Electronic transport signatures of two-electron interactions in all-organic single-molecule junctions

Baum, T.Y.

DOI
10.4233/uuid:dd6db953-9fc5-4be8-99f7-28b2b9e3abd1

Publication date
2024

Document Version
Final published version

Citation (APA)
Baum, T. Y. (2024). *Electronic transport signatures of two-electron interactions in all-organic single-molecule junctions*. [Dissertation (TU Delft), Delft University of Technology].
https://doi.org/10.4233/uuid:dd6db953-9fc5-4be8-99f7-28b2b9e3abd1

ELECTRONIC TRANSPORT SIGNATURES OF TWO ELECTRONS INTERACTIONS IN ALL-ORGANIC SINGLE MOLECULE JUNCTIONS

ELECTRONIC TRANSPORT SIGNATURES OF TWO ELECTRONS INTERACTIONS IN ALL-ORGANIC SINGLE MOLECULE JUNCTIONS

Dissertation

for the purpose of obtaining the degree of doctor
at Delft University of technology
by the authorithy of the Rector Magnificus prof. dr. ir. T.H.J.J. van der Hagen,
chair of the Board for Doctorates
to be defended publicly on
Thursday 11 July 2024 at 15.00 o'clock

by

Thomas Yves BAUM

Master of science in Physics,
Université de Strasbourg, France,
born in Schiltigheim, France.

This dissertation has been approved by the promotors:

Composition of the doctoral committee:

Rector Magnificus,	chairperson
Prof. dr. ir. H.S.J. van der Zant	Delft University of Technology, promotor
Prof. dr. ir. J.M. Thijssen	Delft University of Technology, promotor
Independent members:	
Prof. dr. A. Ardavan	University of Oxford, United Kingdom
Prof. dr. J. Ferrer	University of Oviedo, Spain
Prof. dr. J.I. Pascual	CIC nanoGUNE, Spain
Prof. dr. M. Ruben	Karlsruhe Institute of Technology, Germany
Prof. dr. A.F. Otte	Delft University of Technology
Dr. S.C. Conesa Boj	Delft University of Technology, *reserve member*

This project received funding from the European Union Horizon 2020 research and innovation program under grant agreement no. 863098 (SPRING).

Keywords: Molecular electronics, molecular magnetism, quantum transport, all-organic radicals, poly-cyclic aromatic hydrocarbons, two- and three-terminal measurements

Printed by: Gildeprint, Enschede

Front & Back: Thomas Y. Baum

ISBN 978-94-6366-890-3

An electronic version of this dissertation is available at
`http://repository.tudelft.nl/`.

The associated experimental data for this dissertation are available at
`https://data.4tu.nl/collections/315d55f4-4512-47d7-84bf-af66938758fe`.

CONTENTS

SUMMARY

In this thesis, we use methods offered by state of the art nanofabrication and single-molecule measurement techniques to capture polycyclic aromatic hydrocarbon (PAH) all-organic, di-radical molecules in solid-state devices, and study their electronic transport properties in different conditions with a focus on their magnetic properties.

Chapter 1 introduces the subject and, in chapter 2, the theoretical background is sketched. In chapter 3 we use the mechanically controlled break junction (MCBJ) technique at room temperature to detect electronic transport signatures in the open-shell di-radical, study the influence of anchoring group addition on the molecule, and carry out reference measurements on the closed-shell precursors of the diradicals. We use a neural-network trained to detect molecular features and reference-free clustering to classify breaking traces measurements and distinguish features in the conductance histograms.

Chapter 4 focuses on low-temperature molecular junctions formed in the MCBJ. We probe the magnetic fingerprints of the di-radical displayed by their electronic spectra through inelastic spin-flip excitations and Kondo resonances. We highlight the importance of the exact molecule-metal conformation when sandwiching the radical between the two-electrodes. We also find evidence for a quench of one or both spins that can take place because of the proximity between the electrodes and the radicals sites. As a reference, we repeat the measurement on a molecule with a similar structure but with a single radical center where only Kondo resonances could be observed. Finally, we determine the triplet ground state of the molecular junctions by magnetic-field dependent measurements and find an exchange coupling close to measurements in the bulk with other methods.

In chapter 5 we report measurements of the di-radical in a three-terminal geometry using electromigrated break junctions (EMBJ). We observe similar transport spectra as in the MCBJ and study their gate dependence. We reversibly trigger redox reactions, reducing the total spin of the radical from $S = 1$ to $S = 1/2$ by application of a voltage on the gate electrode. The ground state of the spin-flip signal is studied in a magnetic field and revealed to be anti-ferromagnetic in this measurement.

In chapter 6 we study the devices from chapter 5 that do not show cotunneling features in the off-resonant transport regime. We use the magnetic field and temperature dependence of the charge degeneracy points to study the change of spin entropy in order to determine the ground state of the molecule. A non-linear evolution of the spin entropy is highlighted and related to devices with spin exitations signatures in the SET regime.

In chapter 7 we focus on the Kondo phenomena observed for the di-radical measurements in the two measurements geometries. We measure the changes in the $S = 1/2$ Kondo resonances as a function of mechanical manipulation, electrostatic gating, magnetic field and temperature. We discuss cases extending beyond the single channel $S =$

1/2 Kondo effect with a transition from $S = 1/2$ to $S = 1$ by mechanical manipulation. We observe an anomalous temperature dependence of the Kondo resonance with characteristics similar to the exotic two-stage Kondo effect and highlight the similarity of the signal with the singlet-triplet Kondo effect.

In chapter 8 we move our di-radical molecular junctions out of the solid-state devices to the scanning tunneling microscope (STM) setup. We observe a striking resemblance of differential conductance spectra measured with the STM with the ones obtained in the MCBJ and EMBJ. Mechanical manipulation of the molecule in both the STM and MCBJ setups yield a similar evolution of the spectra. The resemblance is remarkable from the difference in junction geometry of each setups but also the different ways to obtain the open-shell structure in experimental conditions with the constraints associated to each setup.

Finally in chapter 9, we sum up the findings from this thesis and give a brief outlook on the research direction for all-organic radicals in single-molecule electronics.

1

INTRODUCTION

The noblest pleasure is the joy of understanding.

Leonardo da Vinci

In this first chapter, we introduce the research field of this thesis. We start with the essential historical discoveries that led to the field of molecular electronics and give a brief overview of the carbon prospect. Finally, we introduce experimental techniques to contact single-molecules, discuss the ambition of the field and provide an outline for this thesis.

1.1. AN ATOMIC WORLD

In 1827, Robert Brown, a botanist, surgeon and Scottish explorer, observed small particles from *Clarkia pulchella* pollen grain floating on water in a microscope. He noted that the tiny particles are constantly moving for no apparent reason and publishes his findings a year later in "A brief account of microscopical observations on the particles contained in the pollen of plants, and on the general existence of active molecules in organic and inorganic bodies" [1], pointing out that precedent observations have been reported about this phenomenon. Without knowing it, his observation holds the final proof for existence of atoms and molecules. The random motion of particles suspended in a liguant or gas will later take his name: the Brownian motion. Almost a century after Brown's observation, the French physicist Jean Perrin reproduced the experiment in 1908 and used the mathematical model developed by Einstein to determine the size of atoms [2]. The definite proof to the discreet nature of matter, debated for centuries in the physics community, has been reported by a botanist.

Before the validation of the atomic theory, scientists observed several indications for the discontinuity of matter. The "laws of chemical reactions" known at the end of the 18th century, specifically mass conservation and the law of multiple proportions established by John Dalton, paved the main track toward this idea [3]. Dalton observed that for all compounds containing a particular element, the content of that specific element would differ by a ratio of a small whole number. He named these units after the word already used by pre-socratic Greek philosophers: *atomos*, "unbreakable". However, this theory received much opposition from the scientific community, both from a philosophical point of view and regarding counterexamples to his theory, where compounds had identical masses but different properties (later understood as isomers).

In 1859, James Clerk Maxwell, who would soon become famous for his theory of electromagnetic radiations, developed a formula in idealized gases to describe the proportion of particles with a velocity in a specific range: nowadays called the Maxwell-Boltzmann distribution [4]. It is the first argument to explain temperature homogenization, therefore explaining the tendency of these systems toward equilibrium. Only five years later, Ludwig Boltzmann came across Maxwell's paper and spent the rest of his life developing the discipline. Among the groundbreaking ideas developed by Boltzmann, the probability distribution is one of the central concepts that will later lead to quantum mechanics [5]. A probability distribution describes the likeliness of a system to be in a particular state as a function of its ensemble (macroscopic or thermodynamic) parameters. The Boltzmann distribution, or Gibbs distribution, is given by:

$$p_i \propto \exp\left(-\frac{\epsilon_i}{k_B T}\right), \tag{1.1}$$

with p_i the probability for the system to be in the state with energy ϵ_i, the Boltzmann constant k_B and the thermodynamic temperature T. This distribution is consistent with the state function thermodynamic relations and matches Gibbs's definition of entropy. Even though Boltzmann's work was carried out around 1877, most of his work was published in 1896 in "Lecture on Gas Theory" [6]. Before that, the term "statistical mechanic" appeared in 1884 with Willard Gibbs's publication [7]. At a time when German physics journals were prevalent in the world of science communication, Boltzmann encountered several disputes with the editors over his use of the words atoms and molecules. He will die a couple of years before Perrin's publication confirming Avogadro's and Boltzmann's constant, definitely convincing the scientific community about the reality of a world made of tiny particles.

1.2. BREAKING THE UNBREAKABLE

In 1897, J. J. Thomson realized that atoms might be composed of smaller fundamental units by studying the properties of cathode rays [8]. He estimated the mass of the particles composing the rays by comparing the change of temperature when a ray crashes onto a thermal junction with path deflection caused by a known magnetic field. He concluded that the cathode rays are composed of particles with a mass more than 1000 times smaller than the hydrogen atom and that this mass was the same whatever the original atom was. He calls these particles "corpuscules" and proposed that atoms are divisible and composed out of these "corpuscules". Soon, in 1900, Paul Drude used this discovery to propose his model describing the electrical conduction of electrons in a metal [9]. At that time, Ohm's law was already established [10]:

$$V = R \times I, \tag{1.2}$$

linking V the voltage, I the current and R the resistance of an electronic circuit. Drude took a step further by explaining some metals' properties based on the scattering of electrons engraved by immobile positively charged ions. In this theory, electrons' movement is similar to the marble in a pinball machine, where the small charged particles are randomly deflected when bouncing against heavy immobile bumpers (the ions). Hendrik Lorentz extended this model to relate the thermal and electrical conductivity of metals [11]. He used the Maxwell-Boltzmann statistics to derive his model, leading to a semi-classical theory missing several inputs to predict accurate results. Later, in 1933, Arnold Sommerfeld and Hans Bethe supplemented Drude's theory with the new developments of quantum mechanics, producing the Drude-Sommerfeld model [12].

In 1900, Max Plank proposed his hypothesis to explain the black-body radiation problem from Gustav Kirchoff [13]: energy is emitted and absorbed in discrete energy packets, or "quanta" [14]. Planck describe the proportionality between energy E, and frequency v of a radiation:

$$E = hv, \tag{1.3}$$

with h the Plank's constant. Even though Planck insisted on the non-physical reality of his description, Einstein used his hypothesis to develop a model of the photoelectric effect that owed him a Nobel prize [15]. Later, Niels Bohr used this idea in his model of the hydrogen atom to predict the discrete emission spectral lines of hydrogen [16]. Einstein then expanded it to formulate a theory on the stimulated emission of radiation, describing light as particles carrying a discrete amount of energy [17]. The laying ground of quantum theory was set. This period is now referred to as the "old quantum theory". It will be the basis for describing a range of phenomena that cannot be explained by employing classical methods.

Only in the 1920's did the modern formulation of quantum mechanics, with a particular development of mathematical formalism, take form with the contribution of illustrious physicists. However, the apparent discrepancy between observation of the corpuscular behaviour of electrons and its wave nature had no convincing explanation until 1924, when Louis de Broglie introduced a theory describing electrons as standing waves around a nucleus in his PhD thesis [18]. In his concept, he associated with the particle a wavelength λ, with a mass m and velocity v:

$$\lambda = \frac{h}{mv}. \tag{1.4}$$

Schrödinger developed his eponymous equation describing the evolution of a quantum system with the wavefunction formalism based on this idea [19]. Drude theory was derived using the Maxwell-Boltzmann statistic for a gas of electrons. However, this model's prediction did not reproduce several aspects of the electron's behaviour. In 1926, Enrico Fermi published his derivation for the Fermi-Dirac statistics [20], describing a physical system of non-interacting particles following the discovery of the Pauli exclusion principle in 1925: two electrons cannot have the same set of quantum numbers when in the same atom. For any system of identical fermions in a thermodynamic equilibrium, the number of particles in a state i is given by:

$$n_i = \frac{1}{e^{(\epsilon_i - \mu)/k_B T} + 1}, \tag{1.5}$$

with ϵ_i the energy of the i-state and μ the chemical potential. A couple of years earlier, Satyendra Nath Bose published a theory explaining the occupation of the available state at thermodynamic equilibrium, accounting for observations on superfluid helium and coherent laser light behaviour [21]. Einstein extended the idea to describe the behaviour of particles that do not follow the Fermi-Dirac statistic [22]. All the known subatomic particles constituting the universe can be split among these two categories: the ones following the Fermi-Dirac statistic, named fermions, and the others obeying the Bose-Einstein statistic, named bosons.

At its root, the difference between these two classes of particles arises from a property named spin. The spin is often described as an intrinsic angular momentum held by particles. This property was isolated in 1922 in the experiment designed and conducted respectively by Otto Stern and Walther Gerlach [23]. Spin holds its name from the similarity with classical magnetic dipole spinning, which would yield precession in a magnetic field because of the torque arising from the Lorentz force. However, unlike other types of angular momentum, such as orbital angular momentum, this quantity has no counterpart in classical mechanics.

Interestingly, spin existence can be deduced from the Pauli exclusion principle and vice versa. The spin quantum number s of a given particle defines the number of spin states this particle can take $2s+1$. This number takes half-odd-integer values for fermions and integer values for bosons. The smallest non-null value a spin can take is $s = 1/2$, corresponding to the electron spin with two distinct spin states. The two spin states of an electron have opposite values and experience opposite shifts of their potential energy when exposed to a magnetic field.

Besides its fundamental interest in explaining experimental results, such as the hyperfine structure of hydrogen, the concept of quantum spin underlays a range of practical applications. Nowadays, it is used in a variety of devices for digital data storage with giant magnetoresistive (GMR) drive head technology in hard disks, for non-invasive medical imaging with magnetic resonance imaging (MRI), for chemical spectroscopy with nuclear magnetic resonance (NMR) and electron spin resonance (ESR) etc... Among its promises for future applications, quantum computing and spintronics propose to use the spin properties of electrons instead of their charge to engineer a new generation of logic devices [24]. Spintronics takes advantage of spin currents, which does not imply charge carriers to move, resulting in lower power consumption. Quantum computing was initiated in the early 1980s by Yuri Manin and Richar Feynmann, suggesting the possibility of taking advantage of quantum phenomena for efficient computation [25, 26]. At the same time, Paul Benioff described a Turing machine with quantum formalism [27]. Qubits, the equivalent of bit for quantum computers, based on spin encoded information, have been proposed [28] among the promising candidates [29] to build these devices.

1.3. ORGANIC ORGANISATION

Carbon is the fourth most abundant element in the periodic table after hydrogen, helium and oxygen. If we exclude helium, a noble gas with a filled valence band that does not interact, and add a few elements such as nitrogen, sulfur and boron, more stable structures can be built than all the remaining chemical elements of the periodic table. By adding a couple of other species to act as reacting centers, we obtain all amino acids, the structural blocks of life.

Understanding the chemistry of carbon has been a long-running interest in science, from the synthesis of the first organic molecules to the breakthrough from early XIX$^{\text{th}}$ century industrial chemistry. One of the carbon specificities is its ability to form versatile structures. It can form four covalent bonds, allowing for various, complex and stable structures. This property is one of the bases for the vast diversity of organic compounds found in living organisms and the many materials essential to life. Carbon exists in several allotropes with unique properties, the two most known being diamond and graphite. Due to their three-dimensional lattice structure, diamonds are among the hardest known substances and excellent heat conductors. On the other hand, graphite consists of hexagonal lattices of carbon atoms arranged in several layers, with good electrical conductivity and excellent lubricant properties. Finally, carbon is the backbone of organic chemistry, forming the basis for life. Carbon-carbon bonds are stable yet reactive, allowing diverse and complex organic molecules to form. Its ability to form long chains by bonding with each other and forming branched structures is fundamental for biomolecules such as nucleic acids, carbohydrates, and proteins.

These tunable properties shed light on the sixth heaviest element of the periodic table, making carbon a cornerstone of XXI$^{\text{th}}$ century chemistry, material science and biology, with promising properties for future applications. Among the exciting structures formed by carbon-based backbones are aromatic rings, such as benzene, which exhibit unique properties. Aromatic compounds are more stable than their non-aromatic counterparts, characterized by conjugated π bonds in cyclic structures. This highly stable electronic structure is attributed to the delocalization of π electrons over the entire ring, resulting in a lower energy state than localized bonds. In resonant structures, the position of π electrons can be shifted, contributing to the overall stability of the compound. Polycyclic aromatic hydrocarbon (PAH) molecules are composed of multiple aromatic rings. When the π electrons delocalize across multiple resonant structures, the system's overall energy is lowered, yielding more stable compounds. This stability can even take the form of chemical inertness. These properties are advantageous for experimental characterization of all-organic radicals, as they make aromatic compounds less prone to undergo undesired reactions. At the same time, the stability enhances extended conjugation with various organic groups, allowing the formation of larger and more complex molecules.

Like its carbon building blocks, PAHs appear among the most frequent poly-atomic species in the observable universe [30]. They have been observed in meteorites [31], comets [32], planets [33] and nebulae [34]. Their abundance has been recently linked to their synthesis in the interstellar medium [35], possibly explaining missing steps in the abiogenesis of Ribonucleic acid (RNA) [36]. Some PAH molecules, named open-shell structures, present the exotic characteristic of retaining an unpaired electron in a semi-filled π-orbital, leaving the valence electronic structure unfilled. These compounds are called radicals as they hold one or more unpaired electrons; most are unstable as they readily react with ambient oxygen and moisture to alter the original molecule structure. These radicals can be generated through photochemical reactions, high-energy irradiation, or chemical reactions. Their reactivity makes them important intermediates in various synthetic and biological processes that appeared in the course of evolution, such as the fascinating bird's ability to navigate long distances with the help of the Earth's magnetic field [37, 38]. Therefore, understanding the chemical reactions of PAHs in various conditions is of fundamental interest besides their appealing properties for material science.

1.4. CONTACTING SINGLE QUANTUM OBJECTS

Modern instrumentation has enabled scientists to manipulate a small number of atoms, bridging the gap between the microscopic and macroscopic scales. These developments started with the invention of modern photolithography in the mid-50s and the first patent on transistor fabrication methods, marking the beginning of the miniaturization of mass-produced semiconductor devices in 1959 [39]. Imagining a sustained trend of decreasing size, the minimal functioning size of transistors would sit in the range of a few atoms; the idea of building operational devices based on single-molecule building blocks had been mentioned early (see 1.6). The idea of measuring and controlling objects at this scale grew in the physics community by understanding the link between waves and particles. The conception of microscopes using shorter wavelengths started with the development of quantum mechanics, first applying the concept to ultraviolet wavelengths and later pursuing the idea with the trending cathode rays (see 1.2). In 1931, Max Knoll successfully used magnetic lenses to image mesh grids and create the first transmission electron microscope (TEM). Taking the idea a step further in 1972, three physicists built a prototype instrument based on field emission to obtain a topographic map with sub-nanometer resolution [40]. Soon after, in 1981, Gerd Binning and Heinrich Rohrer developed their instrument, imaging features smaller than an angstrom with 10 pm depth resolution: the scanning tunnelling microscope (STM) [41]. Conductance measurements of single C60 molecules on a metallic surface have been performed using this technique [42] shortly followed by experiments on self-assembled n-dodecanethiol monolayers [43].

1.5. SINGLE-MOLECULE DEVICES

Beyond the STM setup previously described, other techniques have been developed to capture single molecules and study their properties. The break junction (BJ) technique consists of two metallic wires separated by a thin gap, in the range of a nanometer, to sandwich a molecule between them. STM-BJ are built using the tip of an STM and repeatedly fusing and opening a metallic gap by crashing the tip into a metallic substrate. Mechanically controlled break junction (MCBJ) uses mechanical strain applied to a suspended metallic wire to open a gap in a patterned constriction. Both methods use mechanical manipulation to yield a similar layout. However, the STM technique allows the precise manipulation of the tip in both the x, y and z directions. It can select an area on the substrate with the required molecular characteristics, while the MCBJ technique relies on substrate bending, allowing for the control of a single degree of freedom. Upon repetition of breaking and contacting between the two electrodes, a single molecule may be trapped in the gap. Molecular junction formation is a random process, and experiments must rely on statistics over many breaking events to obtain a reliable outcome.

Mechanically fabricated break junctions allows for a change in the molecule metal geometry after the initial gap opening. However, the advantage is limited: the typical layout is a two-terminal measurement. Despite the addition of a third gate electrode in some experiments [44], their efficiency is low, and the significant charging energy typically observed in molecules limits the ability to change its charge state.

Electromigrated break junctions (EMBJ) offer the advantage of integrating a third gate electrode, capacitively coupled to a gate potential and insulated by a thin layer of oxide, to maximize the change of electrostatic potential sensed by the captured molecule. In this way, a transistor-like device is obtained as the gate electrode can be used to align the discrete energy levels of the molecule with respect to the electrochemical potential of source and drain electrodes, modulating transport between the resonant and off-resonant regimes. To open a nanogap, EMBJ devices use the electrostatic interaction of the electric field and the metallic ions (Lorentz force) and the momentum exchange (Joule heating) between conduction electrons and the ions. However, unlike the mechanical break junction devices, the gap cannot be further modified once it has been opened.

1.6. MOLECULAR ELECTRONICS

The idea of molecular electronics appeared in the second half of the XXth century with the goal of leveraging tailored properties of molecules to build an innovative new generation of devices differing from traditional semiconductor-based electronics. The original aim of the field was to create molecular-scaled devices, such as transistors, diodes and wires to revolutionize the landscape of electronic technology. The first mention of this idea can be found in a publication from Arthur Von Hippel in 1956 [45]. He describes a bottom-up procedure to develop electronic components from atoms and molecules rather than from patterned materials. The first proposed device based on this concept, described in a publication from Ari Aviram and Mark Ratner [46] in 1974, is a rectifier diode based on donor-acceptor interactions.

Based on these discoveries, Aviram proposed in 1988 to use π-conjugated molecules to perform computation [47]. He developed a theoretical system based on $\pi-\sigma-\pi$ mixed-valence type molecules providing a double-well potential, tunable to a single well, for single electron operation through the device. He suggested implementing logic gate schemes with this model, such as OR [46], AND [48], and even composed HALF ADDER, allowing for basic computations with a molecular device. Shortly thereafter, the first implementation of logic gates using molecules was published in 1993 by Prasanna de Silva and coworkers [49]. They build a molecular AND gate with a fluorescent output by converting signals from ionic to photonic ones. However, building more complex architectures required the combination of several different logic gates, which could not be proved by completing the truth table due to the binding instability of the molecular compounds. Several other implementations of more complex logic gates have been performed over the years, such as NAND [50], NOR [51] and XOR/XNOR [52], aiming to create the building blocks for practical molecular devices. However, commercial devices based on these concepts do not exist, attesting to the failure of molecular electronics to reach their original goal of building devices suitable for practical applications. The variations of properties from device to device, reliability over a long time and the impossibility to scale production restricted commercial exploitation.

Despite the apparent setbacks, molecular electronics explored the idea of leveraging quantum properties in practical applications and highlighted unexplored physical phenomena governing the behaviour of mesoscopic systems. Investigating single molecules allowed researchers to delve into the quantum effects that manifest at this scale, shedding light on phenomena such as electron tunnelling, quantum interference, and electron-electron correlations. Furthermore, the field's interdisciplinary nature, involving expertise in chemical synthesis, quantum chemistry, theoretical modelling, and experimental implementation, encouraged collaborations, enhancing the understanding of molecular interactions and driving innovation in nanotechnology and quantum computing. While commercial applications have yet to materialize, ongoing interdisciplinary efforts continue to refine the theoretical frameworks and push the experimental techniques, holding the promise to unlock the full potential of the discipline in the future. Much like Robert Brown in front of his microscope, molecular electronics may be currently focusing on its small erratic particles, with the potential to unlock an extensive collection of questions through an interdisciplinary vision of the extended collection of physical phenomena it perceives.

1.7. THESIS OUTLINE

In this thesis, we study di-radical molecular junctions using an all-organic polycyclic aromatic hydrocarbon (PAH) molecule. This di-radical PAH molecule, the 2-OS, is the same throughout the chapters, with the difference that some molecular junctions were formed using the same backbone with the addition of sulfur-methyl groups, the Sme-2OS. In the next chapter, we introduce the theory to understand the results obtained with these di-radicals. In chapter 3, we present an investigation of the two di-radicals of interest at room temperature with the MCBJ technique. As a reference, we measure the closed-shell precursors of the di-radicals presented. In chapter 4, we carry out our investigations with the MCBJ technique at low temperature. The magnetic fingerprints observed in the di-radical molecular junctions are linked to the molecular charge state and we determine the exchange coupling between the two free electrons with magnetic field measurements. In chapter 5, we move to three-terminal measurements by using the electromigrated break junction technique at low temperature and link the results to those observed in the MCBJ. In chapter 6 we focus on the molecular junctions of chapter 5 and study their spin entropy evolution with the aim to determine its ground state. In chapter 7 we focus on the Kondo resonance measured over the previous chapters with the different techniques. In chapter 8, we mechanically manipulate the di-radical in a scanning tunneling microscope setup and compare with the results obtained from MCBJ. Finally in chapter 9 we finish with concluding remarks and a quick outlook.

2

THEORY

Nothing in life is to be feared,
it is only to be understood.

Marie Curie

In this chapter, we introduce the theoretical concepts to comprehend charge transport through single-molecule junctions. We start with a description of electron tunneling and introduce the quantum-transport regimes in molecular junctions. We then expand our description to three-terminal devices and introduce higher-order transport processes with inelastic electron tunneling spectroscopy and the Kondo effect.

In this chapter, we discuss the use of electronic spectroscopy to study single-molecule electronic structures. We introduce the basic theory to understand transport through a single molecule sandwiched between gold electrodes. Although valid for our approach, the reasoning described here is compelling for other mesoscopic structures, including, but not limited to, quantum dots, nanotubes, nanowires, and metallic islands.

2.1. ELECTRONIC SPECTROSCOPY

Electronic transport spectroscopy is performed by measuring a current I through a circuit as a function of an applied voltage V or vice-versa. The voltage is applied between macroscopic source and drain electrodes connected to a smaller nanostructure of interest to study its effects on the flow of conduction electrons. Several significant parameters of the flowing electrons govern the electronic transport through the nanostructure. Ohm's law is valid in the linear approximation: when the mean free path, the phase coherence length and the de Broglie wavelength of conduction electrons are all smaller than the circuit elements' scale the Drude model can be used. When the size of the wave function of the conduction electrons is of the same order or larger than the nanostructure, quantum mechanical effects come into play, and non-linear behaviour has to be taken into account. In a mechanically controlled break junction, when the wire is stretched upon the breaking point as displayed in figure 2.2 d, the reduction in the size of the narrower circuit element leads to the quantization of the conductance in steps, approximately equal to multiples of $G_0 = 2e^2/h$ where e is the electron charge and h is the Planck constant. Before the wire breaks, an atomic point contact may form between the two leads, leading to a plateau around one G_0 of conductance with a length proportional to the size of a single gold atom.

Upon the wire's opening, the conductance drops in the tunnelling regime ($G \ll G_0$), and a molecule may be trapped in the opened gap to form a molecular junction. Whether a molecule links the two electrodes can be inferred from the conductance variation as a function of electrode spacing. In a tunnel junction two metallic conductors are separated by an insulating layer, here, vacuum. The electron wave nature leads to a non-zero probability for tunneling from one side to the other. This process is probabilistic, and the odds for an electron to tunnel are determined by the height and width of the potential barrier formed by the insulator, as well as intrinsic particle properties such as its mass and energy. This setup can be modelled by two electron reservoirs, each with its density of state determined by the Fermi-Dirac distribution, separated by a potential barrier. This layout is represented in figure 2.1 a,b and using Wentzel-Kramers-Brillouin (WKB) approximation [53] the resulting current can be modelled as a function of bias voltage V (see figure 2.1 c) and insulator thickness d (see tunnelling conductance under G_0 on figure 2.1 d). In an empty molecular junction, the current thus decays exponentially and appears as a straight line in a semi-log plot of the conductance as a function of electrode spacing (as displayed in figure 2.1 d).

2.1.1. CHARACTERISTIC SCALES

When capturing a molecule in an electronic circuit (see figure 2.2 a), the properties observed depend on the interplay of several physical quantities. Due to their small size,

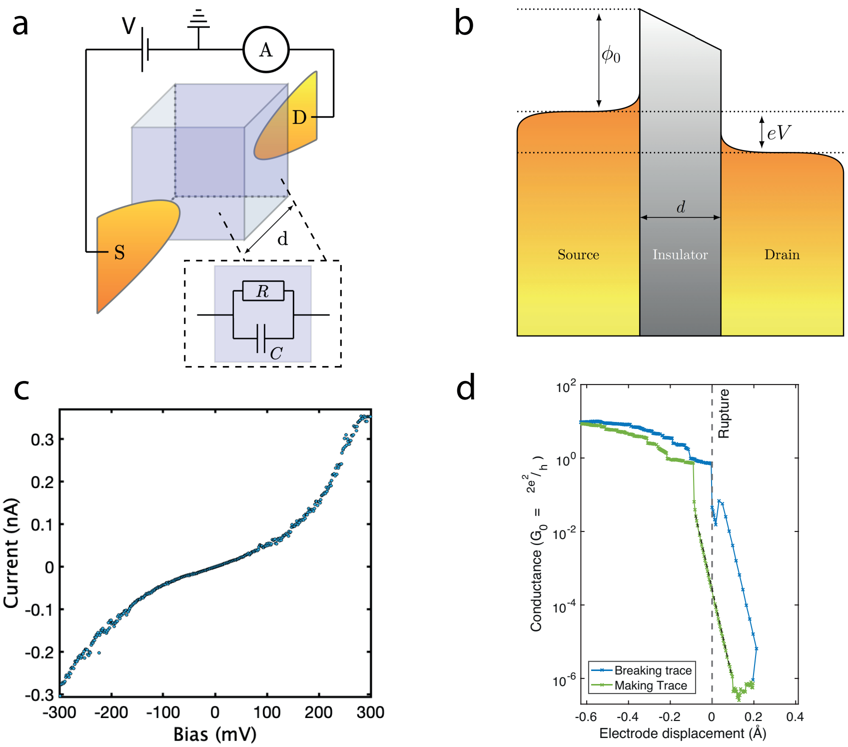

Figure 2.1: (a) Representation of a molecular junction in two-terminal measurements. A box of size d is connected to a source (**S**) and drain (**D**) electrode. A bias voltage V is applied in a two-point measurement scheme while the current is measured. The electrode-box interfaces (blue faces of the cube) behave as a tunnel barrier: (inset) the hopping can be modelled as a capacitor in parallel with a resistor. (b) Representation of a metal-insulator-metal junction such as in an empty mechanically controlled break junction (MCBJ) with two electron baths separated by a potential barrier of height ϕ_0 and width d. When there is a potential difference, eV, between the two electrodes, the barrier changes from a rectangular to a triangular shape. (c) Tunnelling current in an open junction as a function of bias voltage. The non-linear behaviour is captured by the Simmons model [53]. The change of conductance depends on the potential barrier's height, width and shape. (d) Conductance of a pristine gold mechanically controlled break junction as a function of electrode displacement; conductance is plotted on a logarithmic scale. The sloped line at conductance values under 10^{-1} G_0 corresponds to the tunneling current between the two electrodes, highlighting the exponential dependence of the current on the potential barrier width.

spatial confinement between the charge carrier leads to a spectrum of discrete energy values. Level spacing is dictated by the confinement energy (Δ) that can be roughly estimated from the particle in a box model. The smaller the box, the larger the value taken by the confinement energy:

$$\Delta = \frac{\hbar^2}{2m_e}\left(\frac{\pi}{d}\right)^2, \tag{2.1}$$

with $\hbar$ the reduced Planck constant, m_e the free electron mass and d the box length. In a molecule with a typical size of about a nanometer, the confinement energy is a few hundred meV. The small size of molecules and their large confinement energy imply that the charge carriers are close, and Coulomb repulsion plays an important role. This interaction is accounted for by a charging energy:

$$E_c = \frac{e^2}{2C}, \tag{2.2}$$

with e the electron charge and C the molecule capacitance to its environment. In addition to the effect of capacitance on the energy spectra, the molecule's configuration in the junction also determines the probability for an electron to tunnel from one electrode into the molecule and tunnel out into the other electrode, resulting in a net current. These interfaces between the molecule and the conductor can be described in terms of tunnels couplings (Γ in figure 2.2 a,b), i.e., a resistance in parallel of a capacitor, giving the rate at which an electron tunnel from an electrode to the molecule and vice-versa. These couplings are linked to the characteristic time an electron spends on the molecule:

$$\tau = \frac{\hbar}{\Gamma} \tag{2.3}$$

The electrons tunnelling through the molecule see their interactions bound by this characteristic time. In the strong coupling regime $\Gamma \gg \Delta, E_c$, large couplings lead to a short time on the molecule as many charge carriers are hopping on and off; an electron does not have the time to interact, and transport is coherent as electrons preserve their phase. In the weak coupling regime $\Gamma \ll \Delta, E_c$, it is the opposite: the long time spent by the conduction electrons on the molecule allow for interactions and dephasing, leading to incoherent transport through the structure.

2.1.2. MOLECULAR ORBITALS

Realistically, the discrete energy states of a charge carrier bound in the molecule are described by its wave function. In an isolated atom, this function is called an atomic orbital and is determined by the potential landscape formed by the atom nuclei. Orbitals follow the Pauli exclusion principle: they are, at most, occupied by two electrons. Electrons populate the molecular orbitals, starting with the lowest available energy and successively filling higher ones. In a molecule, multiple atoms combine by forming valence bonds, and the atomic orbital cannot be considered individually anymore but are determined by the molecule as a whole. Combining atomic orbitals composing the molecule yields molecular orbitals. The filled molecular orbital with the highest energy is called the highest occupied molecular orbital (HOMO). In the same way, the empty molecular orbital with the lowest energy is called the lowest unoccupied molecular orbital (LUMO). HOMO and LUMO levels are the discrete equivalents of valence and conduction bands (respectively) for semiconductors. They are the most critical levels for understanding transport phenomena in quantum dots and molecules.

The precise electronic structure of a molecule can be inferred from quantum chemistry calculations such as density functional theory (DFT). However, such methods are computationally expensive and reproduce experimental results only to some extent. The complexity of these calculations grows exponentially with the number of elements to consider. In a molecular junction, van der Waals interactions and metallic ions play an essential role in the exact molecule conformation and the potential landscape it experiences, which is not possible to model precisely in the context of a particular experiment.

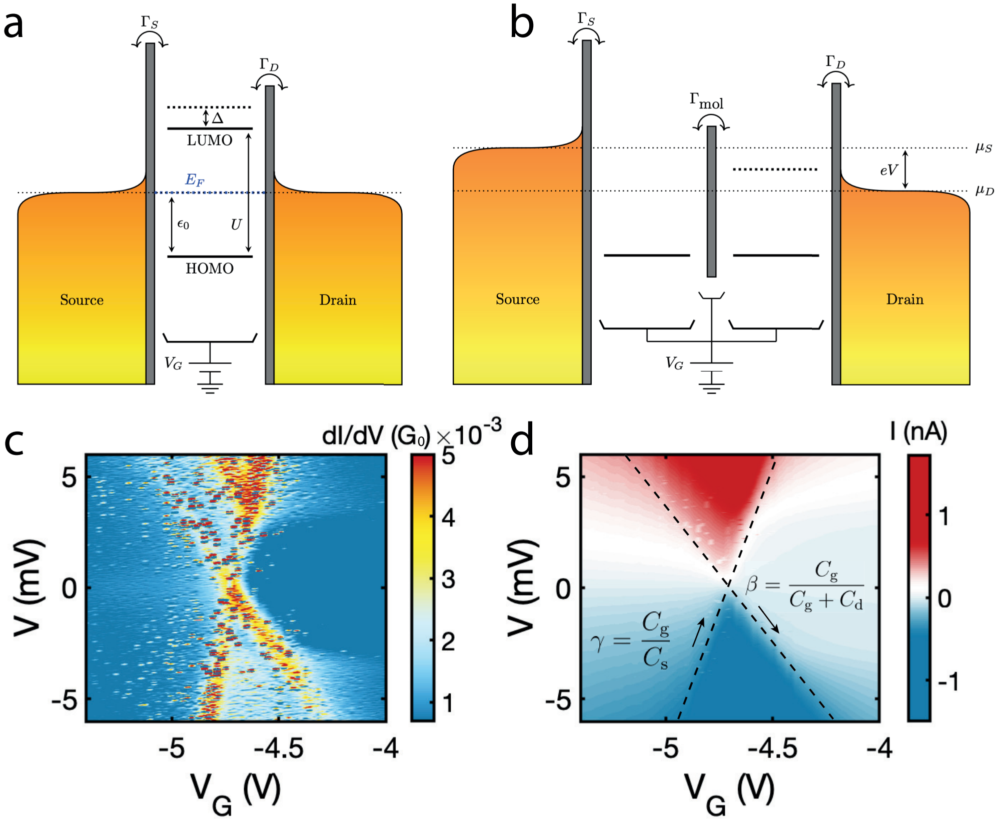

Figure 2.2: (a) Schematic representation of a molecular junction: a set of molecular orbitals is sandwiched between source and drain electrodes acting as an electron reservoirs. Tunnel barriers with hopping parameter $\Gamma_{\mathrm{S,D}}$ represent each molecule-metal interface. The molecular orbitals alignment with the electrode potential can be adjusted using a third gate electrode capacitively coupled to the molecule. (b) When there is more than a single site on the molecule (in a di-radical for this example), another potential barrier can model their coupling strength. When this barrier is smaller than the tunnel couplings, the two impurity molecular orbitals are hybridizing, and the junction is equivalent to (a). When the molecule barrier is large, the two electrons are decoupled and act as two independent $S = 1/2$ molecules. The potential can be different between the two sides of the barrier, leading to differential gating of the molecular orbitals. Measurements of a three-terminal device summarized in stability diagrams of differential conductance (c) and current (d): sweeping the source and gate voltage bias and measuring the current through the junction: (d) typical molecular devices display alternating regions of high current (blue and red) and blocked transport (white); the slope separating the high and low current regions is determined by the capacitive coupling of the molecule to the electrodes.

2.2. LANDAUER APPROACH

Describing charge transport through a molecule goes back to counting the number of electrons tunnelling through the structure in a selected direction. The transport processes allowing electrons to tunnel are energy-dependent and can be summed up in a transmission function $T(E)$ and the resulting current through the junction is obtained using the Landauer-Buttiker formula:

$$I = \frac{2e}{h}\int T(E)\,[n_S(E) - n_D(E)]\,dE, \tag{2.4}$$

with $n_{S,D}$ the Fermi-Dirac distributions of the source (S) and drain (D) electrodes. At 0 K, the electrode's chemical potential is defined as the Fermi energy (E_F see figure 2.2). At equilibrium, when $\mu_S = \mu_D$, the chemical potential of both electrodes is equivalent, and there is no net current. When a symmetric bias voltage is applied, the chemical potential of the electrodes is shifted, and the energy range between the two is called the bias window. If no molecular orbital is present in the bias window, electrons do not have the energy to populate or leave the energy level: the current is blocked. Increasing the bias voltage up to a bias window aligned with a molecular level opens a new channel for transport, thereby increasing the current through the junction.

2.2.1. RESONANT TRANSPORT

In a first-order (resonant) process, i.e., when an electron spends a longer time in an orbital than the time it starts to lose coherence, electron transport is incoherent. As displayed in figure 2.3 a,b these tunnelling processes can happen through the ground state of the molecule, i.e. the LUMO, but also through an excited state. During these processes, the total charge of the molecule goes from $N \to N+1$ and its total spin change by $\pm 1/2$; this is called sequential or single -electron tunneling (SET). When an electron tunnels to the molecule by SET and is expelled toward the other electrode in a distinct SET event, this incoherent charge transport produces a net current through the junction. Note, that an electron can tunnel from an electrode to the molecule and then to the same electrode again. This is proportional to the hybridization of the molecular levels with the metallic electrodes, leading to a Lorentzian broadened density of state. This hybridization depends on the tunnelling rate between the molecule and the electrodes, and the overall hybridization of the molecular orbitals needs to be accounted for both contacts $\Gamma = \Gamma_S + \Gamma_D$.

The alignment of the molecular chemical potentials with the bias window can be adjusted using a third electrode. This third electrode, capacitively coupled to the molecule, influences the electrostatic environment without charges flowing through this path (otherwise leading to leakage currents). Charging the gate positively/negatively, i.e., applying a positive/negative bias voltage, attracts/repulses the electrons occupying the molecular orbital, yielding a shift of the alignment of the molecular levels with respect to the Fermi energy. This process allows for reducing/oxidizing the molecule, and thus changing its ground state by pushing a molecular orbital through the Fermi energy.

Typical measurements to characterize such devices involve sweeping the bias and gate voltage and measuring the current flowing through the device. Results are summarized in colour-coded current maps called stability diagrams displayed in figure 2.2 c,d.

The molecular junction diagrams are characterized by alternating regions of high conductance in an hourglass shape in the SET regime and diamond-shaped regions of blocked current called Coulomb diamonds. Moving from one diamond to another implies changing the charge state of the molecule. Excited states appear as bright slanted lines in the stability diagrams. The resonance between two Coulomb diamonds is called the charge degeneracy point (CDP), where the molecule can be in either one of the charge states of the neighbouring diamonds. A capacitive coupling exists between the molecule and the gate, C_{G}, and between the molecule and the electrodes, $C_{\mathrm{S,D}}$. The ratio between these couplings defines the slope of the diamond edges: $C/C_{\mathrm{G}} = 1/\alpha = 1/\beta + 1/\gamma$, with α the gate coupling parameter, β the positive diamond slope and $-\gamma$ the negative diamond slope (see figure 2.2 d).

2.2.2. HIGHER-ORDER PROCESSES

We considered resonant tunnelling processes up to now, where a single electron tunnels from the source to the molecule to the drain. We will now consider higher-order processes involving more than a single particle. The current in the SET regime scales with Γ while the latter scales with Γ^2, making it more sensitive to the couplings with the electrode.

Resonant transport cannot occur as the number of electrons on the molecule is fixed. However, an electron can tunnel from a molecular level to the drain if another electron tunnels into the molecule in a time capped by the Heisenberg uncertainty principle as displayed in figure 2.3 c. During the time lap where the number of charges on the molecule changes its state is "virtual": the molecule is neither reducing nor oxidizing. This process is called cotunneling (COT) as it implies multiple tunneling event for transport. The electron tunnelling out of the molecule does not necessarily occupy the same level as the incoming electron. Suppose the electron tunnelling from the source to the molecule occupies an excited state while the electron leaving the molecule to the drain is on a different level. In that case, the process is inelastic as the total molecule energy is not conserved between the initial and final state.

Following energy conservation, inelastic processes can only occur if the bias window is equal to or larger than the energy separation between the ground and excited states. When the bias voltage exceeds this energy, another transport channel opens, increasing the conductance of the molecular junction. In the Coulomb diamonds, inelastic COT excitations appear as horizontal lines (when the energy spectra of the molecule are gate-independent in a single charge state; a counter-example can be seen in [54]). This method is used to detect excited states; it is called inelastic electron-tunneling spectroscopy (IETS) and can happen through vibrational or excited electronic states. When the excited state is a different spin state, these processes are called inelastic spin-flip excitations, as the electron spin on the molecule has been flipped during the process. As these excitations occurs in the low condutance regions of the stability diagrams (Coulomb Diamonds) it is more convenient to display the differential conductance derived from the IV measurements. An example is shown on figure 2.2 c where a spin-flip signal is visible in the right diamond at an energy of about 3 meV. As the allowed spin transitions are determined by spin-selection rules [55], one can follow the evolution of the excitations with respect to an applied magnetic field and infer the electronic spectra of the molecule by lifting the degenerated molecular orbitals and following the corresponding transitions on an equivalent of a stability diagram where the magnetic field replace the gate voltage (an example is displayed in figure 4.3).

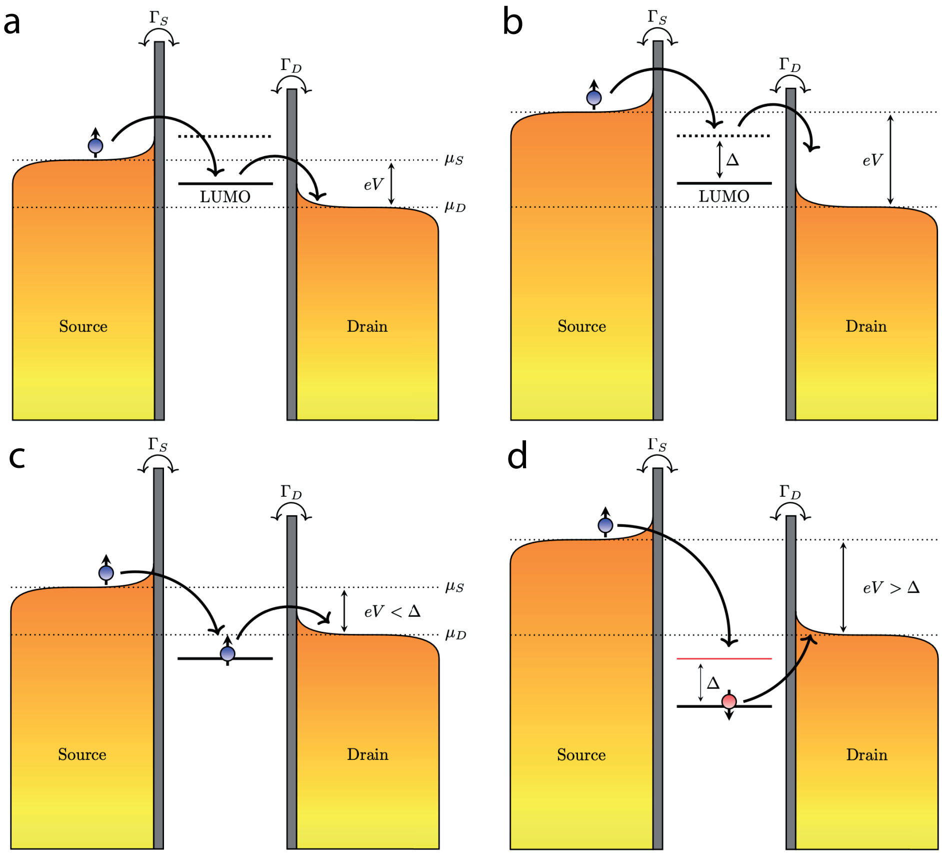

Figure 2.3: Schematic representation of real (a and b) and virtual (c and d) charge transport processes in single-molecule junctions. (a) When a molecular level is aligned within the bias windows opened by the electrode's potential, an electron can hop from the source electrode to the molecular orbital in a sequential electron tunnelling (SET) event. Current flows through the junction if this electron tunnels toward the other electrode in a distinct SET event. (b) This SET process can also happen through any excited state of the molecule provided that it lies within the bias window. (c) When both the ground and excited state of a molecule are outside the bias window, a higher order process can participate to transport through the junction. (d) If the bias voltage between the source and drain electrodes is larger than the energy difference between the ground and excited state Δ, an electron can tunnel to the excited state of the molecule while, and in the meantime, another electron tunnels from the molecule to the drain electrode in a cotunneling (COT) process. (c) If the two electrons tunnel toward and from the same molecular orbital energy transfer is elastic. (d) The energy difference leads to inelastic transport if the electrons tunnel toward and from two distinct molecular levels.

2.2.3. KONDO EFFECT

When the coupling of a molecular orbital is larger than the energy difference in a degenerate level, multiple spin-flip events can occur, leading to the screening of the unpaired electron(s) localized on the molecule by the conduction electrons in the leads at the Fermi level. As a result, a many-body singlet state forms, coupling the spin of the localized electron with anti-ferromagnetic interaction to the nearby conduction electrons leading to a total spin of zero. The effect is named after its discoverer, the Kondo effect. It has been predicted theoretically and observed in bulk for diluted magnetic impurities in metallic alloys [56] and has been observed in a variety of nanostructures since [57]. The Kondo effect in molecular junctions takes place in the case of strong coupling between the molecule and the lead under a threshold value, T_K, the Kondo temperature. Below this temperature the screening electrons form a Kondo-cloud around the molecule to compensate its spin. As a result, a zero-bias resonance in the differential conductance spectra appears in the low-conductance regions of the stability diagrams, whose width is related to the Kondo temperature.

The effect is typically found in $S = 1/2$ molecules, where a single magnetic impurity is interacting with the electrodes. Kondo correlations are more significant for an odd number of electrons on the molecule. However, spin systems with larger spin can also display the Kondo effect depending on its ground state and the couplings. Applying a magnetic field to a spin 1/2 level lifts its degeneracy through Zeeman splitting, and the zero-bias resonance also splits in two when the Zeeman energy ($g\mu_\mathrm{B}B$) gets larger than the Kondo energy ($k_\mathrm{B}T_\mathrm{K}$).

2.2.4. TWO INTERACTING IMPURITIES

When considering conductance through a poly-radical, the previous description still holds considering the molecular spectra as an ensemble (i.e. a set of chemical potentials between two tunnel barriers). However, this molecular spectrum is the result of molecular orbitals hybridization. In a di-radical, where there are two free electrons, we can take a step further by decomposing the molecular spectra into two molecular orbitals coupled to each other. This coupling is represented by a third tunnel barrier in figure 2.2 between the two molecular levels. Note that this layout is particularly relevant for two series-coupled quantum dots described in chapter 9. The molecular barrier is different from the interfaces; physically, it describes the hoping of an electron from one molecular orbital to the other. If this barrier is in the same energy range as the interfaces, there is no exchange coupling between the two electrons, and they act as two independent $S = 1/2$ molecules. This case corresponds to a bi-radical with two non-interacting electrons. When the molecular barrier is smaller than the interfaces, $\Gamma_\mathrm{mol} \ll \Gamma_\mathrm{S,D}$, the two orbitals couple together to form a new ground and excited state. For two $S = 1/2$ particles hybridizing together, the doublet states form a new ground and excited states, singlet and triplets.

Whether the singlet is the lowest in energy or the triplet will define the exchange coupling between the two electrons. The coupling is ferromagnetic for a triplet ground state, and the electrons prefer to orient in the same direction, while for a singlet ground state, the electrons will form a pair with opposite spins. This difference occurs in the symmetry between the two Fermion wave functions. It is interesting to note that a molecule can have several stable conformations; in some molecules, these conformations can imply different wave function symmetries between the orbitals. This means a stable di-radical molecule may transition between ferromagnetic and anti-ferromagnetic ground states for different conformations.

Also, it is worth noting that the two molecular orbitals do not necessarily have the same gate coupling. We can imagine the case of a di-radical with one of the orbitals strongly coupled to an electrode, far from the oxide insulating the gate, and the other close to the gate and less coupled to the electrodes. The gate would influence the two orbital differently, especially regarding the quadratic evolution with the distance of the Coulomb repulsion. This effect would lead to a "differential" capacitive coupling that could influence one of the orbitals more than the other. In this case, the gate could push this second orbital above the Fermi energy (but not the first), changing the number of charges on the molecule from $N = 2$ to $N = 1$ leading to the reduction of the di-radical to a single radical leaving a $S = 1/2$ Kondo resonance in the differential conductance spectra. The gate can also affect the intra-molecular coupling, modifying the coupling strength and the wave function symmetry between the two electrons. In this way, the di-radical triplet and singlet states would form two independent doublet. If at lease one of these doublet is strongly coupled to one of the electrodes the differential conductance spectra would display a $S = 1/2$ resonance as well. However, the two effects may be difficult to recognize this differential gating mechanism in an experiment since a similar differential conductance spectra is expected for both effects.

3

ELECTRONIC TRANSPORT CHARACTERISTICS IN ALL-ORGANIC POLY-CYCLIC AROMATIC HYDROCARBONS DI-RADICAL MOLECULAR JUNCTIONS

> *Ludwig Boltzmann, who spent much of his life studying statistical mechanics, died in 1906, by his own hand. Paul Ehrenfest, carrying on the work, died similarly in 1933. Now it is our turn to study statistical mechanics.*
>
> David L. Goodstein, opening of *States of Matter* (**1975**)

Polycyclic aromatic hydrocarbons (PAH) are an interesting class of compounds, amongst their properties, free spins can exist in semi-filled π *orbitals up to room temperature in their open-shell form, making them of practical interest for spintronic purposes. In this chapter, we show electronic transport measurements through PAH molecular junctions in the precursor and purified di-radical forms with the mechanically controlled break junction (MCBJ) technique.*

3.1. INTRODUCTION

Polycyclic aromatic hydrocarbons (PAH) are a promising class of compounds for fundamental studies of molecular electronics and their possible applications. Their ability to retain an unpaired spin in a semi-filled orbital has been studied in various devices such as scanning tunnelling microscope break junctions (STM-BJ) [58], mechanically controlled break junctions (MCBJ) [59], electromigrated break junction (EMBJ) but also in bulk with electron-spin resonance (ESR), superconducting quantum interference devices (SQUID) or thin film solid-state devices. However, open-shell compounds are highly reactive, both with humidity and oxygen in the ambient atmosphere, reducing the radical to their closed-shell state. Recent advancement in atomically precise synthesis of all-organic molecules allowed to produce new all-organic radicals stable at room conditions with interesting properties for applications such as rectifying diods [60–62], batteries [63–65], field-effect transistors [66–68] or light emitting diodes [69–71]. These molecules are also sought as potential candidates for thermoelectric power harvesting devices due to their expected high Seebeck coefficient [72–74]. Nonetheless, the magnetic impurities held in these molecules are promising candidates for a new class of devices exploiting the spin properties of electrons in addition to their charge, extending the possibilities of currently developed electronics with low-power and highly efficient devices. Despite these outstanding properties, integrating a single radical molecule in a solid-state junction presents several challenges; retaining the unpaired spin in the molecule when sandwiched between metallic electrodes is essential.

In this chapter, we study the charge transport properties of 2-OS all-organic di-radical and the influence of sulfur-stabilizing groups' incorporation with the Sme-2OS di-radical. The structure of the four compounds used in this study is displayed in figure 3.1. Our investigations are based on the mechanically controlled break junctions (MCBJ) technique at room temperature and atmospheric pressure. As a reference, we measure the 2-CS and Sme-2CS precursors where the radical character of the PAH is absent due to the hydroxyl groups attached to the fluorenyl units. These compounds have been investigated by several methods: at low temperature with the mechanically controlled break junction technique (≈ 4 K, see chapter 3) and the electromigration break junction technique(see chapter 5), and with ensemble methods such as SQUID magnetometry and ESR [75]. The detailed synthesis of the compounds is described elsewhere [76].

Previous studies focusing on single-molecule radical junctions highlighted enhanced conductance compared to their closed-shell counterparts [58, 59]. Our approach allows us to study both the radical and reduced forms of all-organic molecular junctions without changing the electrostatic environment through ionic gating or solvent modification. We measure the electronic transport properties of the 2-OS, 2-CS, Sme-2OS and Sme-2CS molecules and use neural network [77] and reference-free clustering methods [78] to analyze and compare the results from the experiments. The combination of highly delocalized radical states with the inherent steric hindrance protecting them from reaction with oxygen in the environment, preserve the radical character of the molecule. We find a strong dependence of the transport properties of a radical molecular junction on the exact molecule-metal configuration. This study also highlights all-organic neutral radicals as highly stable compounds under ambient conditions particularly suited for molecular electronics experiments.

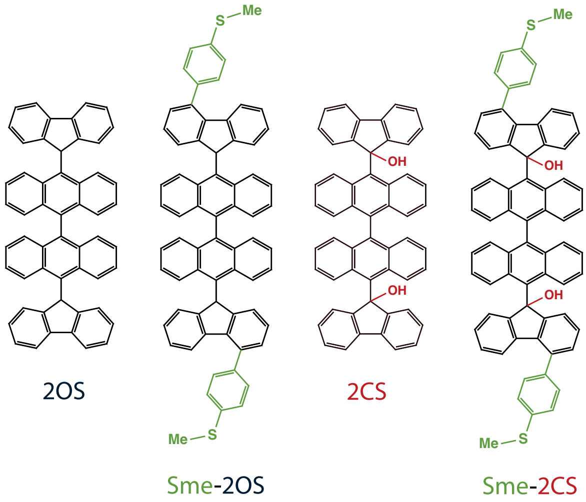

Figure 3.1: From left to right: molecular structure of the all-organic di-radicals **2-OS** composed of two fluorene moieties holding a radical center linked by two anthracene units and **Sme-2OS** holding extra sulfur-methyl stabilizing groups connected to the di-radical backbone through a benzene ring. The **2-CS** and **Sme-2CS** are the precursors of **2-OS** and **Sme-2OS**; the reaction to radicals is triggered by dehydroxylation of the OH groups connected to the fluorenyl units.

3.2. MEASUREMENTS

Molecular junctions based on each of the four compounds displayed in figure 3.1 are studied using the MCBJ method: a molecular solution of 0.1 mM of the selected molecule diluted in dichloromethane (DCM) is drop-cast on top of an MCBJ device. Once the solvent is completely evaporated, fast-breaking measurements are started by driving the piezo element pushing against the flexible substrate at a speed of 50 V/s with a constant voltage bias of 100 mV. As the 2-OS di-radical doesn't hold any anchoring groups and is expected to produce molecular junctions with a low yield, we use a supervised tunnelling removal algorithm based on a neural network trained on a set of different molecule measurements (details about the procedure can be found in Ref. [77]).

The results are compiled in two-dimensional histograms and displayed for the 2-OS molecule in figure 3.2 with (top-left) the tunnelling class corresponding to empty junctions and (top-right) the features class that doesn't fit within the tunnelling category. The features class corresponds to 5.3 % of all the traces in this experiment, close to the yield observed for the same di-radical in MCBJ at low temperature [76]. From the 2D histogram categories, we see that breaking traces labelled as tunnelling appear shorter than the features class: at electrode displacements larger than 1 nm, almost no counts are observed. However, no clear molecular plateau is distinguishable in the data. The differences between tunnelling and features classes are better seen in the one-dimensional conductance histogram (bottom picture from figure 3.2), highlighting the different number of counts with respect to conductance between the tunnelling class and the features. Normalizing the counts by the 1 G_0 plateau, we observe a peak in both categories around 10^{-6} G_0; this feature is attributed to the amplifier as its conductance shifts with respect to the bias voltage applied. The peak is also visible in the reference measurements taken on bare gold before molecular deposition displayed in SI figure 3.7.

3.3. RESULTS AND DISCUSSION

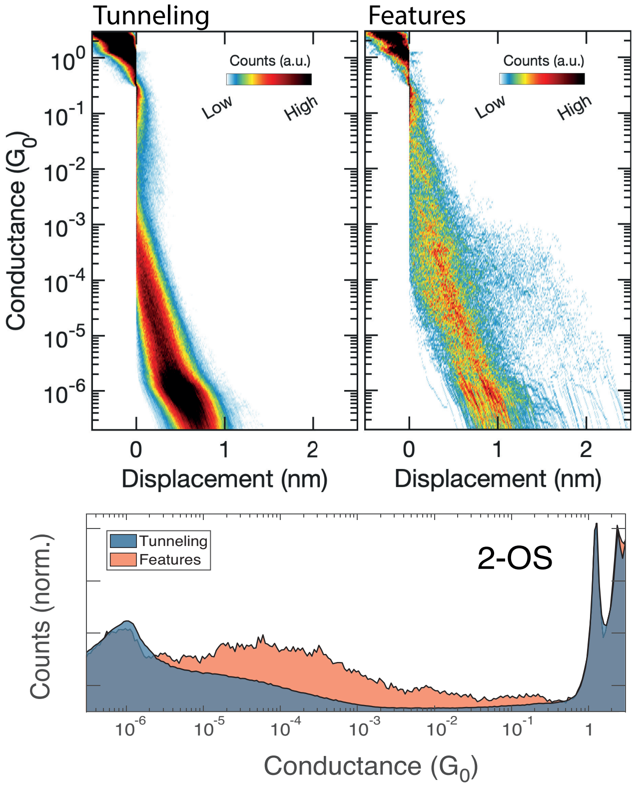

Figure 3.2: Two-dimensional conductance-displacement histogram of breaking traces labelled by the neural network classification as (top-left) tunnelling and (top-right) breaking traces containing molecular features for 2-OS. Bottom: corresponding one-dimensional conductance histogram of 2-OS highlighting counts distribution with respect to conductance for (blue) tunnelling and (red) molecular features breaking traces.

We use the features extracted with the neural network in figure 3.2 to categorize the breaking traces into subclass in order to separate the different features. To this end, we use a reference-free clustering method previously detailed elsewhere [78]. We build 33 × 66 pixels image of the 2D histograms with conductance range from 10^{-1} down to 5.10^{-6} G_0 and displacement from -0.5 to 2.5 nm. We add the 1D histogram to the feature vector created from the image with 100 bins. We minimize the number of classes in order to capture distinguishable features in the conductance-displacement histogram of each subclass. The result of the clustering analysis on the 2-OS di-radical is displayed in figure 3.3 (top). Along with a class displaying an intermediate conductance plateau, we find a subclass containing features in the high-conductance region (subclass 1, above 10^{-3} G_0) at electrode displacement below one nanometer and another with low-conductance features (subclass 3, under 10^{-4} G_0). The intermediate conductance plateau around 10^{-4} G_0 displays counts up to an electrode displacement of 1-1.5 nm; it is the longest of the three subclasses corresponding to the most extended molecule configurations in the junction.

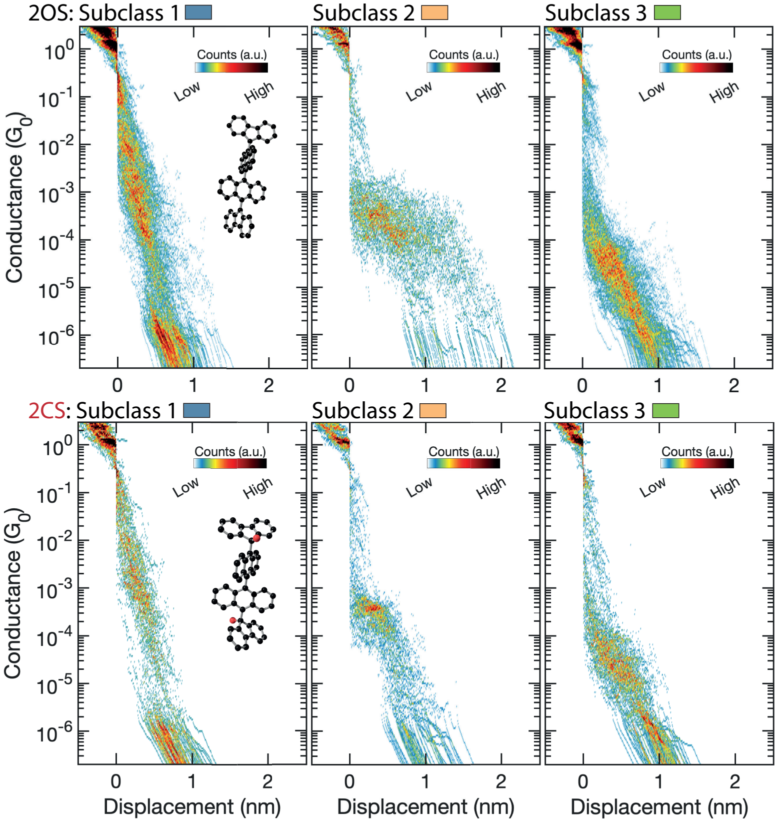

Figure 3.3: Two-dimensional conductance-displacement histogram of breaking traces of the subclass obtained from a clustering analysis on breaking traces labelled as molecular features by neural network for (top panels) 2-OS and (bottom panels) 2-CS molecules. The three subclasses extracted present similarities: (subclass 1) a high-conductance class and (subclass 3) a low-conductance class without a clear molecular plateau. Subclass two contains the longest traces with molecular features corresponding to a conductance between 10^{-3} and 10^{-4} G_0.

We repeat the procedure with the non-radical precursor 2-CS (see SI figure 3.8) and display the obtained subclasses at the bottom of figure 3.3. We note that the yield of molecular junction formation for the precursor molecule without anchoring group is almost twice smaller than that for the di-radical (see SI figure 3.6). The 2-CS classes correspond well with the subclass obtained for the 2-OS di-radical, with the difference that subclass 2 is significantly reduced in length with the precursor. To compare the shape of the intermediate conductance plateaus, we build a 1D conductance histogram for each molecule by normalizing the 1 G_0 peak height of all subclasses and display the result in figure 3.4 (top). Excluding the conductance region under 10^{-6} G_0, we fit the conductance peak of each class to a log-normal distribution. The bottom of figure 3.4 shows the results of this fit for the di-radical (right) and the precursor (left): the relative heights of the high and low-conductance features classes, respectively subclass 1 (blue) and 3 (green) are similar in both compounds. However, the extended configuration, subclass 2, displays almost twice the number of counts, with respect to the two other classes, in the di-radical experiment compared to the precursor. This figure also shows the similarities in conductance values for the different classes (e.g. comparison of the two bottom panels).

A plausible explanation for the similarities between the two molecules involves their 3D conformations: on the insets of figure 3.3 (left pannels), the conformation in the space of the two compounds is displayed (computed using geometry optimization -SCF Energy- with ORCA 5.0). The 2-OS molecule has a slightly larger length between the most distant carbon atoms due to the larger angle in the backbone axis between the fluorenyl and the anthracene units while the extra hydroxyl groups increase the contortion of the 2-CS precursor reducing its length. We note that the mechanical manipulation, in combination with bias voltage in the junction, could lead to dehydroxylation of the precursor to a single or double radical. This process most likely results in single radicals rather than bi- or di-radicals. since it is more difficult to remove for of them at the same time. This result suggests that the conductance enhancement in a radical molecular junction occurs only under specific molecule-metal configurations. The different in yield for both compounds may indicates that the di-radical center on the backbone plays a role in the stability of the molecular junction as an anchoring group. The van der Waals interactions

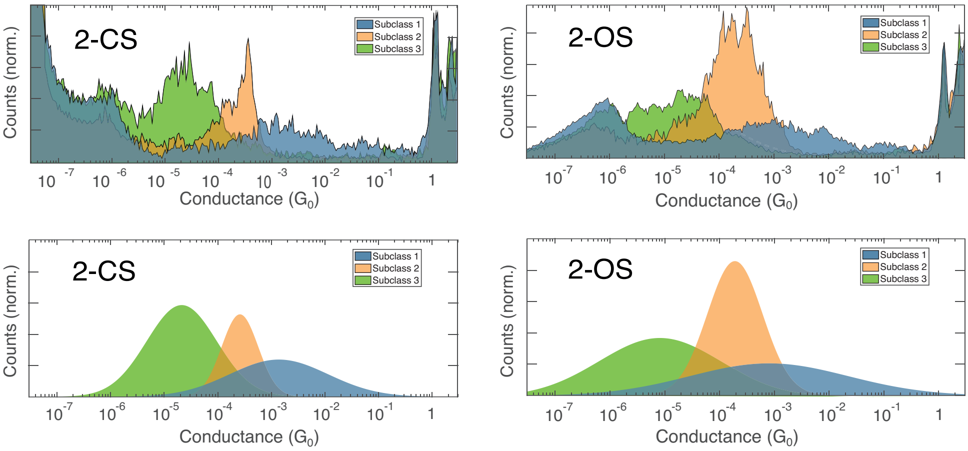

Figure 3.4: One-dimensional histograms condensing results of sub-clustering (see figure 3.3). Left pannels: the 2-CS precursor and (right pannels) the 2-OS di-radical. Both molecules display three distinct levels of conductance with a broad number of counts at higher conductance (blue) for subclass 1. The lower conductance subclass 3 (green) displays a larger number of counts (about twice in both cases) with a maximum of counts around 10^{-5} G_0. The mid-conductance subclass 2 (orange) distribution displays a smaller number of counts than the low-conductance class for the precursor, while it is twice higher in the case of the di-radical.

between the molecule and the metallic electrodes may thus be strengthened by the 3D conformation or/and by the radicals centers in the 2-OS molecule compared to the 2-CS.

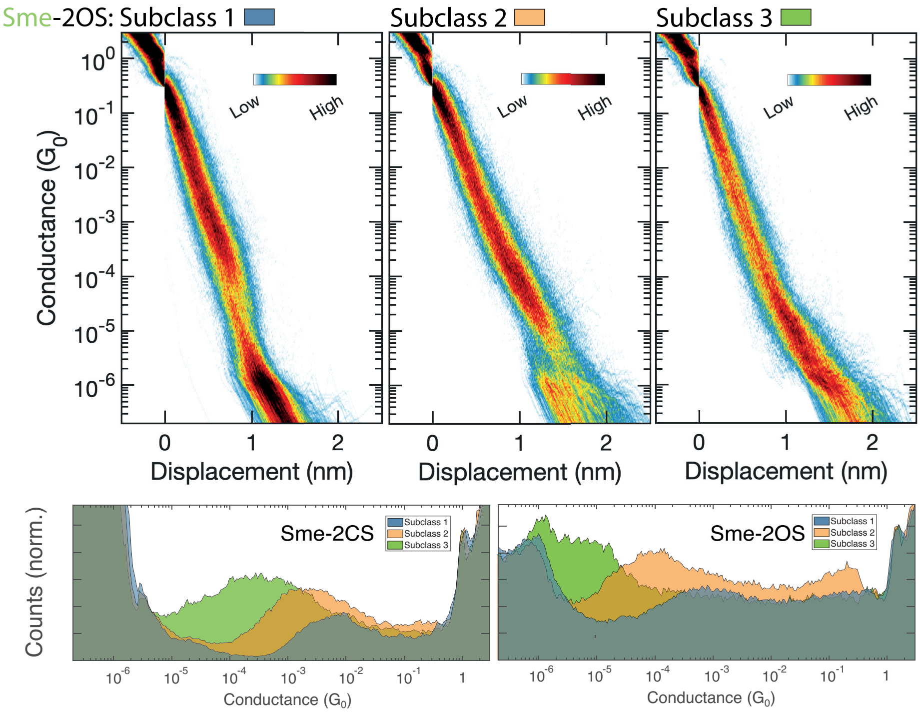

Figure 3.5: (Top) Two-dimensional conductance-displacement histogram of the subclass obtained from clustering analysis on breaking traces labelled as molecular features by neural network for Sme-2OS di-radical. (Bottom) 1D conductance histogram of the clustering analysis for Sme-2CS precursor (left) and Sme-2OS di-radical (right). Both molecule classes display a maximum number of counts (excluding amplifier kick) at a high, a low, and an intermediate conductance. This maximum is larger relative to the 1 G_0 plateau for the di-radical than for the closed shell molecule. Overall, the maximum number of counts is higher in conductance for the precursor (Sme-2CS) than for the di-radical. The Sme-2OS classes feature a flat region for conductances above the maximum number of counts of the class, which is absent from the Sme-2CS results.

We carry on the investigation by repeating the same procedure for the Sme-2OS di-radical and the Sme-2CS precursor containing the same backbone, as the 2-OS and 2-CS respectively, with the addition of sulfur-stabilizing groups. The 2D displacement-conductance histograms for the neural network analysis are displayed in the SI for Sme-2OS (figure 3.9) and Sme-2CS (figure 3.10). Note, that the yield of molecular junction formation is more than ten times larger for molecules with the sulfur stabilizing groups compared to the molecules without them. The 2D histogram for each class of the clustering analysis is depicted for the Sme-2OS di-radical in figure 3.5 (top): the histograms of the three subclasses look very similar in contrast to the 2-OS di-radical. The 2D histogram highlights a "sliding" behaviour of the molecule: no clear molecular plateau is observed in any of the classes; a slanted slope rupturing at different electrode displacements is, instead, observed in each subclass. This behaviour is observed when using up to 10 classes in the clustering analysis; the result is shown in SI figure 3.11. Similar subclassses are observed in the 2D histogram of the Sme-2CS when applying the same procedure. In order to compare the results, we built a 1D histogram following the same procedure as for figure 3.4 and display the results in figure 3.5 for the Sme-2CS precursor (bottom-left) and the Sme-2OS di-radical (bottom-right).

Both for the di-radical and the precursor, the three classes display a maximum number of counts around a high, an intermediate, and a low conductance value. The positions of these maximums are at higher conductance for the Sme-2CS compared to Sme-2CS. However, the maximum number of counts relative to the 1 G_0 plateau is larger for the di-radical than for the precursor. The 1D histograms from the Sme-CS classes (bottom-left pannel 3.5) can be fitted with a log-normal distribution (as displayed for molecules without anchoring groups at the bottom of figure 3.4).

In the di-radical 1D histogram, we observe a non negligible number of counts (more than half of the maximum number) at a high conductance for all classes, making the use of a log-normal distribution to fit the conductance peak positions less relevant. These results indicates that the di-radical does not enhance the conductivity of the sulfur-stabilized molecular junction in the extended molecule configuration. However, the larger number of features at high conductance observed in the Sme-2OS point to the radical-enhanced states at smaller electrode distances. This feature may be linked to the stabilizing group adding an extra layer of protection to the radicals centers, decreasing the probability of molecule-metal conformations quenching the radical sites with the metallic electrodes.

3.3.1. COMPARISON WITH LOW TEMPERATURE EXPERIMENTS

Dehydroxilation of the 2-CS/Sme-2CS radical has been performed at low temperatures in a scanning tunneling microscope (STM), showing that the radical can be turned from its closed-shell to its open-shell form by successive application of bias pulses through the tip brought close to the oxygen atom attached to the molecule. It has also been shown that the radical can exist with a single hydroxyl group attached to the carbon backbone, yielding a single unpaired magnetic impurity localized on the molecule (see chapter 4). In low-temperature MCBJ measurements, some molecule-metal configurations displayed a characteristic zero-bias resonance corresponding to an S=1/2 Kondo resonance arising from strong correlations between the localized magnetic impurity and the electron bath of the gold conduction bands, suggesting that the radical states can be quenched by mechanical manipulation in the proximity of the electrodes contacting the molecule close to the radicals centers (see chapter 3). When embedded in three-terminal devices, the di-radicals can be reversibly oxidized/reduced by the application of a potential on the back-gate electrode (see chapter 5). The aforementioned findings underscore the consequences of the molecule-metal geometry on the electrical properties of the junction. In particular, we observe contacting effects analogous to electrostatic gating leading to oxidation of the di-radical to a single radical (see chapter 3 and 4).

3.3.2. FLUORESCENCE SUGGEST AN UNEXPLORED SPIN-QUENCHING MECHANISM

Both 2-OS and Sme-2OS di-radicals have a red colour in the powder form, tending to pink once dissolved in a DCM molecular solution. The di-radicals 2-CS and Sme-2CS, in contrast, have a pronounced yellow colour in their powder form, while the molecular solutions are completely transparent optically. When exposed to light with a ultra-violet (UV) wavelength using a commercially available UV lamp, the molecular solutions from the precursor molecules (2-CS and Sme-2CS) revealed a fluorescent emission in the optical field perceived as blue, while this fluorescence is quenched in the open shell forms 2-OS and Sme-2OS. Thus, this observation implies that, the conversion of UV light in a larger visible wavelength, is linked to a process occuring exclusively in the precursor containing hydroxyl groups. We verified the evolution in time by lightning older molecular solutions (in DCM) that have been resting for several months up to years with the same UV source and they exhibited the same behaviour. Additionally, it suggests that oxidation of the di-radical in DCM solution does not revert to a closed-shell structure in the precursor form; instead, it leads to the formation of a distinct third molecule.

3.4. CONCLUSION AND DISCUSSION

In this study, we investigated the room-temperature transport properties of molecular junctions formed with stable open-shell di-radicals, with and without anchoring groups, and compared the results with their neutral closed-shell precursors counterparts. Employing neural network and clustering analysis methods, we observe indications of higher conductance configurations in classes labelled as molecular junctions. Conformations with plateaus around 10^{-4} G_0 conductance in both closed and open-shell molecular junctions indicate that extended conformations of the molecule in the junction have a similar conductance. We extended the investigations using molecules with the same backbone but with anchoring groups incorporated to the original compounds. The results indicate enhanced transport characteristics at high conductance ($> 10^{-3}$ G_0) and small electrode displacement in the case of sulfur-stabilized di-radical molecular junctions. In both cases we find similar behavior when comparing the closed and open-shell molecules. This suggest that either the 2-OS di-radical is oxidized to a single or non-radical molecule, or alternatively that the closed shell molecule can be reduced to a radical, by the interactions with environment or electric fields. Alongside observations of their fluorescence under UV light, we find compelling evidence for a redox reaction that oxidizes the radical's total spin number by a different mechanism than hydroxylation. This study also highlight fast-breaking room temperature MCBJ as an adequate method to select all-organic radical compounds for low-temperature studies.

3.5. APPENDIX

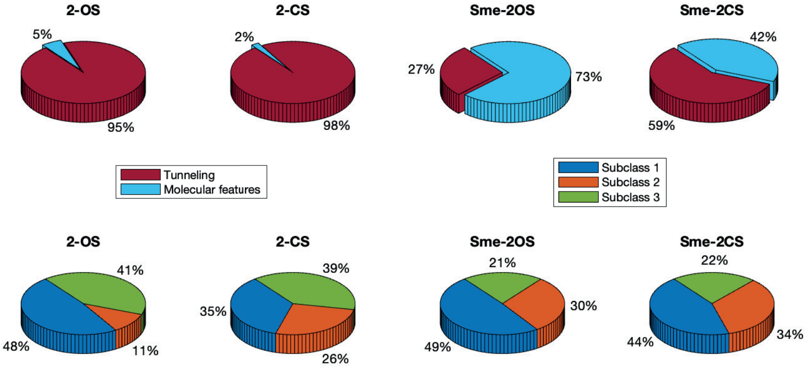

Figure 3.6: Statistics of the mechanically controlled break junctions experiments for the di-radicals without (2-OS) and with Sulfur-methyl stabilizing groups (Sme-2OS) and their respective presursors (2-CS and Sme-2CS). Top: features extracted using the neural network supervised tunneling removal. The yield of molecular junction formation with compounds with sulfur groups is orders of magnitude larger than without. Bottom: statistics of the extracted subclasses from the clustering of breaking traces with molecular features, yield is given relative to the molecular features.

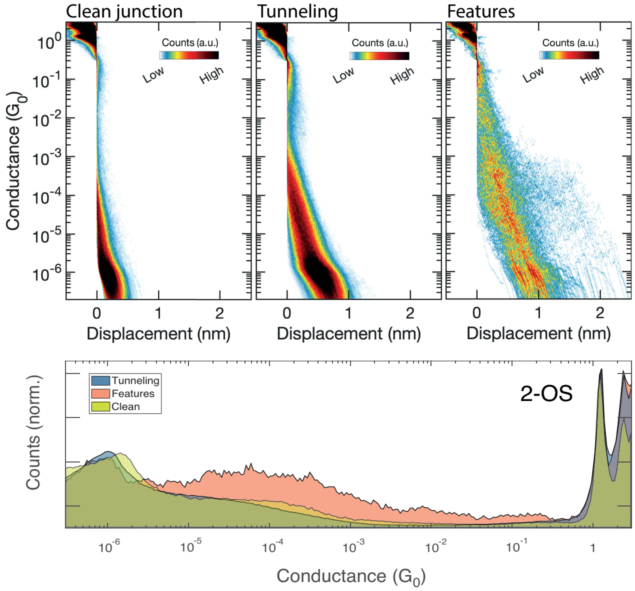

Figure 3.7: Overview of the 2-OS measurements. Top: two-dimensional conductance-displacement histogram of breaking traces: (left) before molecule deposition (traces measured on bare gold), traces labelled as (center) tunneling by neural network classification after molecular deposition and (right) extracted breaking traces containing molecular features. Bottom: corresponding one-dimensional conductance histogram of 2-OS displaying compiled data the from clean junction (yellow), tunneling (blue) and molecular features (red).

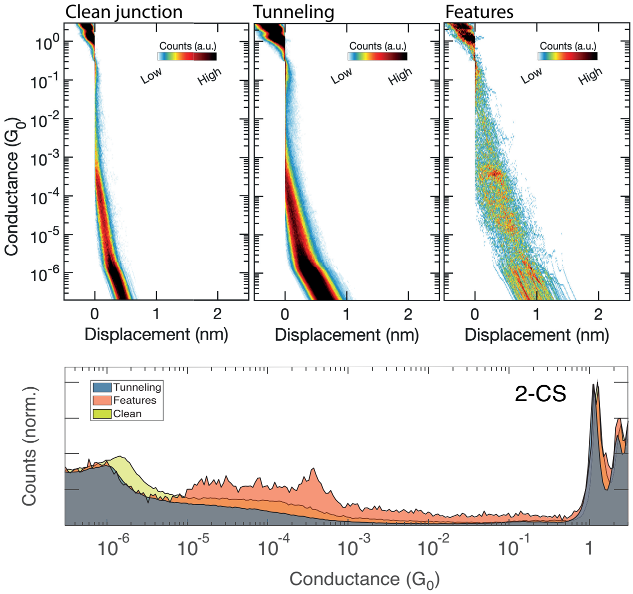

Figure 3.8: Overview of the 2-CS measurements (same figure layout as figure 3.7).

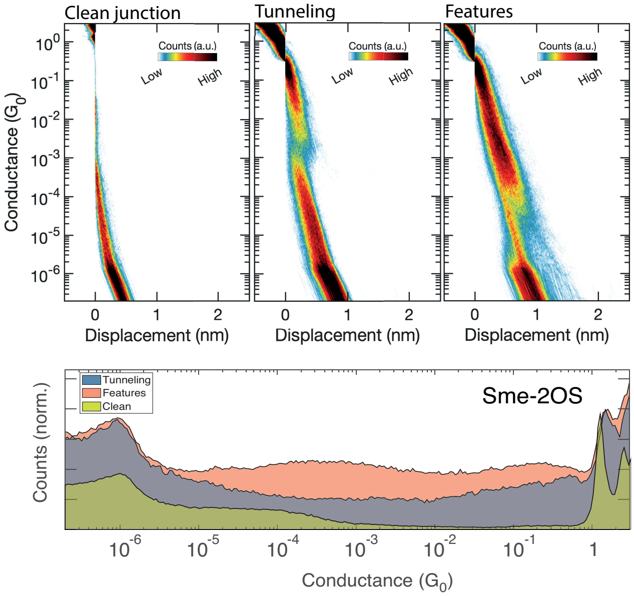

Figure 3.9: Overview of the Sme-2OS measurements (same figure layout as figure 3.7).

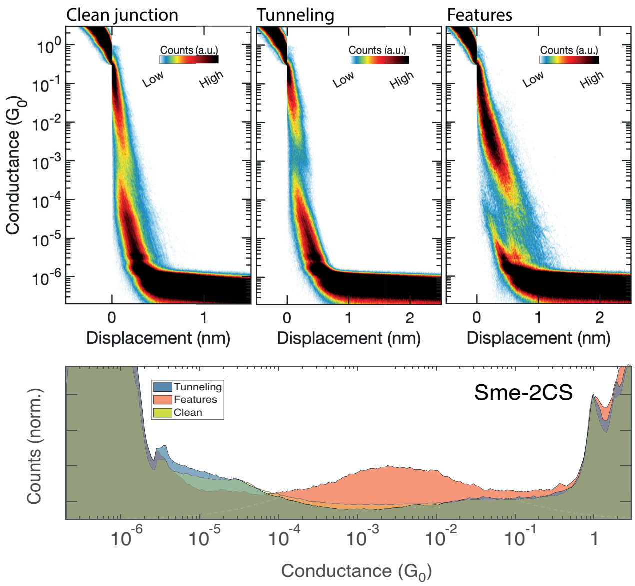

Figure 3.10: Overview of the Sme-2CS measurements (same figure layout as figure 3.7).

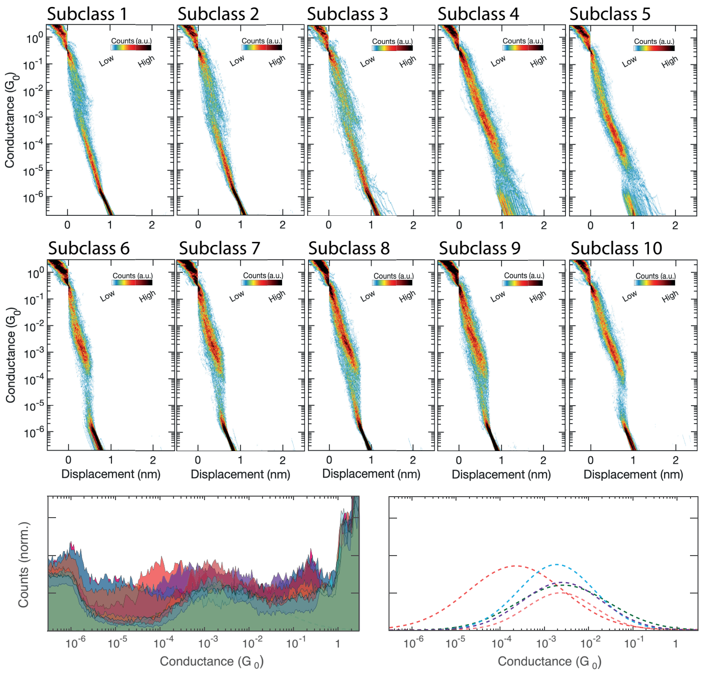

Figure 3.11: Clustering analysis on the Sme-2OS features extracted with neural network with the number of classes fixed to 10; the main text (figure 3.5) shows the results using the same data set when the number of classes is fixed to 3.

4

MAGNETIC FINGERPRINTS IN ALL-ORGANIC RADICALS MOLECULAR JUNCTIONS

> *Thus, the task is not so much to see what no one yet has seen,*
> *but to think what nobody yet has thought about*
> *that which everybody sees.*
>
> Arthur Schopenhauer

Polycyclic aromatic hydrocarbons radicals are organic molecules with a nonzero total magnetic moment. Here, we report on charge-transport experiments with bi-anthracene-based radicals using a mechanically controlled break junction technique at low temperatures (6 K). The conductance spectra demonstrate that the magnetism of the di-radical is preserved in solid-state devices and that it manifests itself either in the form of a Kondo resonance or inelastic electron tunneling spectroscopy signature caused by spin-flip processes. The magnetic fingerprints depend on the exact configuration of the molecule in the junction; this picture is supported by reference measurements on a radical molecule with the same backbone but with one free spin, in which only Kondo anomalies are observed. The results show that the open-shell structures based on the bi-anthracene core are interesting systems to study spin-spin interactions in solid-state devices and this may open the way to control them either electrically or by mechanical strain.

Parts of this chapter have been published in Nano Letters **22**, 8086–8092 (2022) by T.Y. Baum*, S. Fernández, D. Peña, H.S.J. van der Zant.

4.1. INTRODUCTION

Over the last years, atomically precise synthesis of radicals involving polycyclic aromatic hydrocarbons (PAH) has gained attention [75, 79, 80]. These open-shell graphene nanostructures exhibit π-paramagnetism which leads to more delocalized, mobile and isotropic spin states than those generated by electrons in e.g. d or f-orbitals. These newly available structures thus emerge as an ideal solution to combine spin-transport properties with large diffusion length and long coherence time. Taking advantage of these properties, organic radicals may play a key role for developing a new generation of low-power devices [24] using spin polarization instead of charge as information carrier, storage and processing.

4.1.1. MAGNETIC FINGERPRINTS

In single-molecule transport studies the magnetic signatures of a radical are typically revealed by the observation of Kondo resonances [57]. For example, previous scanning tunneling microscopy and break junction experiments focused on all-organic radicals [81] display Kondo temperatures (T_K) ranging from a few [82] K up to tens [83–85] of K. Studies on other charge transport phenomena such as magnetoresistance [86, 87] and magnetic-field induced variation of inelastic electron tunneling spectroscopy (IETS) have also been reported [88, 89].

Using IETS, spin-spin interactions in all organic di-radicals have been studied, demonstrating interesting properties such as large exchange couplings [90, 91] or ground-state inversion by electrostatic gating [92]. Here, we report on measurements of all-organic mono- and di-radical molecules in a mechanically controlled break junction (MCBJ). For this study we selected bi-anthracene-based radicals **1-OS** and **2-OS**, which are considered as stable open-shell PAHs due to the steric hindrance around the radical centers [93]. For both molecules, Kondo resonances were observed with Kondo temperatures ranging from 7 to 50 K; only for the di-radical IETS signals are found that reveal spin-flip excitation with exchange energies of about 10 mV.

The di-radical **2-OS** is composed of two fluorene moieties each hosting a C atom with an unpaired electron, linked by two anthracene units. The mono-radical version **1-OS** has the same structure without one of the fluorenes ends. Both molecules do not host sulfur-based linker groups to stabilize the binding with the electrodes; the electrode-molecule contacts thus rely on van der Waals interactions between the aromatic cycles and the gold atoms of the electrodes or the formation of Au-C bonds [94].

4.1.2. METHODS

We employed lithographically defined mechanically controlled break junctions (MCBJs) to measure the conductance of **1-OS** and **2-OS**. The substrate with the device is held in a 3-point bending mechanism at the bottom of a cryogenic stick in a vacuum chamber; measurements are performed at low temperature by plunging the stick in a liquid helium bath ($T \approx 7$ K) or in some cases in a helium dewar with a 8 T magnet. The electronic transport characteristics are measured in a two-probe scheme by applying a small voltage, V, and reading out the current, I (see Fig. 4.1b). The differential conductance $\mathrm{d}I/\mathrm{d}V$ is then computed numerically with a Savitzky-Golay filter (Fig. 4.1c-d).

We prepared a solution at ambient conditions from a small quantity of **1-OS** or **2-OS**

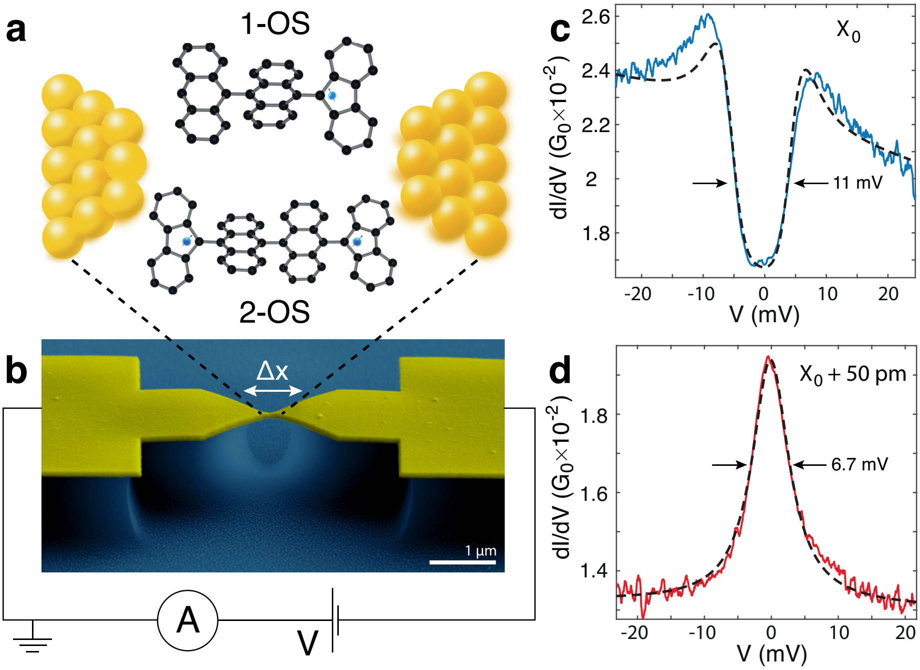

Figure 4.1: (a) Schematics of the single radical **1-OS** (upper drawing) and the di-radical **2-OS** (lower drawing) in between the electrodes of a mechanically controlled break junction (MCBJ). (b) Colored scanning electron microscopy picture of a MCBJ device. Electronic transport across the molecule is measured by sweeping the bias voltage across the electrodes while measuring the resulting current. (c,d) Typical molecular features observed in the differential conductance (dI/dV) of a **2-OS** molecule (breaking series XIV, see SI table **S1**): (c) a dip around zero-bias caused by an inelastic spin-flip excitation (dotted line: fit to the data using the model of Ref. [95]) and (d) a peak centered around zero-bias with a full width half maximum (FWHM) of 6.7 mV. The Kondo resonance (d) is obtained by increasing the distance between the electrodes from an initial position (x_0) in (c) by 50 pm.

in powder form diluted in dichloromethane (DCM) at approximately a 0.1 mM concentration. The solution is then dropcasted on the devices and the chamber of the dip stick containing the sample space is pumped to evaporate the solvent. Subsequently, the sample is cooled down by putting the dip stick in a vessel with liquid helium. The junction is then broken rapidly to the point where the gold atoms no longer link the two sides of the electrodes (we chose this point to be $G < 0.3G_0$), where $G_0 = 2e^2/h$ is the conductance quantum with e the electron charge and h Planck's constant. Afterwards, the gap spacing is increased in small steps of about 5 pm and current-voltage characteristics (IV's) are acquired at each step. The conductance of the junction is measured while separating the electrodes until the current drops below the noise level of 10^{-6} G_0. The electrodes are then pushed back together and the procedure is repeated to statistically assess different molecule-metal configurations. The IV's acquired during one stretching event belong to the same breaking trace.

4.2. RESULTS

We measured 2114 different breaking traces in five different samples with **2-OS**. In total 34805 IV's were taken from which two molecule features were identified in the $\mathrm{d}I/\mathrm{d}V$ spectra: a zero-bias peak (Fig. 4.1d) and an inelastic electron tunneling spectroscopy (IETS; Fig. 4.1c) feature with a clear suppression of the current around zero bias. Over all devices measured 55 junctions (about 2.7 % of the total) showed a zero-bias peak and 18 (about 1 %) showed an IETS signal with current suppression around zero-bias with a flat region around $V = 0$. We note that most junctions do not show molecular features either in the IV's or breaking traces: more than 50% of breaking traces showed an exponential decrease of the zero-bias conductance with gap spacing, consistent with direct, single barrier tunneling without a molecule.

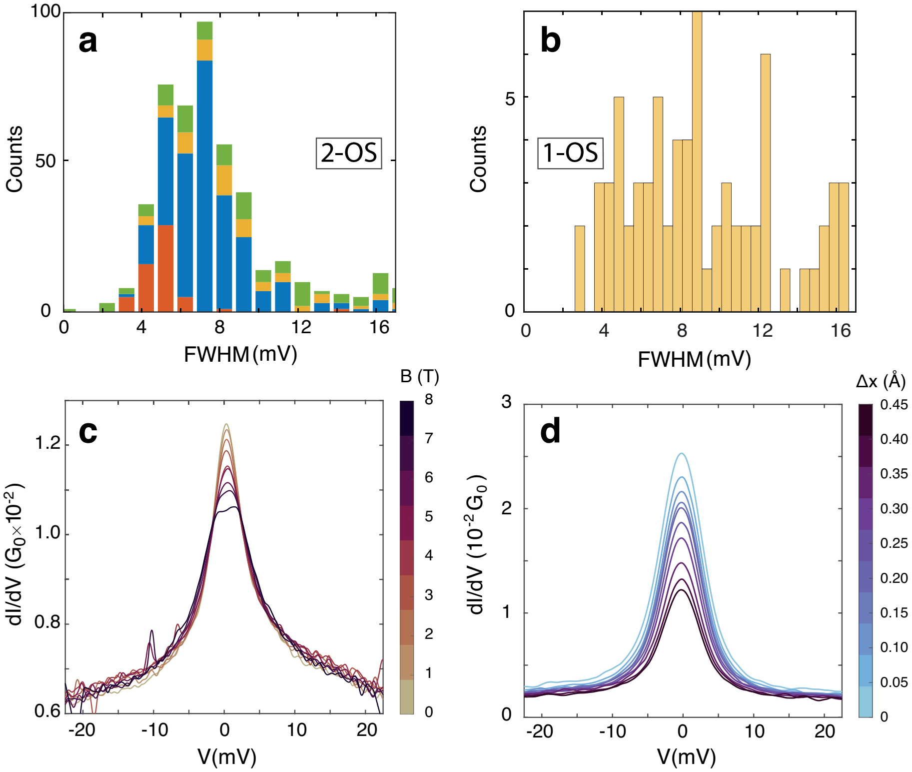

Figure 4.2: (a) Statistics on the widths of the zero-bias peaks of the **2-OS** di-radical molecule as determined from a fit of a Lorentzian function to the $\mathrm{d}I/\mathrm{d}V$ spectra. Each color corresponds to a different sample. The Kondo temperature is approximated from the extracted full-width half maximum (FWHM) using equation (4.2). The average width is 7 mV corresponding to a Kondo temperature of 34 K. (b) Same statistics as in (a) for the **1-OS** mono-radical reference measurements showing a smaller number of peaks with a wider distribution. (c) Magnetic field dependence of a zero-bias peak which has $T_\mathrm{K}(\mathrm{B} = 0) = 30$ K (measurement performed on an **2-OS** molecule, offset vertically for clarity). (d) Mechanical manipulation of a Kondo resonance measured on an **2-OS** molecule with a peak initial width at $x = x_0$ of 6.9 mV ($T_\mathrm{K} \approx 33.5$ K). The peak width and Kondo temperature reduce when increasing the spacing between the electrodes: breaking the electrodes 0.5 Å further apart yields a peak width of 6.4 mV ($T_\mathrm{K} \approx 30$ K).

4.2.1. KONDO RESONANCES

We assign the zero-bias resonance peaks to a Kondo resonance and fit a Lorentzian function to them (Fig. 4.1d):

$$f(V_0,\gamma) = \frac{1}{\pi\gamma}\left[\frac{\gamma^2}{(V-V_0)^2+\gamma^2}\right], \tag{4.1}$$

where V_0 is the resonance center taken to be zero and 2γ is the full width half maximum (FWHM). The FWHM is used to approximate [57] the Kondo temperature, T_K:

$$\mathrm{FWHM} = \frac{2}{e}\sqrt{(\mathrm{k_B}T)^2+2(\mathrm{k_B}T_\mathrm{K})^2}, \tag{4.2}$$

where k_B is the Boltzmann constant, and T is the sample temperature. We apply this fitting to each $\mathrm{d}I/\mathrm{d}V$ with a zero-bias peak and the results for the FWHM are summarized in Fig. 4.2a. Most FWHMs lie between 4 and 10 meV corresponding respectively to a Kondo temperature of 7 and 50 K; the variation indicates that the electronic coupling between the spin and the metal electrode can differ substantially. A Kondo temperature of a few tenths of K is typical for resonances observed in molecular devices [96, 97] but is large compared to values found for spin-1 molecules [98].

We also measured 4235 breaking traces in the presence of the **1-OS** single radical (see Fig. 4.1a). We observed zero-bias peaks in 107 breaking traces (about 2.5 %). A fraction of the resonances had a FWHM value similar to that of the **2-OS** molecule (see Fig. 4.2b); some zero-bias features, however, exhibit a larger FWHM in the range of 20−30 mV. Most likely, these do not originate from Kondo physics and we speculate that they correspond to transport involving a nearby resonance (see appendix, Section II-c).

When applying a magnetic field, B, one expects the Zeeman energy to compete with the Kondo temperature thereby lifting the degeneracy of the spin states involved in transport through the molecule. This competition leads to a splitting of the zero-bias resonance by approximately $2\mathrm{g}\mu_\mathrm{B}B$ where $\mathrm{g}=2$ is the g-factor of the electron spin and μ_B is the Bohr magneton. In the strong coupling limit ($T \ll T_\mathrm{K}$) this splitting is expected to take place beyond the critical field, B_c given by: [57, 99, 100] :

$$B_\mathrm{c} = \frac{1}{2}\frac{\mathrm{k_B}T_\mathrm{K}}{g\mu_\mathrm{B}}. \tag{4.3}$$

Applying this formula to the Kondo resonance displayed in Fig. 4.2c, B_c would be 11 T. In our set-up, the maximum magnetic field available is $B = 8$ T and with this field, we could not split the Kondo resonance, consistent with the single spin-$\frac{1}{2}$ Kondo physics discussed (Eq. 4.2).

Typically, a single breaking trace shows a few IV's with zero-bias anomalies; in some cases, the junction is more stable during stretching of the device allowing the zero-bias anomaly to be measured over distances up to 0.5 nm. An example is shown in Fig. 4.2d where the width and height of the peak decrease when the separation increases between the electrodes. At the same time, the average conductance background of the spectra also decreases because direct tunneling between the electrodes is reduced. In Fig. 4.2d, the FWHM decreases by about 10% whereas the height decreases by about 50%. This behavior is consistent with a lowering of one or both electronic molecule-electrode couplings when moving the electrodes apart.

4.2.2. INELASTIC SPIN-FLIP SPECTROSCOPY

We now turn the analysis to the step-like increases of the conductance in the dI/dV spectra (Fig. 4.1c). These signals indicate the opening of an inelastic spin-flip tunneling channel via an excited state of the molecule. For the **2-OS** system this is the singlet-triplet excitation with the corresponding energy scale, J_{ex}, of the two-spin system formed by the unpaired electrons of the di-radical molecule. We fit the Ternes model [95], a model commonly used in the scanning tunneling microscopy community, to the data as shown in Fig. 4.1c (fits are the dotted lines). We note that these IETS spectra were not observed for the **1-OS** molecule, pointing to the importance of the presence of two spins for its observation.

We have extracted J_{ex} from the fits of the IETS signals and plot their absolute values in Fig. 4.3a; see SI for additional spectra and the fit parameters (Table **S1**). Most counts are around an energy of 11 meV, close to the value found in SQUID magnetometry [93]. The IETS signal from Fig. 4.3b was stable enough for magnetic field measurements. The magnetic field lifts the degeneracy of the triplet state and changes the excitation energy depicted in the inset of Fig. 4.3c. The lifting of degeneracy initially suppresses the small zero-bias contribution and a step appears around zero-bias above 3 T. The same data are shown in the colormap of Fig. 4.3c where the corresponding transitions are depicted by white arrows. The transitions correspond to an open-shell triplet ($S = 1$) ground state with a singlet ($S = 0$) excited state (ferromagnetic coupling). This behavior is well captured by the Ternes model (dotted lines of Fig. 4.3b) but in the data a larger suppression of the current around zero-bias is present compared to numerical simulations (more details can be found in 4.4).

We observe a range of singlet-triplet energy gaps ranging from 7 to 14 meV. The magnetic field measurement from Fig. 4.3b-c shows that the exchange coupling of the spins in this device is ferromagnetic. Within the Ternes model, the small zero-bias enhanced conductance is also explained by having a triplet ground-state due to higher-order Kondo contributions. On the other hand, two IETS spectra show a conductance overshoot at the step-edges in the absence of zero-bias increases (as in Fig. 4.1c). These overshoots may be an indication of an anti-ferromagnetic ground state (no magnetic field measurements were performed on these samples) and are further discussed in supplementary information II-b.

In the **2-OS** molecule, the two anthracene units linking each moieties hosting an unpaired electron have a rotational degree of freedom that impacts the overlap of the two unpaired electron wavefunctions [101]. This effect can result in different values of the exchange coupling between them. The hybridization with the electrodes producing the Kondo resonances can also contribute to the delocalization of the unpaired electrons and thus modify this overlap. A variation of the exchange coupling and change of sign have been observed in other organic radicals [92] where both ferromagnetic and anti-ferromagnetic ground states were found indicating that the conformation of the molecule is important in determining the spin-spin interactions on it. The large magnitude of the exchange coupling in the **2-OS** molecule is in contrast with previous measurements where values are one order of magnitude lower [102, 103]. Similar values of the exchange coupling in an $S = 1$ di-radical system have been reported for a triangulene dimer [90], highlighting the magnetic properties of free electrons in carbon lattices.

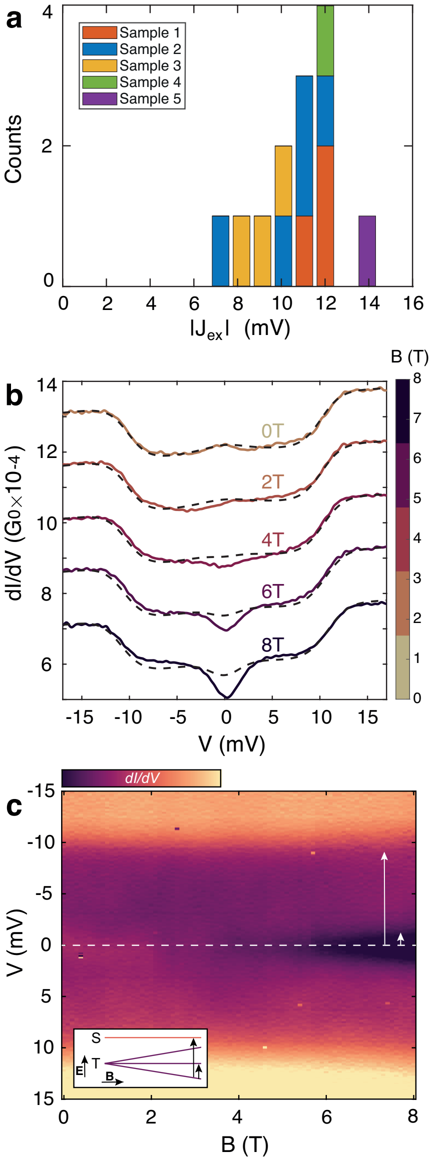

Figure 4.3: (a) Histogram of the exchange coupling values determined from IV's displaying an IETS signal. Most of the observed transitions are around 10 mV, close to the value measured in the bulk using SQUID magnetometry [93]. (b) Measured inelastic tunneling spectra (solid colored lines) are fitted to the Ternes model [95] (black dashed lines) at different values of the applied magnetic field (**2-OS** molecular breaking series I, see Table **S1** in SI for the fit parameters). The step opening at zero bias corresponds to a new transition allowed by lifting the degeneracy of the triplet ground state. (c) Colormap of the magnetic field sweep corresponding to (b). Inset shows the evolution in a magnetic field of the energy of the triplet (T) and singlet (S) states; black arrows correspond to the transitions indicated by white arrows in the chap4 panel.

4.3. CONCLUSION

The two magnetic fingerprints discussed depends on the molecule-electrode geometry. The geometry defines the charge injection points into the molecule (see Fig. 4.4). The absence of specific anchoring groups may allow for a larger range of electronic coupling in the junction compared to sulfur-anchoring group containing molecules. Configurations with strong molecule-electrode coupling involving transport across one of the unpaired spins induce $S = 1/2$ Kondo resonances in the $\mathrm{d}I/\mathrm{d}V$ spectra. With a small gap between the electrodes, several configurations may involve electron pathways interacting mainly with one of the radical centers. Fewer configurations of the molecule bridging the electrodes are possible at larger distances favoring an extended molecule configuration; electrons flowing through the molecule in this configuration interact with both radical centers leading to spin-flip $S = 1$ features in the spectra.

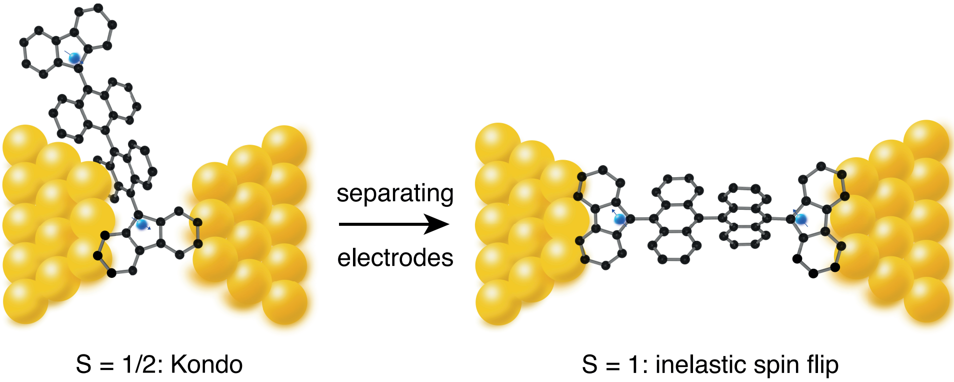

Figure 4.4: At small electrodes distances, the geometry of the molecule in the junction allows injection at several points into the molecule; some configurations may only involve transport across one radical center giving rise to spin-$\frac{1}{2}$ effects in the $\mathrm{d}I/\mathrm{d}V$ spectrum. At larger distances between the electrodes, fewer configurations of the molecule bridging the two electrodes are possible. This favors an extended molecule configuration in the gap as shown on the right. The electrons flowing across the junction interact with both radical centers leading to spin-flip features in the differential conductance spectrum.

In summary, we contacted PAH radical molecules in solid-state devices. We show that the free electrons of these radicals are preserved after integration in mechanically controlled break junctions and the open-shell character persists against mechanical manipulation. We observed spin-1/2 Kondo resonances in the electronic transport spectra of both the mono- and di-radicals and spin-1 inelastic spin-flip effects for the **2-OS** devices only. The exchange coupling of the di-radical was found to be in the range of 10 meV with predominantly a triplet ground-state. The MCBJ technique allows to probe different molecule-metal configurations so that an extended picture of the behavior of the radical molecules in a solid-state device is obtained. Understanding the associated variations in parameters is important for future use in these devices. From a fundamental point of view, the robustness of the radicals and the different physical effects highlight these systems as excellent models for the investigation of magnetic effects on electronic transport at the single-molecule scale.

4.4. APPENDIX

4.4.1. REFERENCE MEASUREMENT

In the same conditions, we made reference measurements on clean mechanically controlled break junctions (at liquid helium temperature). Overall, on 600 breaking traces and 7185 IVs, none show a molecular feature in the spectra such as a zero-bias peak or an IETS-like signal.

4.4.2. FITS OF IETS SPECTRA 2-OS

We use the scilab code provided in ref. [95] to fit the IETS spectra using the following parameters in the model:

- Physical parameters
  - J_{ex}: exchange coupling (in mV)
  - T_{eff}: effective temperature (in K)
  - $J\rho_{\mathrm{s}}$: Kondo scattering term
  - T_0^2: the tip-sample interaction strength (linked to the electronic coupling, Γ, in our case)
  - g: g-factor of the spin, which has been taken to be 2 for all fits
  - $B_{\mathrm{X,Y,Z}}$: magnetic field along the corresponding X, Y, Z axis (in T)
- Data offset parameters
  - b: additional background slope
  - V_{off}: additional voltage offset
  - σ_0: additional background conductance

The values of the parameters used to fit the IVs displaying an IETS signals are collected in Table **S1**. In total 14 breaking traces have been considered. For breaking series I the parameters at different magnetic fields are given. The corresponding fits are the ones shown in Fig. 4.3b of the main text.

For fitting, we set the program to use both 3rd order and enable interactions of electrons which originate and end in the same electrode (checkbox called 3rd order scattering with other spin systems in the program). Most spectra can be fitted using a negative exchange coupling (ferromagnetic coupling/triplet ground state), and most are better fitted without including the rates equations in the model. Thus, the two spectra with a positive exchange coupling (anti-ferromagnetic coupling/singlet ground state) are described by the model with large bias overshoots (shown in Fig. 4.1c of the main text and Fig. 4.5b that are better fitted including the rates equations. Another indication for triplet ground state spectra is the zero-bias conductance enhancement (Fig. 4.3b of the main text and Fig. 4.5a that can be captured by the model using a ferromagnetic exchange coupling.

We fix the value of the g-factor to be 2 in all of the fits as a different value in the carbon lattice of PAH is unlikely. The value $g = 2$ is the best fit to capture the evolution

Breaking series	**Fit parameters**								
I	J_{ex} (mV)	T_{eff} (K)	J_{ρ_s}	T_0^2	b	V_{off} (mV)	σ_0	Δx (Å)	inc. rates
B = 0 T	-10.14	6.8	-0.02	0.0012	0.0017	0	0.435		no
B = 1 T	-10.14	6.8	-0.02	0.0012	0.0017	0	0.435		no
B = 2 T	-10.14	6.8	-0.02	0.0012	0.0017	0	0.435		no
B = 3 T	-10.14	6.8	-0.02	0.0012	0.0017	0	0.435		no
B = 4 T	-10.14	6.8	-0.02	0.0012	0.0017	0	0.435		no
B = 5 T	-10.14	6.8	-0.02	0.0012	0.0017	0	0.435		no
B = 6 T	-10.14	6.8	-0.02	0.0012	0.0017	0	0.435		no
B = 7 T	-10.14	6.8	-0.02	0.0012	0.0017	0	0.435		no
B = 8 T	-10.14	6.8	-0.02	0.0012	0.0017	0	0.435		no
II-1	-12.7	7.2	0	4	-0.0006	-0.78	0.15	0	yes
II-2	-12.7	7.2	0	4	-0.0006	-0.78	0.15	0.15	yes
III-1	-12.1	7.2	0	1.8	-0.0019	-0.39	0.75	0.47	no
III-2	-11.5	9.7	-0.08	1.3	-0.0015	-0.39	1.15	0.63	no
III-3	-11.2	7	-0.04	1.3	-0.0015	-0.69	1.15	0.79	no
III-4	-11.2	7	-0.01	1.7	-0.0014	-0.69	0.85	0.94	no
III-5	-10.5	7.7	0	2.93	-0.0005	-0.69	0.33	1.10	no
III-6	-10.5	9.7	0.05	1.7	-0.0008	-0.87	0.86	1.26	no
IV	11.5	6.8	0	4.79	0	-0.4	0.24		yes
V	6	9	0	1.5	-0.004	-0.37	0.99		yes
VI-1	-9.04	8.3	0	0.78	0.0019	-1.16	2.24	0	no
VI-2	-9.04	8.3	0	0.78	0.0013	-0.76	2.24	0.10	no
VII	-11	7	0	3.63	-0.0102	0	0.28		yes
VIII	-11.5	7	0	10.57	0.005	-2.7	0.17		yes
IX-1	-11.4	15.4	0	19.2	0	-0.58	-0.24	0	no
IX-2	-11.1	15.4	0	20	0	-0.73	-0.26	0.09	no
IX-3	-10.9	15.4	0	21.5	0	-0.73	-0.24	0.19	no
IX-4	-10.9	15.4	0	21.5	0	-0.73	-0.24	0.29	no
IX-5	-10.6	15.4	0	21.6	0	-0.73	-0.24	0.39	no
IX-6	-10.6	15.4	0	21.6	0	-0.73	-0.24	0.49	no
IX-7	-10.6	15.4	0	21.6	0	-0.73	-0.24	0.58	no
X-1	-8.3	10	0	0.003	0.002	-1.53	3.8	0	yes
X-2	-8.6	10	0	0.003	0.002	-1.53	3.7	0.09	yes
XI-1	-7.05	11.5	-0.03	0.039	0	-0.47	0.112	0	no
XI-2	-6.94	9.93	0	0.035	0	-0.3	0.2	0.08	no
XII	-9.7	7	0	0.099	0	0.08	0.036		no
XIII-1	-12	9.9	-0.055	0.028	0.0012	-2.16	2.06	0	no
XIII-2	-12	9.9	-0.055	0.028	0.0012	-2.16	2.12	0.12	no
XIII-3	-11.5	9.9	-0.045	0.028	0.0012	-2.12	2.15	0.22	no
XIII-4	-12	9.9	-0.045	0.028	0.0012	-2.1	2.16	0.22	no
XIII-5	-12	9.9	-0.045	0.028	0.0012	-2.1	2.16	0.22	no
XIII-6	-12	9.9	-0.045	0.028	0.0012	-2.1	2.16	0.22	no
XIV	-14.2	10.7	0.008	0.011	-0.0004	-0.34	0.095		no

Table 4.1: Fit parameters of the Ternes model for 14 breaking traces. Each IV fitted is labelled with its breaking series number (Roman numbers) and an integer number in case more IV are measured for the same breaking series. Δx corresponds to the electrode displacement in Ångstrom with respect to the first IV of the series (with value 0). The other fit parameters are defined in the text, see previous page.

of the steps in the dI/dV spectra around 10 meV at different magnetic fields (IV with series number I, shown in Fig. 4.3b of the main text) but the opening of the zero-bias dip is better reproduced with a value larger than 2. In the Ternes model, the g-factor is the only parameter that has an effect on the width and height of the zero-bias dip (in the

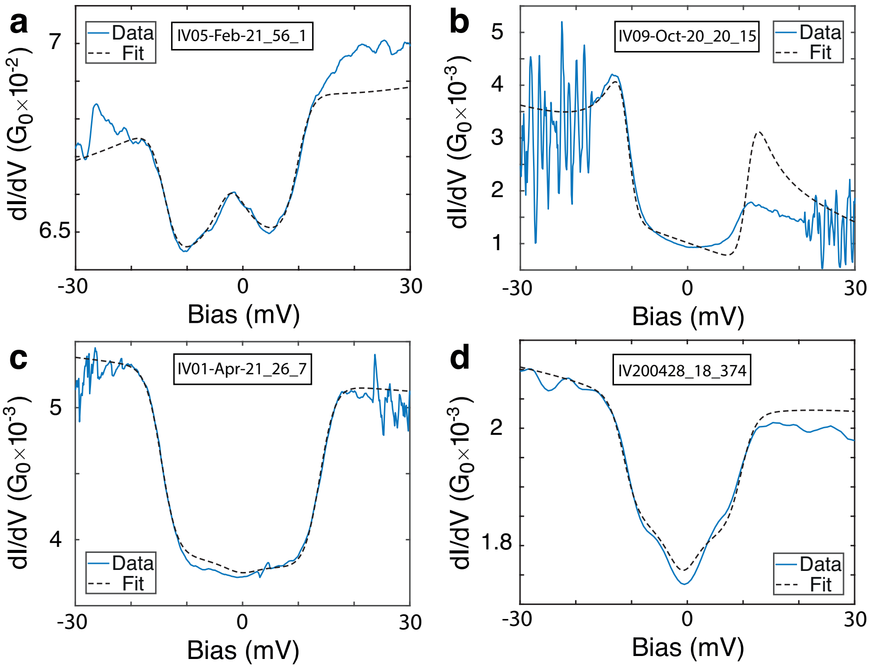

Figure 4.5: Four $\mathrm{d}I/\mathrm{d}V$ spectra from different breaking traces. a) $\mathrm{d}I/\mathrm{d}V$ from series XIII-1 with zero-bias contributions ascribed to a triplet ground state. b) $\mathrm{d}I/\mathrm{d}V$ from series VII with large bias overshoots at the steps positions indicating a singlet ground state. c) $\mathrm{d}I/\mathrm{d}V$ from series XIV can be both fitted with a singlet and a triplet ground state. d) $\mathrm{d}I/\mathrm{d}V$ from series III-6 with another step opening around zero-bias with stretching; this feature can be reproduced in the model using a positive Kondo contribution J_{ρ_s}.

case of ferromagnetic couplings between the spins) but its origin may not be captured in the perturbative approach of the model. Most of the temperatures deduced from the model are consistent with our estimation of 7 K, but some of them are higher (IV with series number IX-1 with 15 K for example). The temperature during the measurement of a single breaking trace is stable.

The exchange coupling, J_{ex}, is almost constant across a breaking series as can be seen in Table S1. In the series III-1 to 6, J_{ex} decreases from -12.1 mV (with a large Kondo contribution around zero bias) to -10.5 mV (without this Kondo contributions). This is also seen in the IV's from breaking series IX-1 to 7 where the exchange coupling starts at -11.4 mV to end with a value of -10.6 mV.

The slope of the background conductance is captured by the b parameter, introducing an asymmetry over the bias voltage range. This asymmetry is also present in the high bias-range, beyond the IETS steps. Inside the steps, the slope is different and no parameters in the model allow to reproduce this feature. The same applies to asymmetries of the zero-bias features. In particular, the bias overshoots present an asymmetry with different amplitudes for the overshoots (see Fig. 4.5b).

We observe the opening of a step around zero bias in the spectra of Fig. 4.5d with mechanical stretching reminding the effect of Fig. 4.3b of the main text without magnetic field applied. This step can be reproduced in the Ternes model using a positive Kondo scattering term J_{ρ_s}. The same is used for the IV from breaking series XIV in Fig. 4.5c.

4.4.3. 1-OS MONORADICAL

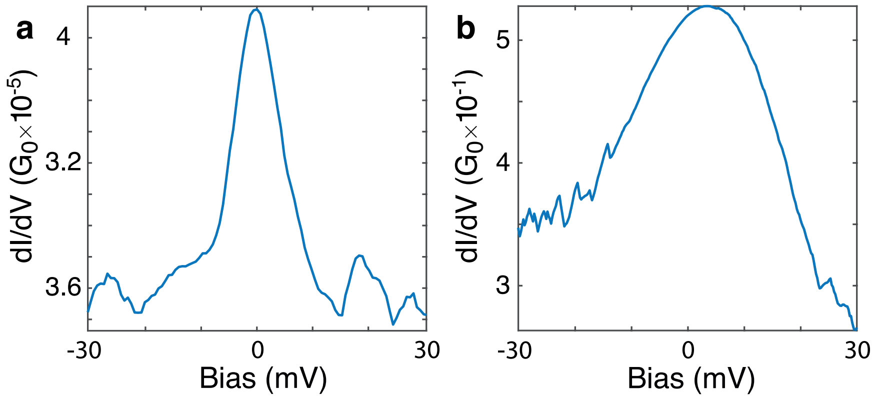

Figure 4.6: Two zero-bias resonances in the dI/dV spectra for two different breaking traces with an 1-OS molecule. The resonance on the left has an FWHM of 7 mV corresponding to a Kondo temperature of 34 K, while the peak on the right is more asymmetric and has a width of 23 mV (T_K = 131 K). The left spectrum is compatible with Kondo physics while the right one most likely does not originate from the same physics (see discussion in the text).

In the 1-OS molecular junction we also observed zero-bias peaks in the dI/dV spectra measured. A typical resonance is shown in Fig. 4.6a with a FWHM in the same energy range as features observed in 2-OS molecular junctions (around 7 meV). However, the range of the FWHM extracted from the fits of these spectra is larger than that displayed in Fig. 4.2b of the main text. An example is shown in Fig. 4.6b where the resonance is found to have an FWHM of 23 meV corresponding to Kondo temperatures of hundreds of K. Most likely, these signals do not arise from Kondo physics and are thereby excluded from the main text figure.

We also observe that mechanical manipulation of the zero-bias peak can shift the center of the resonance with electrodes spacing (see 4.7); as a consequence the center is no longer found at $V = 0$ (see Fig. 4.6b and 4.7). This behaviour is different from the observations for the 2-OS molecule where the width and height of the peak reduces while the center of the resonance stay close to zero-bias (as shown in Fig. 4.2d of main text). Another interesting feature of the 1-OS measurements is the presence of the large peaks in the spectra, symmetrically located around zero bias as shown in Fig. 4.8a. In some spectra, a small zero-bias resonance between these large structure was present (see Fig. 4.8b) which could indicate the presence of a Kondo resonance.

The features in the aforementioned paragraph can be explained by the proximity of an energy level close to the Fermi energy. When this energy level approaches the Fermi level of the electrodes, enhancement of the conductance through the molecule appears in the IV's. This energy level alignment depends on the injection point of charge carriers in the molecule and on the conformation in the junction; consequently, not all IV's

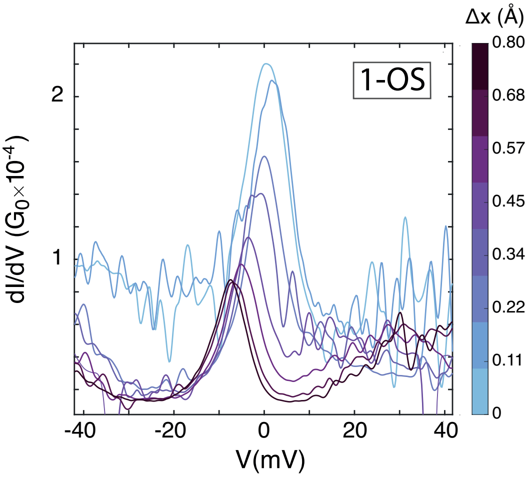

Figure 4.7: Breaking series from 1-OS reference measurement displaying a zero-bias resonance persisting along with the stretching of the electrodes. The center of the resonance is shifting from 0 mV on the first IV of the series to −8 mV after breaking the electrodes 0.8 Å apart. This result is different from the comportment observed for the 2-OS Kondo feature displayed in Fig. 4.2d of the main text.

exhibit this behavior. It would be interesting to understand which configurations lead to this better level alignment. Future work and calculations are needed to address this crucial aspect in single-molecule electronics.

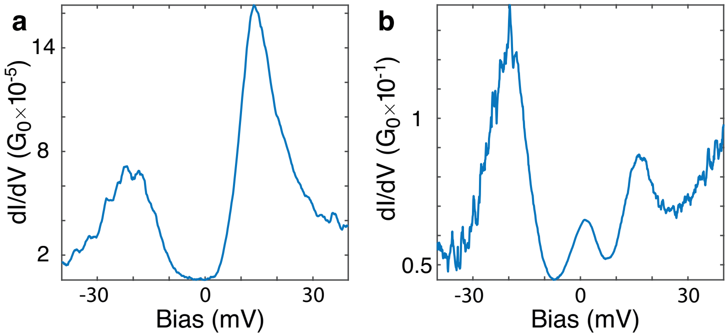

Figure 4.8: Two dI/dV spectra with resonant structures, symmetric with respect to zero-bias at different positions of the same breaking traces of 1-OS molecular junctions. The right spectrum also shows a zero-bias resonance which may be an indication that the 1-OS molecule has an odd number of electrons ($S = 1/2$ Kondo).

5

SPINS SIGNATURES OF ALL-ORGANIC DI-RADICALS IN THREE-TERMINAL MOLECULAR JUNCTIONS

C'est avec la logique que nous prouvons
et avec l'intuition que nous trouvons.
-
We prove with logic
and we find with intuition.

Henri Poincaré

In the previous chapters, the measurements were carried out using the mechanically controlled break junction (MCBJ) and the scanning tunneling spectroscopy (STS) techniques. In that case, transport through the molecule is probed in a two-terminal configuration. This chapter focuses on measurements using the electromigration break junction (EMBJ) technique, in which a gate electrode has been integrated. Both methods display similarities in the differential conductance (dI/dV) spectra confirming the similitude between the geometries observed in the two systems. The correspondence is remarkable, especially given the absence of systematic studies comparing the transport characteristics obtained with both techniques. We hereby note that the precise geometry of each molecular junction is different, leading to variations in the coupling with the electrodes and in the overall electrostatic environment experienced by the molecule, which defines the precise features observed in the device.

5.1. INTRODUCTION

All-organic polycyclic aromatic hydrocarbons (PAH) radicals have seen a continuously growing interest in the last decade both for their fundamental aspects [104, 105] and potential application [106–109]. Despite the early reported synthesis in the 1900 [110], only the recent advancement in atomically precise bottom-up synthesis of carbon nanostructures allowed to obtain these compounds with sufficient purity for the study of their outstanding properties, such as large delocalisation of their charges, long coherence time and preservation of their radical character up to room temperature [93, 111]. The absence of metallic compounds in these molecules (in opposition to single-molecule magnets) leads to a magnetism originating from semi-filled π-orbitals, which is more delocalised and isotropic than that from d or f-orbitals.

Investigations with scanning tunnelling microscopes (STM) on radicals conducted at the individual molecule scale focus mainly on π-extended nanographene structures adsorbed on metallic [112–114] surface, or more recently on insulating substrates [115–117]. Neutral organic radical molecules have also been integrated into solid-state devices and showed remaining magnetism in molecular junctions by detection of Kondo resonances and spin-flip spectroscopy signals at low-temperature both in two and three-terminal devices [82, 118] and displayed properties such as redox gating of the exchange interactions [88], or exchange coupling inversion controlled with gate voltage [92]. However, studies comparing different investigation tools using the same molecular system still need to be carried out.

In this chapter, we report on the detection of unpaired spins in all-organic di-radical molecular junctions in a three-terminal solid-state device geometry. The magnetic properties of the di-radical (see 2OS schematic in figure 5.1.b) and its sulfur-methyl stabilised derivative (SMe-2OS in figure 5.1.c) are probed through the observation of Kondo resonances originating in the strong coupling between at least one of the magnetic impurities and the conduction electrons in the leads [56, 57] and inelastic spin-flip spectroscopy signals indicating that the di-radical character of the molecule remains in specific configurations once integrated in a solid-state device. The similarity of the results with the di-radical measurements in the STM(cite stm pickup here) and mechanically controlled break junction (MCBJ) [76] geometries is discussed.

The three-terminal electromigration break junction (EMBJ) technique allows electrostatic control of the molecule's spectra, independently from the Fermi energies in the leads [119]. The possibility to push an energy level of the molecule across the Fermi level of the electrodes, thereby crossing a charge degeneracy point, depends on the molecule / gate coupling, which relies on the exact position of the molecule in the junction relative to the electrodes and the gate [120]. The result is that only one charge state can be accessed in some cases 5.3, while in others, the gate voltage can be used to switch between two ground states with the addition of one electron (or hole) (see section 5.2.2 and chapter 6).

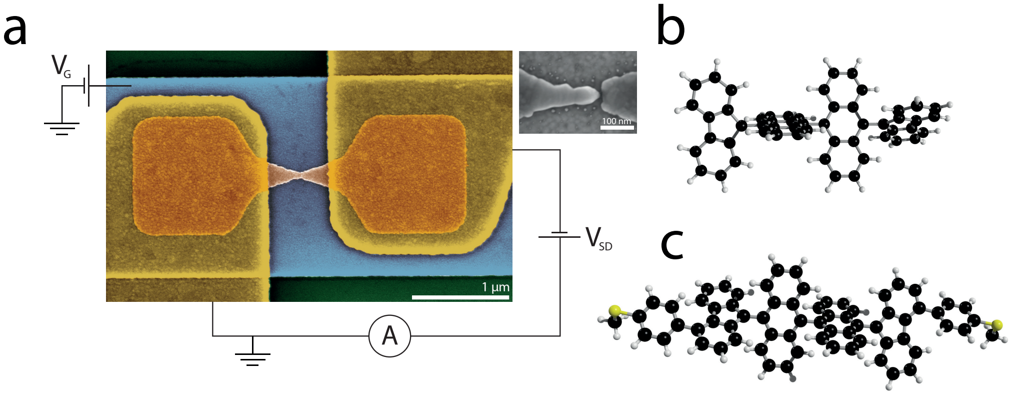

Figure 5.1: (a) Scanning electron micrography of an electromigration break junction (EMBJ) device. A 10 nm thick gold layer (orange) deposited in a bowtie shape on top of a palladium gate (blue) insulated by a few nm aluminium oxide layer. A nanometer sized gap is opened in the gold bowtie using a feedback-controlled electromigration and self-breaking procedure (top-right insert). (b,c) Representation of the two all-organic di-radical used to form 3-terminal molecular junction with (c - Sme-2OS) and without (b - 2OS) sulfur-methyl anchoring groups. The sulfur atoms in (c) are colored in yellow.

5.1.1. ELECTROMIGRATED DI-RADICAL JUNCTIONS: FABRICATION AND MEASUREMENT SET-UP

Electromigration break junction (EMBJ) and mechanically controlled break junction (MCBJ) devices operate by opening a nanometer-sized gap in gold electrodes to trap a molecule between the source and drain electrodes. Still, there are some critical differences in their designs and operations. In a MCBJ, the geometry and the tunnel/capacitive couplings can be modified by adjusting the distance between the electrodes [76]. In the EMBJs, the gap opens using the feedback-controlled electromigration technique [121–123] and self-breaking [124] procedure which does not allow for changes in the molecule-metal geometry without risking irreversible damage to the junction. Consequently, we only measure a few molecule-electrodes geometries using EMBJ devices while hundreds to thousands are explored in a single MCBJ experiment.

EMBJs are fabricated on a silicon substrate by depositing a thin layer of gold in a bowtie shape on top of a palladium gate, insulated from this gate electrode using an aluminium oxide deposited by atomic layer deposition (ALD) of less than 10 nm thickness (see Figure 5.1). Using a local gate close to the measured molecule in the junctions allows for a significant change in the electrostatic environment of the molecular junction (i.e., a large capacitive coupling α between the captured molecule and the local back-gate) compared to devices using a silicon doped substrate buried under few hundreds nanometer of silicon dioxide called a global back-gate. Using the capacitor formula $C = \frac{\epsilon A}{d}$, we see that the capacitance scales proportionally to the area A and inversely proportional with the distance d between the two conductors, in this case, the molecule and the local gate. ϵ is the dielectric constant of the dielectric layer. The area of the molecules studied is typically nanometer-sized, way smaller than devices using two-dimensional materials, which for example, can reach micrometers up to millimeters scale. These parameters highlight the importance of the insulator thickness; ALD is necessary to obtain a thin, uniform, high-quality dielectric insulating film. Finally, another adjustable parameter is the dielectric constant of the insulator ϵ, which can be tuned by choosing a specific insulating oxide constrained by the deposition technique employed.

The devices are loaded in a measurement system equipped with a 1 K pot, allowing for monitoring and controlling the temperature during the electronic transport measurements (in the range of 1.8 to 100 K, as for higher temperatures, the junctions are unstable). A perpendicular (out of the sample plane) magnetic field can be applied up to 9 T. The gap is opened in the gold bowtie by ramping a current up and down between a maximum and a minimum bias voltage value through the device while gradually increasing this maximum value. At the same time, the resistance across the gold bridge is measured. Once this resistance is in the range of 15 to 20 kΩ, we let self-breaking of the junction occur in the presence of the solution containing the molecule at 0.1 mM concentration, i.e., no currents flow through the gap region at this stage. The built-up stress during the first part of the electromigration scheme allows for the opening of the gap assisted by the surface diffusion of gold atoms. Within an hour after self-breaking, the vacuum chamber is pumped to low pressure, and the insert with the devices is cooled down to Helium temperatures. Resistances in the range of MΩ to GΩ typically indicate the formation of an nm-sized gap with at least one molecule linking the two electrodes; empty junctions typically display a resistance of several GΩ or larger, leaving only noise to be observed in the spectra.

5.2. RESULTS

We measured five EMBJ samples with 75 different break-junctions following the procedure described in the previous section. Two chips were measured in the presence of the 2-OS di-radical (schematic of the molecule is displayed in figure 5.1.b; it is the same molecule as in the MCBJ experiments from the chapter 3), and the three others with the Sme-2OS, with a similar structure except for the addition of a benzene ring linked to the sulfur-anchoring groups in the para position of the fluorenyl unit (displayed in figure 5.1.c). The measurements are summarised in table 5.1. Out of the 75 junctions, 11 displayed signatures of a molecule captured in their electronic transport spectra. The fingerprints observed are similar to the ones observed for the 2-OS molecular junction formed in the MCBJ: a zero-bias peak (bottom plots from Fig. 5.2) or a dip with sharp steps and a flat bottom ascribed to a spin-flip inelastic spectroscopy signal (top plots from Fig. 5.2). Spin-flip signals are found in the presence of both the 2-OS and Sme-2OS indicating that the spin properties of the molecule are resilient upon integration of the sulfur-methyl termination groups to the fluorenyl units in the chemical structure of the open shell di-radical. This result indicates that some molecular conformations observed in EMBJ, and therefore the corresponding charge state of the molecule, are similar to the ones observed in MCBJ and STM.

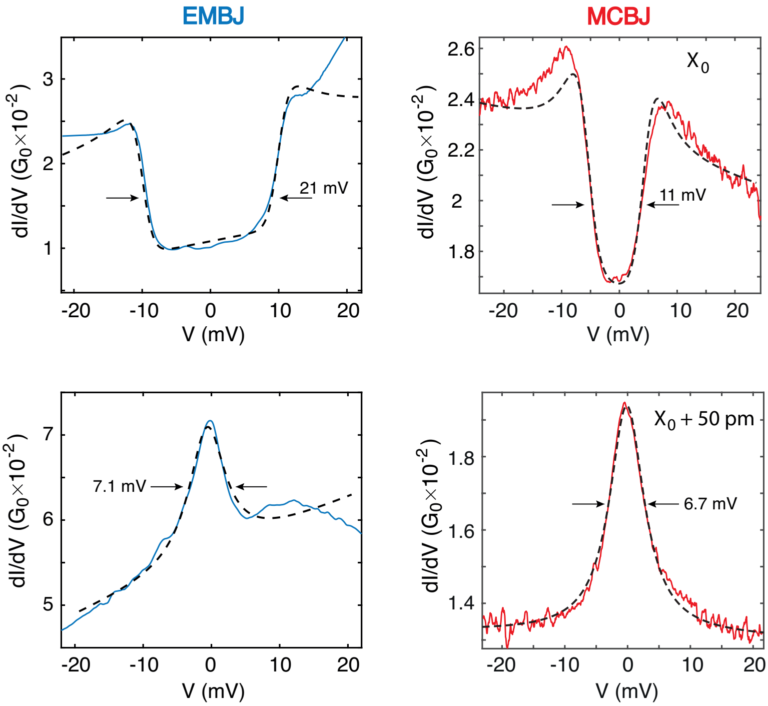

Figure 5.2: dI/dV spectra of 2-OS molecular junctions obtained (left) with EMBJ and (right) with the mechnically controlled break junction (MCBJ) technique at low temperature (≈ 6 K). In both devices (bottom figures) a zero-bias peak is observed with an energy scale compatible with spin-1/2 Kondo physics; the width of the peaks diplays a similar full-width half maximum of 7.1 mV for the EMBJ spectrum (bottom-left figure) and 6.7 mV for the MCBJ one (bottom-right figure) corresponding to respective Kondo temperatures of 40 K and 35 K. (top figures) Both devices also display a flat dip with sharp steps and bias overshoots at the steps position corresponding to inelastic spin-flip signals. The exchange coupling in both devices is of a similar order of magnitude of about 5 to 10 meV. Dashed lines in the top figure are fits to the model of Ternes [95] and fit to a lorentzian resonance on the bottom figures with full width half maximum (FWHM) displayed.

5.2.1. STABILITY DIAGRAMS DISPLAYING A SINGLE CHARGE STATE

Out of the eleven different junctions displaying molecular features, seven were found in a single charge state in the gate voltage range accessible without leakages, i.e. no charge degeneracy point (CDP) has been observed in their stability diagram. We will first focus on these devices with an emphasis on device A, C, and D from figure 5.3 that display similar cotunneling (COT) signals (see chapter 4) as observed in the previous MCBJ experiments.

In device A, the increasing dI/dV conductance on the right part of the map indicates that a charge degeneracy point is close, but increasing the gate voltage further than 2 V led to gate leakage in the device. The gate leakage threshold varies from device to device as it relies on the oxide quality at the interface between the gate and the electrodes. In this junction, a zero-bias peak is accompanied by two excitations around

-4 mV and +8 mV. These excitations in the dI/dV map can be better followed using the second derivative as displayed in figure 5.9. Note, that with increasing gate voltage, the zero-bias peak broadens in a similar way as seen for device E (it can be better seen in the second derivative displayed in appendix figure 5.9), while the two satellites excitations are slightly shifting toward positive bias. This behaviour is expected from a Kondo resonance due to the renormalisation of the exchange coupling interaction with the proximity of the CDP. The gate dependence of the Kondo resonances is discussed in more detail in the chapter 7. The temperature and magnetic-field dependent measurement shown in (chapter 7 kondo gate dependence device A) (bottom right) is in agreement with the expected behaviour for an S=1/2 Kondo resonance with a Kondo temperature of 20 K as shown in Fig. (chapter 7 kondo temp dependence device A).

Device B shows a variety of features in the same stability diagram: a flat dip in the center of the spectra tunable with gate voltage, a zero-bias peak on the right side of the map (for positive gate voltage) shifting to positive bias for lower gate voltage, and two excitations around 10 to 13 meV. A conductivity suppression is observed around a gate voltage of -4 V for a voltage bias above 7 mV, leading to negative differential conductance. It is a typical example of a complex situation requiring more detailed analysis to understand its origin. However, such an analysis is non-trivial and may not give insightful information on the system and, therefore, is not further investigated here. Similar resonance lines, however, may be found in other devices (for example, in device F from figure 5.4 two similar pair resonances can be seen around ±10 mV).

The spectra from device C with sharp steps around 10 mV are similar to the ferromagnetic inelastic spin-flip spectra observed in MCBJ (see figure 4.3 from chapter 3). A similar spectrum is also observed in other devices (see appendix) but did not show any magnetic field dependence as highlighted in MCBJ. The slight change of exchange coupling with gate voltage is better seen in figure 5.9; the dip width increases with about 1 mV/V with respect to the bias applied to the gate. As for the Kondo resonance from device A, this may be explained by the renormalisation of the exchange coupling arising when approaching the charge-degeneracy point, which is out of the reachable window in this case.

Device D displays a double peak centered around zero bias. Similar spectra have been observed in MCBJ. They are compatible with the two-stage Kondo effect, where Kondo correlations in combination with an antiferromagnetic exchange coupling with the same order of magnitude in energy leads to a zero-bias centered peak in the differential conductance with slight suppression of the conductance around zero-bias. The second derivative of the differential conductance map (displayed in appenix figure 5.9) shows that the energy position of this feature is independent of the gate voltage, which is different from the signal observed in Device C. EMBJ devices have a heater close to the sample position. We can use it to control the temperature of the device and gain more insights on the observed phenomena (see section 7).

5.2.2. REDUCTION AND OXIDATION CONTROLLED BY GATE VOLTAGE

We will now focus on the cases where a cotunneting signal was observed, and the charge degeneracy point could be crossed. When a cotunneling signal without a CDP is observed (such as devices A and C from Fig. 5.3), using the warm-up procedure up to 100 K

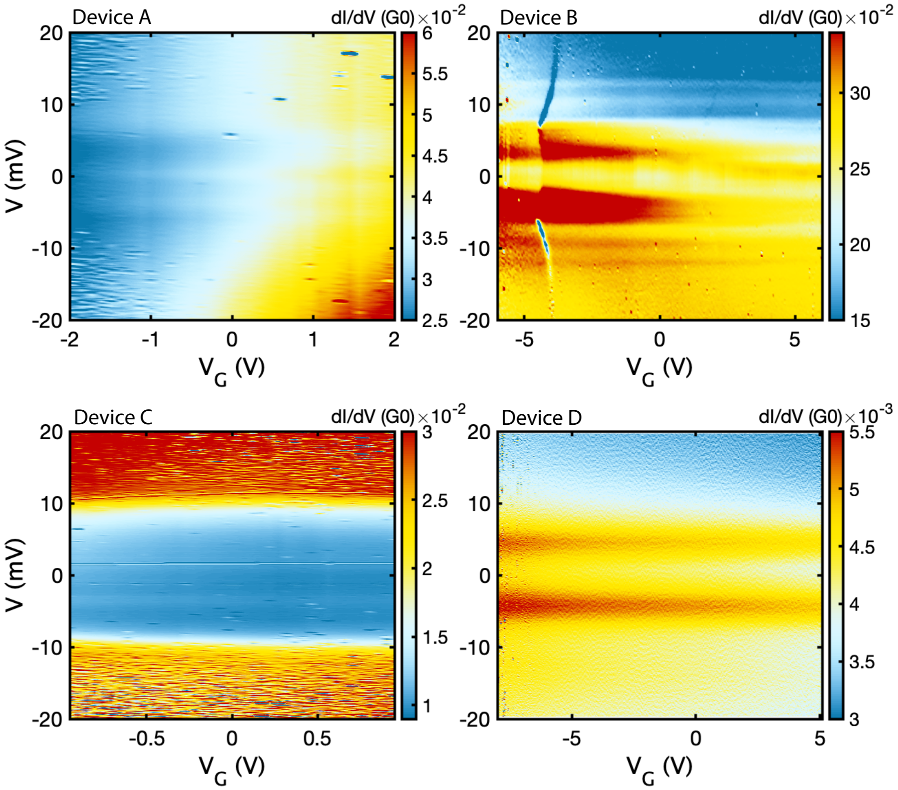

Figure 5.3: Differential conductance map ($\mathrm{d}I/\mathrm{d}V$ in units of $G_0 = \frac{2e^2}{h}$) as a function of source-drain bias voltage (V) and gate potential (V_G) for four different junctions in EMBJs displaying a single charge state. In Device A (top-left), the $\mathrm{d}I/\mathrm{d}V$ shows a zero bias resonance. Device B (top-right) is a more complicated example with a zero-bias resonance at positive gate voltage shifting to positive source-drain bias with a mirror excitation displaying negative differential conductance around a gate voltage of -4 V.. Device C (bottom-left) shows an example of an inelastic tunnelling signal with sharp steps at around ±10 mV. Device D (bottom-right) displays a double peak centred around zero bias.

and subsequently cooling down the device can increase the molecule diffusion in the junction leading to a new conformation and different capacitive coupling to the gate. It is the case for device E on the left of figure 5.4 that has been obtained by warming up the device E1 (see table 5.1) first showing an IETS signal with slight tuning of the exchange coupling with gate voltage (the change of exchange coupling may be an indication that a CDP is nearby being responsible for the renormalisation of the exchange coupling). Similar cotunneling fingerprints are observed in the stability diagram of device F with the 2-OS di-radical. On the other side of the CDP, we follow a Kondo resonance ascribed to the single magnetic impurity left on the molecule. Further analysis of the zero-bias peak behaviour while varying other parameters such as gate, magnetic field, and temperature are shown in chapter 7. In the present section, we will focus on the inelastic spin-flip signal on the right side of the Coulomb diamonds.

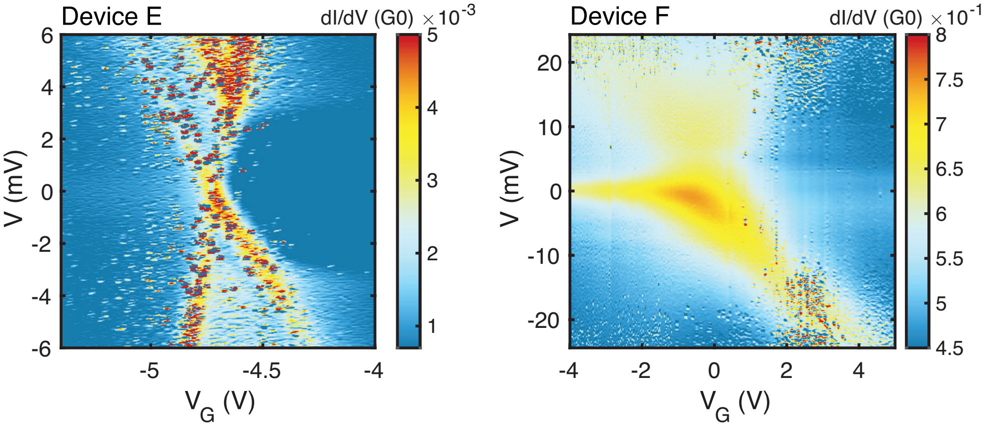

Figure 5.4: Stability diagrams with Δ N = 2 from two devices (right - device E with 2-OS / left device F with Sme-2OS). On the left of the Coulomb diamond, in the cotunneling regime, a zero-bias peak compatible with an S=1/2 Kondo resonance indicates the screening of a single magnetic impurity (see chapter 7). The right side shows an inelastic spin-flip signal with an exchange coupling of about 3 meV corresponding to a doubly occupied state on the molecule. The bottom-left edge of the Coulomb diamond is missing in the stability diagram from device F. This feature has been observed in other devices. These two devices are good examples of similar phenomena observed in the COT regime with different coupling parameters: the gate coupling extracted from Device E is 0.9 % while Device F is 0.5 %. The conductance range is two orders of magnitude larger for Device F, where no SET excitation are observed in a broader bias range than for Device E, where both COT and SET excitation can be seen.

5.2.3. GROUND STATE DETERMINATION AND MAGNETIC FIELD DEPENDENCE OF THE INELASTIC SPIN-FLIP SIGNAL

In the previous experiments with MCBJ, co-tunneling signals ascribed to inelastic spin-flip scattering signals were also observed. For the device measured in the presence of an external magnetic field, the ground state was found to be ferromagnetic (see figure 4.3). Some features in the $\mathrm{d}I/\mathrm{d}V$ spectra can be used to determine the system's ground state. A small zero-bias conductance enhancement at the bottom of a flat dip (as in the MCBJ examples from Fig. 4.3) indicates a ferromagnetic/triplet ground state. This zero-bias enhancement origin is linked to the Kondo correlations arising from the hybridisation of localised magnetic impurities with the electron bath of the gold electrodes. The hybridisation strength can be modelled by an exchange coupling parameter, J, between the localised magnetic impurity (electron in the molecule's semi-occupied orbitals) and the electrode's electron bath. An enhancement of the conductance at zero bias is found (in the ferromagnetic ground state case) with an increased value of $G(0\ V)$.

The Kondo hybridisation strength is also influencing the bias overshoot prominence of the steps at the edges of the dip. For a singlet ground state, the step at finite bias corresponds to an electronic transition to the first excited triplet state that is three times degenerate (see the energy spectrum depicted in figure 5.5 c). The triplet levels allow for transitions between them, enhancing the conductance at these points, resulting in larger bias overshoots for an antiferromagnetic/singlet ground state than for the ferromagnetic/triplet ground state. These features have also been observed in the MCBJ experiments: an example of potential antiferromagnetic ground state is shown in the top-right figure 5.2 where significant bias overshoot without conductance enhancement at zero-bias is shown. The case on the top-left of figure 5.2 shows a more ambiguous example where slight bias overshoots are visible but small enough to be compatible with a ferromagnetic ground state where the Kondo correlations are too small to be observed at the bottom of the dip. For the IETS signals observed in a stability diagram with a charge degeneracy point (see figure 5.4), the bottom of the dip is flat, while bias overshoots are also present, indicating an antiferromagnetic/singlet ground state.

We confirm this interpretation of the $\mathrm{d}I/\mathrm{d}V$ spectra features by ramping an external magnetic field up to 9 T aligned with the z-axis of the device while recording its transport characteristics. We see a different step opening from the one observed in the MCBJ (see figure 4.3). In this case, there is no opening at zero bias, while the steps positioned at finite bias corresponding to the exchange coupling energy are blurred. In the picture where the exchange coupling is antiferromagnetic, this level is the degenerate triplet state split by the magnetic field. Instead of two new intermediate conductance plateaus appearing, as expected close to a 0 K temperature, we observe a widened dip at the top of the steps and a shrinkage at the bottom, appearing as an increased slope in this region. This effect is due to thermal broadening that is expected to be of $3.5 \times k_B T$ (in this case, the temperature was 1.7 K corresponding to $k_B T = 0.15$ meV and $3.5 k_B T = 0.5$ meV)

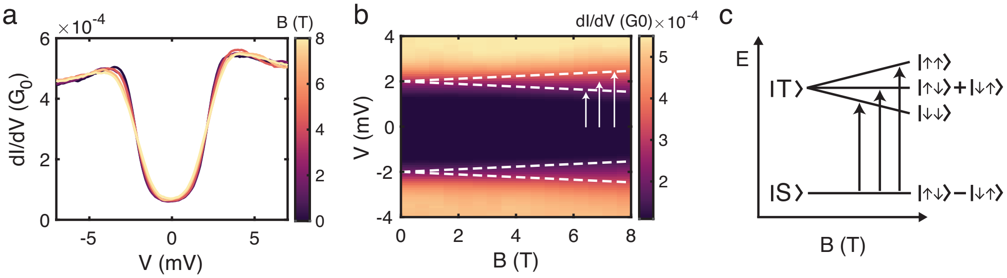

Figure 5.5: (a) $\mathrm{d}I/\mathrm{d}V$ of the spin-flip signal of device E at $V_G = -4.05$ V in the cotunneling regime at different applied external magnetic field (solid lines), dashed lines correspond to the best fit with the Ternes model using an exchange coupling of $J_{ex} = 3$ mV and Kondo coupling strength $J\rho_s = 0.1$. (b) $\mathrm{d}I/\mathrm{d}V$ as a function of applied bias V and magnetic field B. The splitting expected with a magnitude of $g\mu_B B \approx 120$ μV/T is depicted by the dashed white lines. The singlet ground state transitions allowed by selection rules from the scheme (c) are depicted by the white arrows.

5.3. INTERPRETATION AND DISCUSSION

No signs of a ferromagnetic ground state have been observed in the five EMBJ samples measured. Both Sme-2OS and 2OS showed indications of a singlet ground state with the reduction of the molecule by tuning the electrostatic environment with the gate electrode. To push the SET resonance in the chemical potential range of the electrodes, the molecule must have a sufficient capacitive coupling to the gate; a molecular junction conformation compatible with this requirement is the adsorption of the radical on top of the aluminium oxide covering the gate electrode, at the bottom of the gap formed between the two gold electrodes. In this case, the strong van der Waals interactions tend to planarize the molecule on the surface, reducing the conformational degrees of freedom and favouring an antiferromagnetic exchange coupling between the two radical centers. The STM experiments complement this interpretation (PUT A SENTENCE HERE - see chapter 4).

The proximity of the CDP is renormalising the energy separation between the ground and excited of the molecule, tuning the strength of the magnetic exchange coupling interaction. Beyond that resonant point to the more negative voltage side, the molecule's total charge number is reduced, leaving a single electronic spin 1/2 characterised by a Kondo resonance in the $\mathrm{d}I/\mathrm{d}V$ spectra around zero-bias voltage. The correlations of the Kondo coupling can also be tuned by the gate electrode and are discussed in further detail in chapter 7. Contacting the molecule in specific ways can also lead to a reduction of the total charge, making the di-radical a single radical, in which case a S=1/2 Kondo resonance is observed in some EMBJ spectra (see figure 5.3) which are very similar to MCBJ observations [76]. In this scenario, the image charges at the interface with the electrodes play a preponderant role in the electrostatic environment experienced by the molecule.

The exact mechanism behind this redox reaction is not explicitly defined. The wavefunctions of the partially filled orbitals within the molecule may be significantly influenced by the surrounding electrostatic environment, leading them to fully localise within the fluorenyl units. This localisation suppresses any interactions or overlap between these orbitals, resulting in two non-interacting S=1/2 systems, as indicated by the presence of Kondo resonances. A geometric configuration with an oxygen atom close to the molecule may induce a shift of the energy levels in the order of magnitude of an electronvolt. Based on calculations in the gas phase, the reduced radical, which contains one or more hydroxyl groups, tends to adopt a less planar conformation. In such cases, we anticipate changes in the molecular conformation and tunnel couplings if an oxygen group interacts with the di-radical to induce reduction.

Based on the measurements presented in this chapter, we observed that the tunnel and capacitive couplings remain relatively unchanged when crossing the charge degeneracy point (CDP). However, it's essential to note that even a slight alteration in the shape or thickness of the barriers would result in significant differences in the recorded electronic spectra.Estimating the strongest tunnel coupling using Kondo correlations between the localised magnetic impurity and the screening electrons from the gold electrodes, we see that the parameter $J\rho_s$ is in the same order of magnitude for both inelastic spin-flip and Kondo resonance sides of the Coulomb diamond.

5.4. CONCLUSION

The magnetic fingerprints of the all-organic 2-OS di-radical, and its sulfur-stabilized version the Sme-2Os, are preserved in three-terminal devices at low temperatures. The molecule charge state is reversibly reduced or oxidised involving a change from a $S = \frac{1}{2}$ to $S = 1$ state by tuning the electrostatic environment with gate voltage. Measuring spin-flip inelastic spectra as a function of an externally applied magnetic field, an antiferromagnetic exchange coupling is found when the molecule is in its even charge state. These results complement the observations from previous studies with the MCBJ and STM techniques. Based on the similarities between the different methods, we expect the EMBJ's molecular junctions geometries to be more or less planar like the ones in the STM setup with an adsorbed molecule constrained on the gate or/and on one of the electrode surfaces with indications for a singlet ground state. These results indicate that the exchange coupling of the 2-OS and Sme-2OS di-radicals can vary from triplet to singlet ground state as already indicated from the MCBJ measurements. The value of the magnetic exchange coupling depends on the angle between the anthracene and fluorenyl units; physisorption of the molecule on a surface is likely to restrain this exchange coupling to small antiferromagnetism or two non interacting spins $\frac{1}{2}$.

Chip	Molecule	junc.	mol.	Sample	ΔN	Fingerprint
1	2-OS	17	3	A1	1	Kondo (T_{K} ~10 K)
				A	1	Kondo (T_{K} ~8 K)
				F	2	Kondo-IETS (T_{K} ~16 K / J_{ex} ~3 meV)
2	2-OS	17	2	I	2	SET resonances (C_{gate} ~2.7 % / no COT)
				H	2	Spin-blockade
3	Sme-2OS	16	2	D	1	Double peak - Two-stage Kondo (T_{K1} ~60 K / T_{K2} ~20 K)
				B	1	Unusual resonance
4	Sme-2OS	21	2	G	2	SET resonances (C_{gate} ~1.9 % / no COT)
				C	1	IETS (J_{ex} ~8 meV)
5	Sme-2OS	4	2	E1	1	IETS (J_{ex} ~2 meV)
				E	2	IETS-Kondo (J_{ex} ~3 mV / T_{K} ~10 K)
				E2	2	IETS-Kondo (with Spin-blockade)
				J	1	Kondo (T_{K} ~10 K)

Table 5.1: Summary table of devices measured and their corresponding molecular features in the EMBJ molecular junctions experiments formed in the presence of the 2-OS and Sme-2OS di-radicals. The third column correspond to the number of working junction before electromigration and the fourth column to the number of junction displaying molecular features. Each junction has a label (ordered as they appear in the chapter). When a number is in the label, this junction has been obtained after a change of conductance from the smaller label number (i.e., junction A2 has been obtained after a change of junction A).

5.5. APPENDIX

5.5.1. ELECTROMIGRATION PROCEDURE

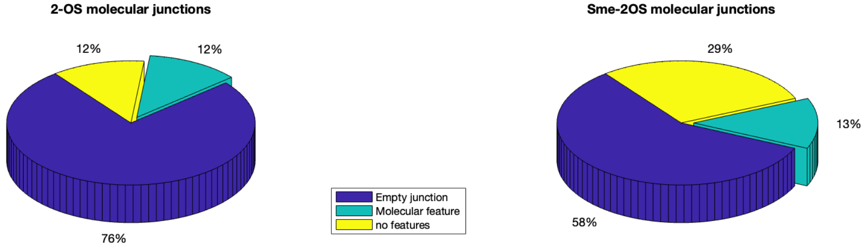

Figure 5.6: Statistics of 2-OS and Sme-2OS di-radical molecular junctions formation in electromigration break junction (EMBJ) devices .

The electromigration procedure consists of ramping the voltage between a minimum voltage value to readout the resistance of the junction and a maximum threshold value gradually increased by the operator. When a change in the resistance of more than 10 % is observed, this maximum threshold is slightly reduced to avoid too abrupt opening which can lead to large gap such as some displayed in figure 5.7.

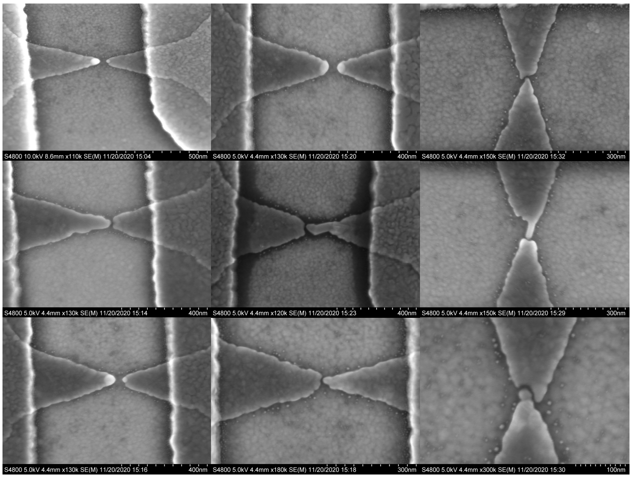

Figure 5.7: SEM pictures of gold bowties after the electromigration procedure without a molecule. The gap size and shape can vary greatly from device to device

The optimal devices typically display a slow drop of conductance depicting a parabola on the current/bias migration diagram sin figure 5.8

5.5.2. DATA PROCESSING

The current-voltage characteristics are acquired with a home-built DAC system to apply a DC bias voltage and amplify the output current in a readout voltage saved with a Keithley DMM. The dI/dV curves are obtained by deriving the current using a Savitzky-Golay

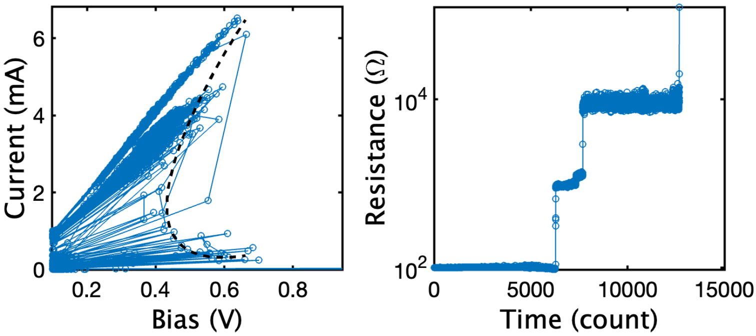

Figure 5.8: (Right) Resistance as a function of time and (left) current-bias diagram of the electromigration procedure on a pristine EMBJ device. The threshold current is gradually increased by the operator until the resistance changes by more than a few percent. These increases of resistance happen fast as depicted by the jumps in the top figure.

filtering method. The second derivative of some devices can be used to better see shifts of the features such as displayed in figure 5.9.

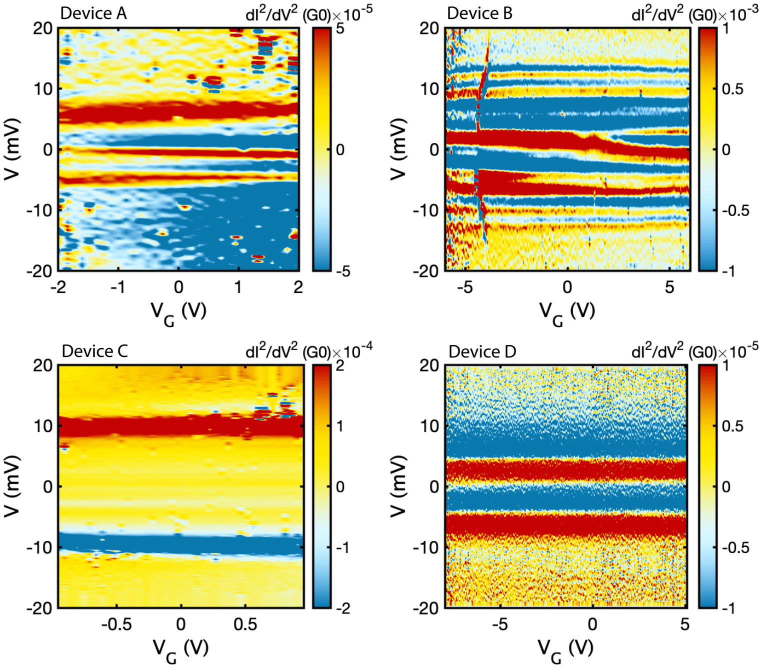

Figure 5.9: d^2I/dV^2 of the devices with no crossing of the charge degeneracy point in the stability diagram. In device A, the zero-bias peak intensity is increasing at positive gate voltages, the two excitation at −5 and +6 mV are shifting toward positive bias in the meantime. The exchange coupling in device C is slightly increasing (about 0.5 mV/V) with gate voltage. The features in device D do not show any dependence on the gate voltage.

5.5.3. ADDITIONAL DATA ON SPIN-FLIP SPECTRA

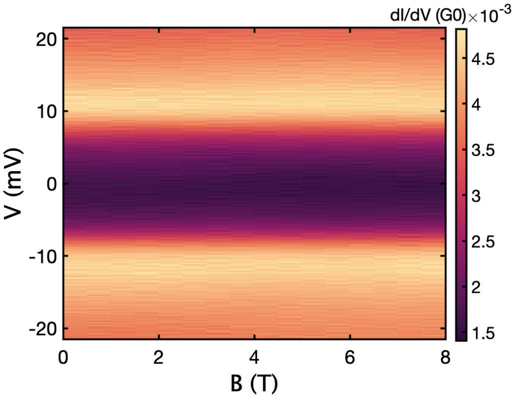

Figure 5.10: dI/dV of a spin-flip signal in a Sme-2OS molecular junction (device C see table 5.1) in function of applied external magnetic field along the normal of the device plane

TEMPERATURE BROADENING

The spin-flip signal from device C was measured in a system without a 1 K pot in very close conditions to the mechanically controlled break junctions (MCBJ) devices at an estimated temperature of 6 K. This device was measured with an external magnetic field along the z-axis of the device, yielding the stability diagram displayed in figure 5.10. This measurement do not show any feature shifting with respect to the applied magnetic field.

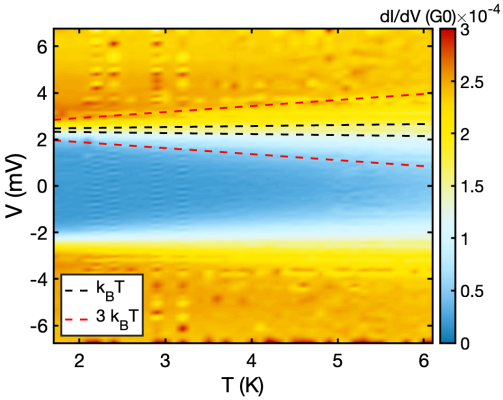

Figure 5.11: dI/dV in function of temperature of a spin-flip signal in a Sme-2OS molecular junction from device C. Dashed lines indicates the energy scale for thermal broadening of respectively $k_B T$ (black) and $3k_B T$ (red). No clear change of the spectra is observed up to magnetic field of 8T.

Measuring the temperature dependence of the inelastic spin-flip signal of device E displayed in figure 5.11, we see that the step broadening with respect to the temperature scale better with the red dotted lines (corresponding to a splitting of $3k_b T$) than with the black dotted lines (corresponding to a splitting of $k_b T$). We speculate that the observed signal was a singlet ground state where the splitting of the step at 8 T $g\mu_b B \approx 1$ meV while $3k_b T \approx 1.6$ meV.

BACKGROUND ASYMMETRY

Both for the 2-OS and Sme-2OS radicals we observed a change of background asymmetry in the differential conductance spectra between two distinct Coulomb diamond regions. In both devices E and F, we observe a position background slope in the even charge state and a negative slope in the odd charge state.

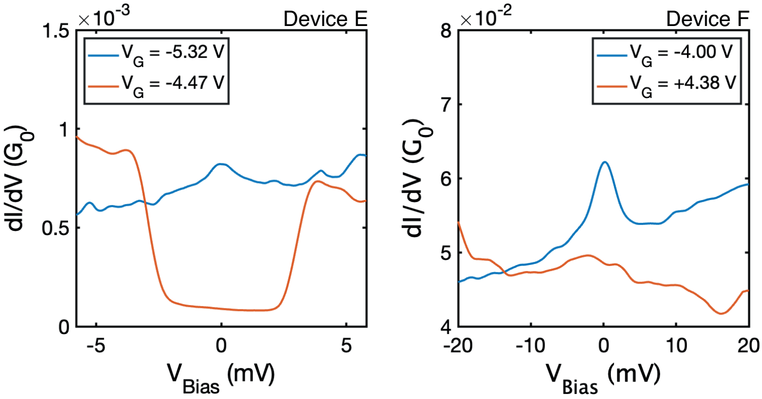

Figure 5.12: dI/dV linecuts in the (red) even and (blue) odd charge states from figure 5.4.

6

GROUND-STATE INVESTIGATION WITH ELECTRICAL GATING IN ALL-ORGANIC DI-RADICAL MOLECULAR BREAK JUNCTIONS

> *. . . j'me sens comme un imprimeur :*
> *j'fais qu'penser au papier.*
>
> Issa Lorenzo Diakhaté - Ancelotti

This chapter focuses on all-organic di-radical molecular junctions displaying features in the resonant transport regime. Some devices show these in both the off-resonant co-tunneling (COT) and resonant sequential electron tunneling (SET) regimes. Other devices display differences of several orders of magnitude between the noise in the COT and the SET regime; in this case, determination of the ground state with inelastic spin-flip signatures - as described in the previous chapters- is not possible. By following the chemical potential shift of the charge neutrality point with respect to the temperature, we extract the evolution of the spin-entropy of the molecule as an indication of its ground state.

6.1. INTRODUCTION

In three-terminal devices, the electrostatic environment and the alignment of the molecular orbitals' energy with the electrodes' chemical potential can be varied by applying a potential to the third gate electrode [119]. Pushing a molecular orbital through the chemical potential difference across the junction increases the conductance where the molecule switches between two different charge states, as discussed in chapter 1. This effect is typically detected in molecular devices by observation of an increased conductance around specific values of the gate voltage. The ability to manipulate molecular junctions through gate voltage opens possibilities for the development of memory storage [125] and molecular wires for nanoscale circuits [126] with the potential to evolve computing and data storage by providing compact, low-power alternatives to traditional semiconductor technologies [24].

Focusing on the spin properties of these devices, the gate voltage has been used to induce redox reactions of the radical or modify the spin-coupling properties [82, 88, 92] observed in the cotunneling (COT) regime as discussed in the previous chapter. Helpful information can also be extracted from the resonant transport regime in devices with non-trivial conductance properties where characteristics such as spin-phonon coupling [127, 128] can be investigated. Extracted quantities, such as the spin-entropy evolution with temperature, can yield insights on the ground state of the system and/or the precise location of the unpaired magnetic moments [129, 130].

In this chapter, we discuss 2-OS and Sme-2OS molecular junctions in a three-terminal geometry with a stability diagram displaying a charge degeneracy point (see table 5.1) and focus on the features in the sequential electron tunnelling (SET) regime. We will first focus on the SET resonances appearing as thin excitation lines parallel to the edge of the Coulomb diamond for devices I & J in figure 6.1. We measure the evolution of these excitations and the charge degeneracy point (CDP) as a function of applied external magnetic field. The shift of the latter points at a saturation phenomenon that may be linked with spin-anisotropy. Finally, we discuss stability diagrams with indications for spin-blockade (see device G & H in figure 6.1).

6.2. RESULTS

We used the 2-OS di-radical (synthesis is described in [76]) and Sme-2OS di-radical holding a similar backbone with the addition of a benzene and sulfur-methyl chemical groups participating to a steadier anchoring of the molecule with metallic electrodes. Both di-radicals are shown in insets b and c in figure 5.1. We fabricated 2-OS and Sme-2OS molecular junctions with the electromigration break junction (EMBJ) technique at low temperature (~2 K), which is described in chapter 5. The current-voltage characteristics of the molecular junctions are obtained by sweeping a bias voltage between the source and the drain electrodes and recording the output current. This measurement is repeated for different values of the gate-electrode potential, and results are summarized in a differential conductance ($\mathrm{d}I/\mathrm{d}V$) map as a function of source-drain and gate electrode bias called a stability diagram (figure 6.1). The signals observed in the 75 junctions

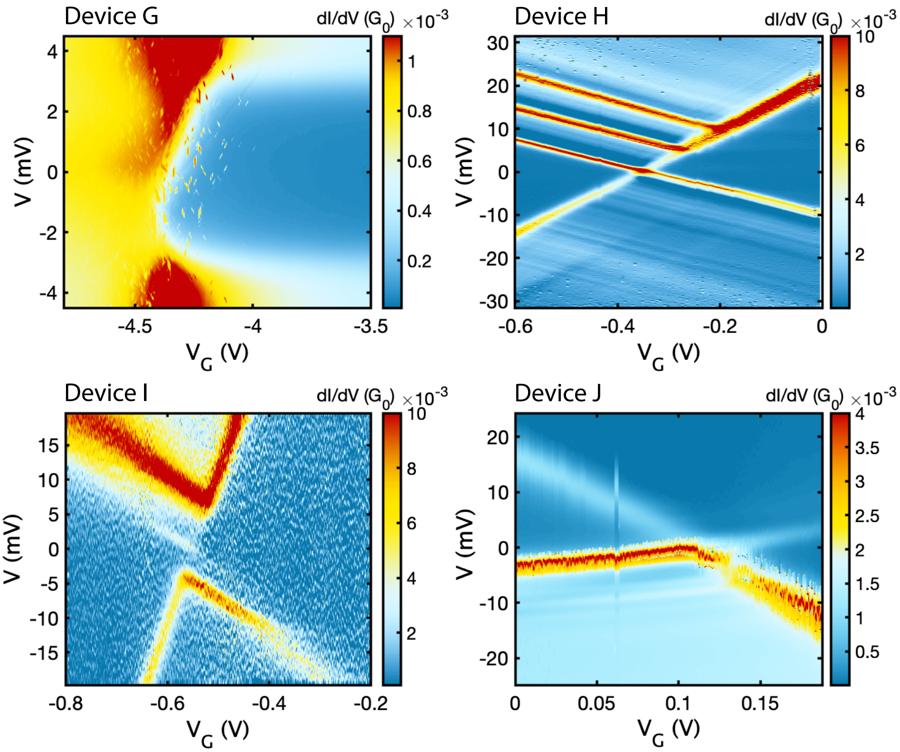

Figure 6.1: Stability diagrams displaying two charge states. Device G (top left panel) shows a Kondo resonance on the left part of the diamond while an inelastic excitation of about 3 mV is observed on the right side. Device H and J (panels on the right) do not shows co-tunneling excitations (on the left and right hand side of the diamond) but multiple excitation lines in the sequential electron tunneling (SET) regime. Device I is another example of a charging device that exhibits a clear excitation in the SET regime, which in this case has a larger conductance than the edges of the Coulomb Diamond.

measured are summarized in table 5.1. Once at low temperature, six junctions display a sufficient gate coupling to switch the molecule between two different charge states, displaying a characteristic pattern in their stability diagram involving Coulomb diamonds, typically observed in quantum dots and single-electron transistors. Two of these devices have been discussed in chapter 5. This chapter focuses on other devices where the charge degeneracy point could be crossed.

When a molecular orbital is energetically aligned between the chemical potential of the two electrodes, a new transport channel opens for conduction electrons via an excited state of the molecule (see chapter 1) and resistance of the junction decreases. This regime where first-order processes are the main components of the transport is referred to as sequential electron tunnelling (SET), where an electron tunnels between the two electrodes by jumping on the available molecular level and tunnels to the other electrodes in a subsequent process. The SET regime scales linearly with tunnel coupling to the leads (Γ), in contrast to the co-tunelling (COT) regime, including higher order processes where charging of the molecule is virtual and the current scales quadratically with the coupling (Γ^2). When Γ, the total tunnel coupling is in the proper range, both COT and SET regime diplay sharp resonances containing information on the spin state (i.e., device E from figure 5.4). At larger values of Γ, the SET regime saturates (for example, device G from figure 6.1), yielding broad resonances in overall higher conductance regions. Finally, at small values of Γ, a sharp conductance resonance separates the SET and the COT regimes (see devices H, I and J from figure 6.1), but the cotunneling regime displays a weak, noisy signal restraining deeper analysis.

The diamond structure is linked to the capacitive couplings between the molecule, the electrodes and the gate [119] by the relation $\frac{C}{C_G} = \frac{1}{\alpha} = \frac{1}{\beta} + \frac{1}{\gamma}$ where β and γ are the slopes of the two lines in the stability diagrams separating SET and COT regimes. This gate coupling parameter takes typical value in 1-2 % range: device G (0.9 %) or device H (1.9 %), but larger values are observed in device I (4.5 %) and J (2.8 %) typically accompanied with a larger tunnel coupling asymmetry between the source and the drain. We note that, at most, only one diamond is visible in the gate bias range accessible. This is expected in molecular junctions where the addition energy is in the range of hundreds of meV or larger. The diamond's corners of devices H and J close at zero source-drain bias, forming a clear charge degeneracy point (CDP); this feature is less clear for devices G and I. In device I, the highest conductance resonance is at finite bias in the SET regime; at a first glance, the signal is similar to a non-closing diamond, but looking in more detail, a faint white diamond closing at zero bias can be observed. In devices H and J, many excitations are visible in the SET regime, more than ten for Device H in both the upper and lower part of the Coulomb Diamond. Also, dark lines parallel to the opposite diamond edge suppressing the conductance in the lower source-drain bias region can be seen.

To further study the SET excitations in sample H, we fixed the gate voltage close to the charge degeneracy point (-350 mV) and measured dI/dV spectra when applying an external magnetic field perpendicular to the sample up to 9 T (figure 6.2). Note, that the charge degeneracy point is slightly shifted compared to the original stability diagram. Some excitation shifts toward positive bias with a magnetic field, while others shift to a more negative bias voltage. The ground state evolution with magnetic field (solid red line close to 0 V in figure 6.2 a and b) is consistent with a Zeeman effect $g\mu_{textrmB}B$; we expect it to shift by 0.12 meV/T (taking g=2), drawn as dashed black lines. Two of these excitations, around -8 meV, are "fusing" together above 2.5 T and seem to shift toward positive bias with increasing magnetic field (see figure 6.2 c). This non-continuous shift does not fit with the magnetic field evolution expected from Zeeman splitting of a free electron.

Without the possibility of using the COT signal to determine the ground state of the molecular junctions, we can use the shift in gate potential of the degeneracy point when applying a magnetic field and changing the temperature to get further insights. We determine this shift by recording the zero-bias conductance as a function of gate voltage called a gate trace and find the maximum of the current for device H (Fig. 6.3) and device J (Fig. 6.4). The latter shows a linear chemical potential shift with the magnetic field and temperature, while the first shows a nonlinear one. The difference in degeneracy, d_N and d_{N-1}, from the states with N and $N-1$ electrons is expected to shift the charge degeneracy point toward the lowest magnetic quantum number state, m_s, with increasing

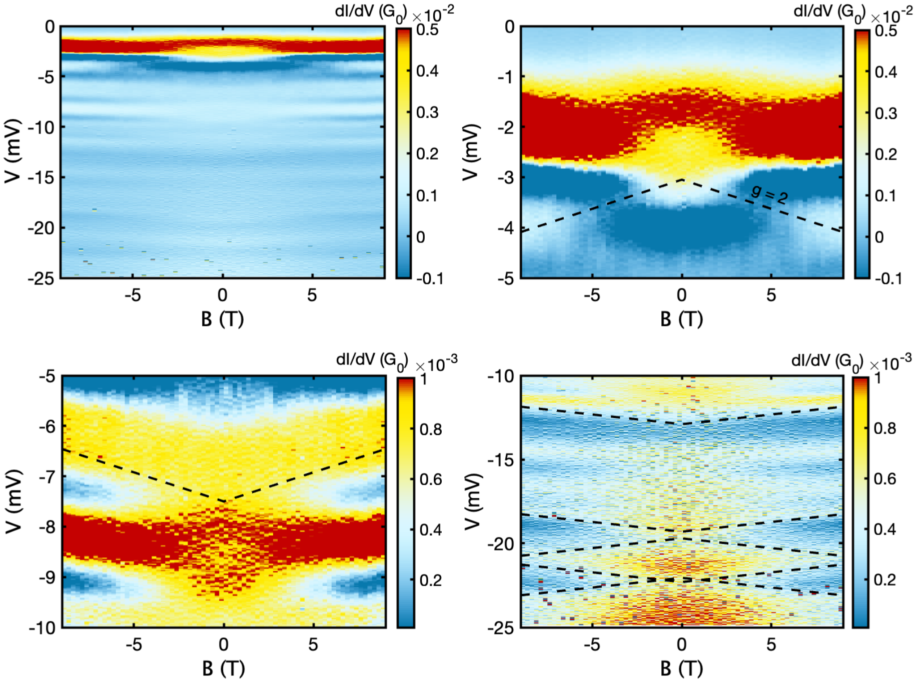

Figure 6.2: Magnetic field dependence of the excitations in the SET regions for device H taken at a fixed gate voltage of -350 mV (upper left panel). The other panels shows the same data but in different voltage range with adjusted color scale highlight the splitting occurring for the resonance at the edge of the SET regime. The observed splitting is consistent with a Zeeman splitting energy scale with an electron spin g-factor of 2 (dashed black lines).

temperature [130]:

$$\frac{\partial \mu}{\partial T} = \frac{1}{2} \Delta S_{N-1 \to N}. \tag{6.1}$$

This equation relates the CDP shift as a function of T with a change in spin entropy $\Delta S = S_{N-1 \to N} - S_N = k_{textrmB} \left[\ln(d_\mathrm{N}) - \ln(d_\mathrm{N-1}) \right]$ between the two ground states of the molecule. The shift of the conductance maximum observed in the stability diagram is connected to the capacitive couplings to the leads and to the gate: $\Delta V_{G_\mathrm{peak}}(T) = \Delta \mu_\mathrm{mol}(T)/\alpha$. In a di-radical with a transition between a doublet to a singlet ground state, the change of degeneracy between the two states is expected to go from $d_{N-1} = 2$ to $d_N = 1$ yielding a shift with a slope of $\frac{1}{2} k_\mathrm{B} \ln(2)$. Quantitatively, the magnitude of the shift is in the range expected for a singlet-to-doublet transition in device H as displayed by the dashed black line in figure 6.3 c. Nevertheless, a change in the shift direction is observed above a temperature of 5 K. Interestingly, this change of direction happens at an energy of $k_\mathrm{B} T(T = 5.5\ K) \approx 0.47$ meV, which is close to the energy at which a saturation happens in the magnetic field dependence of the SET resonances

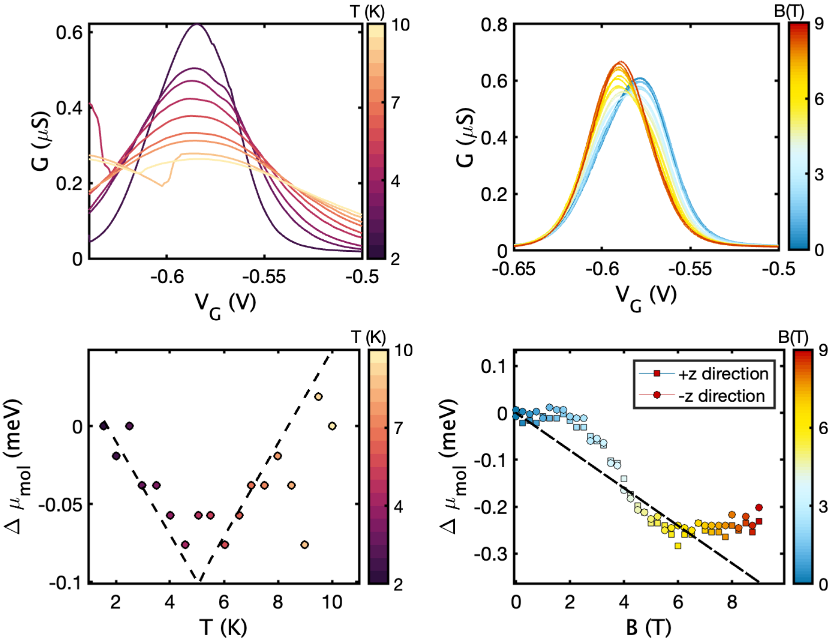

Figure 6.3: Conductance vs. gate voltage across the charge neutrality point of device H as a function of temperature (left panels) and magnetic field (right panels). The gate bias value at which the maximum of the current in the gate sweep is observed is plotted on the bottom pannels for both cases. The maximum value of the current as a function of the gate voltage V_G is converted to a chemical potential shift $\Delta\mu_{\mathrm{mol}}$ using the gate coupling parameter extracted from the Coulomb diamonds α. (Bottom left) No monotonous shift of the CDP with respect to the temperature is observed but the magnitude of the shift is in the range of $\frac{1}{2}k_B T\ln(2)$ (black dotted line). (Bottom right) Non-linear shift of the chemical potential with respect to the magnetic field; no hysteresis is observed between positive and negative direction of the magnetic field. Both magnetic field and temperature dependence of the CDP are non-linear with changes observed in the same range of energy.

$(k_B T(T = 1.8\ K) + g\mu_B B(B = 2.5\ T) \approx 0.45$ meV) in figure 6.3 d (i.e. the CPD does not shift further with stronger magnetic field). In contrast, device J from figure 6.4 c displays a linear shift of the chemical potential, but in this case, the magnitude is different, suggesting a change in spin-entropy with a different origin than a singlet-to-doublet transition.

We measure this shift with respect to an applied external magnetic field (see b and d in figures 6.3 and 6.4). In this case, similar to the case with varying temperature, the shift is not linear with respect to the magnetic field. At low fields, no clear shift is observed up to 2 T. The peak is then rapidly shifting to more negative values of the gate voltage until reaching a threshold above 6 T, where the peak does not move with increasing magnetic field. Again, the magnitude of this shift is in reasonable agreement compared to the black dashed line, but a deviation from this trend is observed. On the other hand, the same measurement on device E (figure 6.5) shows good agreement between experimental data and the expected trend, although a slight difference in the two directions (+z for circular

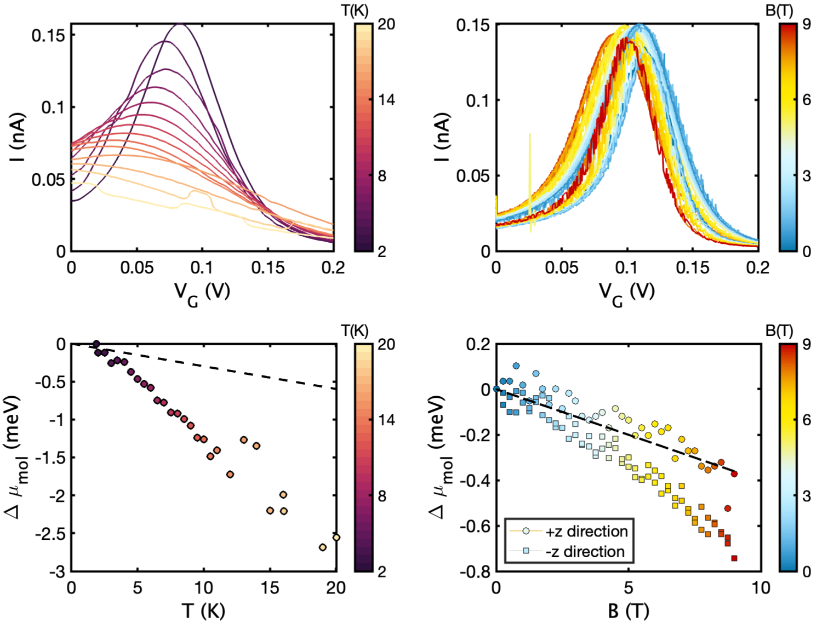

Figure 6.4: Current vs. gate voltage across the charge neutrality point of Device J as a function of temperature (left panels) and magnetic field (right panels) in a similar way as for Device H in figure 6.3. (Bottom left) A shift of the CDP with respect to the temperature is observed but the magnitude of the shift is larger than the expected $\frac{1}{2}k_B T \ln(2)$ (black dotted line). (Bottom right) Device J shows a linear shift of the chemical potential with respect to the magnetic field with a magnitude close to $\frac{1}{2}g\mu_B B \ln(2)$ (black dotted line). A slight hysteresis is observed between positive (squared markers) and negative direction (round markers) of the magnetic field. Both magnetic field and temperature dependence of the CDP are linear, unlike Device H.

dot, -z for squared ones) is observed in this case while device H show identical results for both. Note, that in both devices shifts of their charge degeneracy point occur toward the same direction (negative gate value) when a magnetic field is applied in both directions.

We have reiterated the measurement on device G (from figure 6.1 obtained from device E 5.4). The result for both positive (a, c and e) and negative (b, d and f) magnetic field directions are compiled in figure 6.5 where the conductance resonance as a function of the gate bias is displayed in a and b, the shift of the resonance center is shown in c and d, and the change in height is visible on e and f. In c and d, the shift of the CDP as a function of the magnetic field is displayed with a black dashed line reporting values from equation 6.1 with a change in spin entropy corresponding to a singlet-to-doublet transition, showing that the shift is in the range expected from Zeeman splitting. Finally, the height of the peak varies linearly with increasing magnetic field. This is consistent as the height of the peak is expected to scale with 1/T [119]; the slope is shown in the inset of the figures.

6.3. SPIN-BLOCKADE PHENOMENA

Device G from figure 6.1 displays a Coulomb diamond with three distinct levels of conductance. On the right of the CDP, the lowest conductance zone is at the bottom of a spin-flip signal with $J_{ex} \approx 3$ mV, while on the left of the diamond, a Kondo resonance indicates that the radical is in its reduced spin 1/2 state. This behaviour has been described in the previous chapter as this device has been obtained after heating of Device E (figure 5.4). Thus in Device G, the excitation in the SET regime isn't distinguishable and a uniform zone of high conductance is visible, except for the bottom part of the Coulomb diamond where the right corner is missing, leaving a diamond structure non centered on zero-bias. An asymmetric Coulomb diamond not closing at $V = 0$ mV is the typical signature expected from a spin-blockade phenomena. To further study the effect, we applied a magnetic field of 9 T to the device expecting the transition to become available again with application of an external magnetic field, however, no clear change of the blockaded region of the Coulomb diamond has been observed up to the maximum magnetic field available. This indicates that the energy of spin-excitations is too large for the magnetic field to lift this blockade.

Device I from figure 6.1 shows an excitation in the SET regime with an order of magnitude larger conductance than the resonance at its charge degeneracy point (CDP). The two solid red diamond corners above +5 mV and under -2 mV depict a case where SET transport is blocked up to a finite bias. This effect is expected from a *spin-blockade* where the difference between the two ground state multiplets, $\Delta S > \frac{1}{2}$ for which selection rules forbid the transitions close to zero-bias. In this device, the cotunneling (COT) regime is not visible

6.4. CONCLUSION

In this chapter, we investigated all-organic di-radical molecular junctions exploiting features in the sequential electron tunneling (SET) regime. We show that the resonance in the SET regime is potentially linked to the ground state of the molecule and investigated this relation by measuring shift of the charge degeneracy point (CDP) as a function of the temperature and external magnetic-field applied. The non-linear temperature and magnetic dependence observed in device H suggest presence of magnetic anisotropy in the molecular junction. We highlight the chemical potential shift method as an additional method for ground state determination of a molecular junction applicable even when the co-tunneling regime is not accessible. At the same time, the variations from device to device with the different behaviours observed highlight the different junction geometries available in the electromigrated break junctions devices.

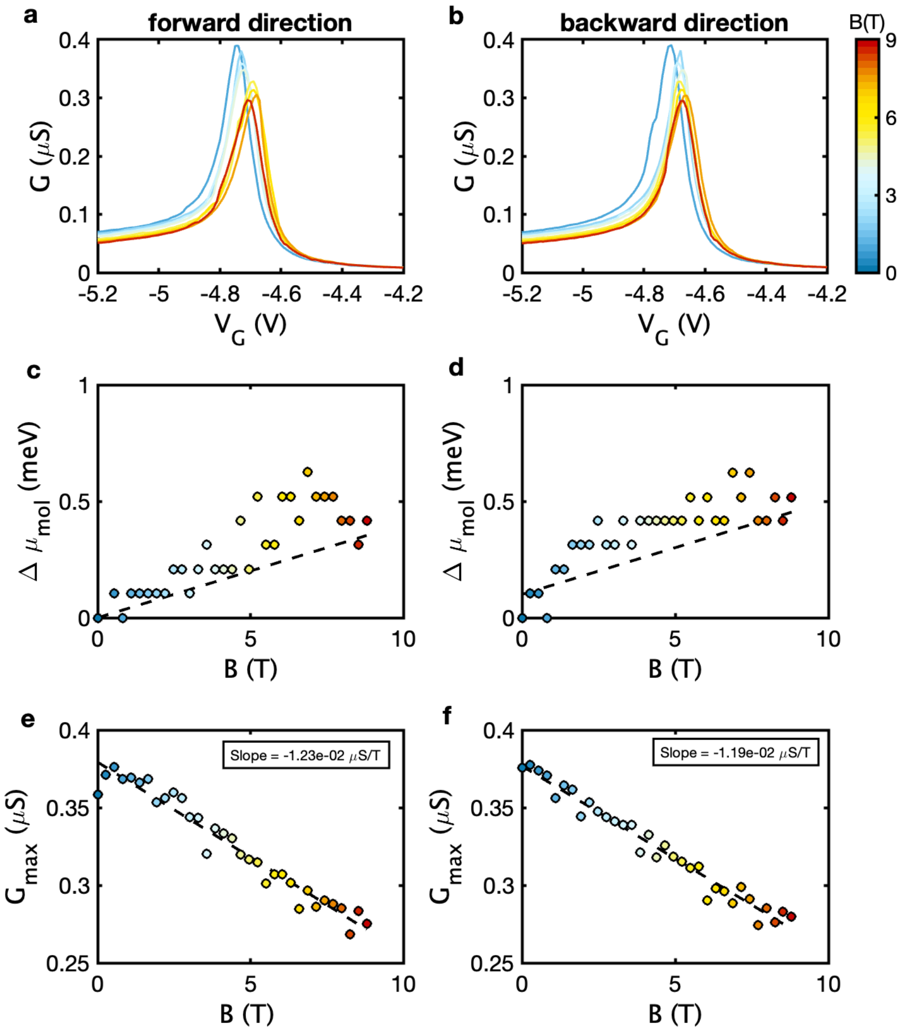

Figure 6.5: (a and b) Conductance vs. gate voltage across the charge neutrality point of device E at different temperatures from a negative value to a positive value of the gate voltage (forward - left) and opposite direction (backward - right). (c and d) chemical potential shifts as a function of the magnetic field extracted from the center of the charge degeneracy point and capacitive coupling to the gate $\Delta\mu_{mol} = \alpha\Delta V_g$ with $\alpha =$. The shift is in accordance with a value of $\frac{1}{2}g\mu_B\mathbf{B}$ and uncertainties are in the range of 30%. (e and f) Conductance of the charge degeneracy point as a function of the magnetic field; insets display the value of the best fit to the data (black dotted line) similar for both directions.

7

KONDO RESONANCES IN ALL-ORGANIC DI-RADICAL MOLECULAR BREAK JUNCTION DEVICES

> *Any moron can obtain weapons,*
> *but what he does with these weapons is the factor*
> *which will determine the success or failure of a particular operation.*
>
> William Powell - *The Arnachist Cookbook*

In this chapter, we compile observations of the Kondo effect in all-organic di-radical molecular junctions formed in two different devices geometries: the mechanically controlled break junctions (MCBJ) and the electro-migration break junctions (EMBJ). By applying mechanical strain in the MCBJ and gate voltage in the EMBJ, the Kondo correlations can be modified and the ground state of the di-radical can be reduced/oxidized between an $N = 1$ *and* $N = 2$ *occupancy on the molecule. Using resonances width, broadening with temperature and magnetic field splitting, we observe both the fully screened* $S = 1/2$ *and underscreened* $S = 1$ *Kondo regimes. Finally, we discuss cases extending beyond the single channel* $S = 1/2$ *Kondo effect and point out the similar qualitative behavior of the conductance at low temperature between the two-stage Kondo effect and the singlet-triplet Kondo effect.*

7.1. INTRODUCTION

Since their first synthesis in the early 1900 [110, 131, 132], polycyclic aromatic hydrocarbons (PAHs) polyradicals have gathered renewed attention over the last decade [75, 111, 113]. Their appealing properties harvested interdisciplinary investigations both for their fundamental interest and potential applications [24, 109, 133]. The semi-filled π-orbitals of PAH radicals can retain unpaired magnetic impurities up to room temperature owing to large delocalisation of the charge and steric hindrance increasing stability against chemical reactions [93]. Furthermore, π-magnetism exhibits a higher degree of delocalisation and isotropy, and is less impacted by decoherence compared to magnetism originating from d-orbitals. Nevertheless, these characteristics come with a high sensitivity of the electronic configuration on the geometric conformation of the molecule and its surrounding electrostatic environment due to the polarisability of carbon-carbon bonds.

A fundamental manifestation of the interaction between a localised magnetic moment and its environment is the Kondo effect [56], where conduction electrons form a spin cloud around the magnetic impurity screening it. The strong electron-electron interactions lead to a pronounced zero-bias Kondo resonance in the differential conductance spectra that cannot be accounted for in a single-particle model. Since its first experimental observation, the Kondo effect has been studied in a variety of systems, including semiconductor quantum dots [134–136], magnetic atoms [137–139], carbon nanostructures [113, 140, 141] and also in single molecules using scanning tunneling microscope [142, 143], mechanically controlled break junctions [82, 98, 144] and single molecule transistors [88, 118, 128]. The many-body highly correlated state arising from this phenomenon may help to understand better decoherence and screening of the electronic states in nanometer-sized systems.

In this chapter, we report on Kondo resonances arising from the unpaired spins of all-organic PAH di-radical 2-OS and Sme-2OS molecular break junctions at low temperature in the two and three-terminal device configurations. The two di-radicals used, 2-OS and Sme-2OS, are depicted in figure 7.1 (a, top and bottom respectively). The backbone of both molecules is composed of two fluorene moieties hosting radical centers linked by two anthracene units. Sme-2OS (figure 7.1 a) holds additional sulfur-methyl groups with benzene rings stabilizing the molecule-metal interfaces. More details on the synthesis of the di-radical can be found in [76] and [145].

Previous work demonstrated that these di-radicals retain their magnetism upon integration in solid-state devices and that the molecules can be gate-tuned through a reversible redox reaction between singly and doubly occupied states (see chapter 5). When the molecule is in the $N = 2$ state, the exchange coupling between the radical electrons can be either ferromagnetic (triplet ground state, $S = 1$) or anti-ferromagnetic (singlet ground state, $S = 0$) depending on the exact molecule conformation in the junction. Some configurations lead to the quenching of one of the magnetic impurities, leaving the radical in a $S = 1/2$ state. Alternative configurations with small to no singlet-triplet splitting may lead to two independent $S = 1/2$ impurities, leaving the molecule in a biradical state. We find Kondo temperatures that range from a few K to several tens of K, allowing for a study of Kondo crossovers regimes at relatively high temperatures (above a Kelvin). We compare the effects of mechanical manipulation, electrostatic gat-

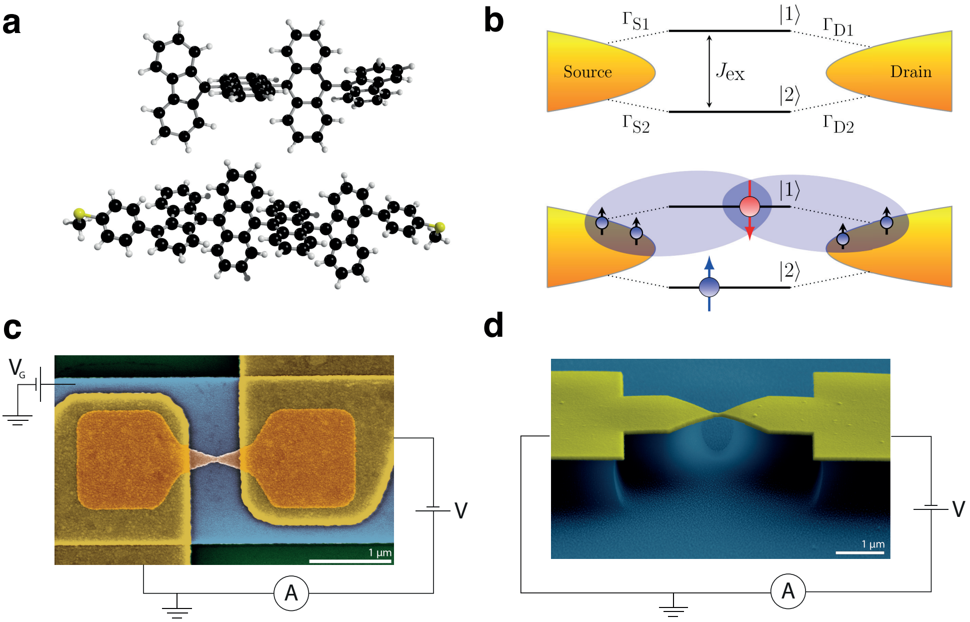

Figure 7.1: (a) Schematic representation of the (top) 2OS and (bottom) Sme-2OS di-radical molecules. The magnetic impurities are localised in the fluorene moieties separated by two anthracene units with a angular degree of freedom. The Sme-diracical holds additional sulfur-methyl groups with benzene rings acting as anchoring groups. (b) Top: schematic representation of a di-radical molecular junction where two molecular orbital with a tunneling amplitude τ between them, giving rise to an exchange coupling J_{ex} coupled to source and drain electrodes through tunnel coupling terms Γ. Bottom: when a molecular orbital is strongly coupled the conduction bath, the Kondo effect leads to a polarisation of the conduction electrons cloud around the localised magnetic impurity in order to screen it. (c) Scanning electron microscopy (SEM) image of a mechanically controlled break junction (MCBJ) device and (d) an electromigration break junction (EMBJ) device.

ing, magnetic field splitting and temperature dependence of Kondo resonances in these all-organic di-radical molecular junctions and outline compatibility of the results with $S = 1/2$ Kondo effect. Then, by comparing the transitions of the electronic transport fingerprints, we point out cases extending beyond the single screening channel spin-$\frac{1}{2}$ Kondo effect.

Di-radicals measurements are carried out using two different methods: the electromigration break junction (EMBJ) technique and the mechanically controlled break junction (MCBJ) technique, depicted respectively in figure 7.1 c and d. By mechanical manipulation with the MCBJ technique, the molecule-metal geometries can be adjusted while recording the two-terminal current-voltage (IV) characteristics of the molecular junction. MCBJ allow the probe of many different junction geometries in a single experiment, while an EMBJ gap is fixed once it has been opened and supports the measurement of only a single configuration per junction. By incorporating a third gate electrode, the EMBJ devices are able to tune the electrostatic environment by applying a voltage to the gate and adjusting the alignment of the molecular orbitals with respect to the chemical potentials of the electrodes. Additionally, EMBJ devices support temperature-dependent measurements. In both cases, we measure the current, I, as a function of applied DC bias voltage, V, between the source and drain electrodes and use a numerical Savitzky-Golay filter to obtain the differential conductance $\mathrm{d}I/\mathrm{d}V$.

7.2. RESULTS

We measured 75 devices in EMBJ and 6646 in MCBJ, both in the presence of Sme-2OS (respectively 41 for EMBJ and 4532 for MCBJ) and 2OS (34 for EMBJ and 2114 in MCBJ). Inelastic spin-flip tunnelling spectra are observed in the $\mathrm{d}I/\mathrm{d}V$ spectra in 1 % of the devices with an exchange coupling in the range of 10 meV. 2.7 % of 2OS MCBJ devices display Kondo resonances, 1.9 % in the SMe-2OS and 5.9 % in the 2OS EMBJ devices and 7.3 % in the Sme-2OS EMBJ device. The statistics are summarized in SI figure 7.8. Here, we will highlight different examples on how to quantify and control the Kondo physics in di-radical molecular junctions.

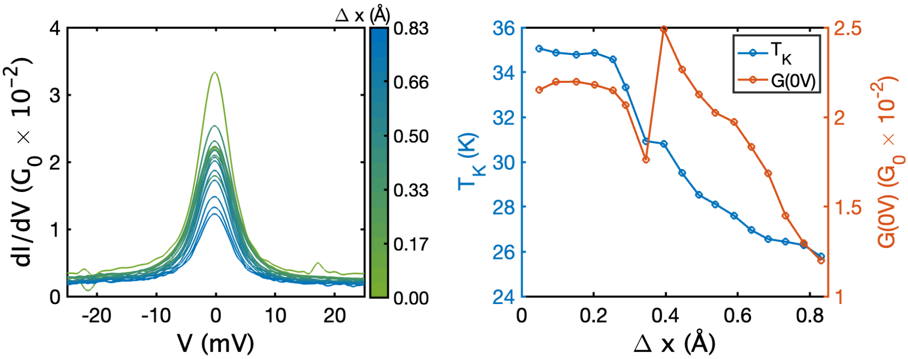

Figure 7.2: (left) Differential conductance ($\mathrm{d}I/\mathrm{d}V$) as a function of bias voltage of a 2-OS molecular junction in MCBJ at low temperature for increasing electrodes-electrodes distance (Δx). (right) Fitting the Kondo resonances to a Lorentzian, the extracted full-width half maximum (FWHM; blue curve) as a function of electrode distance decrease monotonically resulting from the Kondo temperature reduction due to the increased tunnel barrier length. Differential conductance at zero-bias (red curve) display a jump after 0.4 Å electrode spacing increase while the FWHM decreases in the meantime indicating relaxation of the tensile stress in the gold electrodes resulting in an increased amount of direct tunneling between the two electrodes relative to scattering through the quantum transport channel.

7.2.1. MECHANICAL MANIPULATION OF T_K

The MCBJ devices allow for adjustment of the size of the gap to further modify the geometry of a junction once a molecule is sandwiched between the metallic electrodes, and rearrange the molecule couplings to the source and drain (Γ on figure 7.1 b). On the left side of figure 7.2, we show successive differential conductance spectra of a 2-OS MCBJ molecular junction for increasing electrodes spacing (Δx). By changing the gold electrode gap, the tunnel couplings (and therefore the capacitive couplings) of the molecule with the electrodes increase. The dependence of the gap size on the electrode spacing is not necessarily monotonic and continuous as the reorganisation of gold in the electrodes may spontaneously release mechanical stress, restructuring the junction geometry and changing the conductance. Fitting the Kondo resonances to a Lorentzian (the procedure is detailed in Appendix 7.4.1), one can estimate the Kondo temperature for a $S = 1/2$ screening from the extracted full-width half maximum (FWHM):

$$\text{FWHM} = \frac{2}{e}\sqrt{(\pi k_B T)^2 + 2(\pi k_B T_K)^2}, \tag{7.1}$$

with k_B the Boltzman constant, T the temperature and T_K the Kondo temperature. On the right side of figure 7.2, we see that the characteristic energy of the Kondo effect, the Kondo temperature, decreases monotonically for increasing electrode distance, i.e., increasing the tunnel barriers.

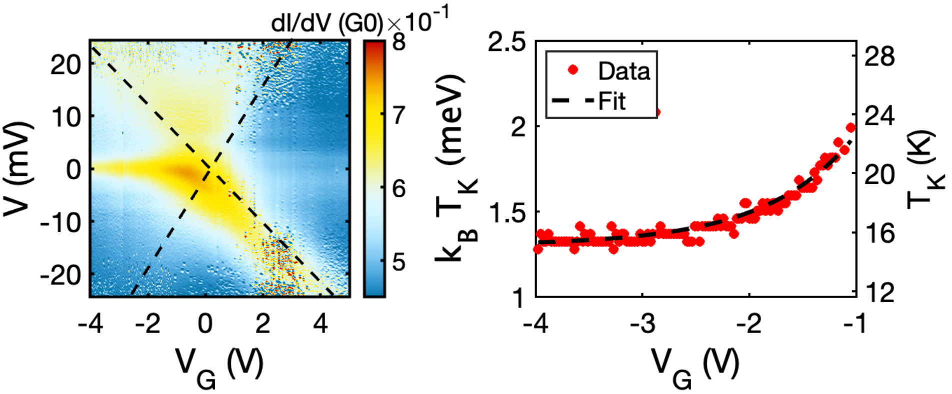

Figure 7.3: (left) Stability diagram (dI/dV as a function of bias and gate voltage) of a 2-OS molecular junction in EMBJ at low temperature (device F from chapter 5). Dashed lines highlight the corners of the Coulomb diamond with the charge degeneracy point at $V = 0$ V. (b) Kondo energy (left axis) and the corresponding Kondo temperature (right axis) extracted from zero-bias resonances fits to a Lorentzian (see SI 7.4.1) with $T = 2$ K. The black line correspond to the best fit to the Haldane relation 7.3 with $\Gamma = 90$ mV, $U = 240$ mV assuming a charge degeneracy point at $V_G = 0.4$ V.

7.2.2. GATE DEPENDENCE OF T_K

The many-body singlet state formed by the localised magnetic impurities with the conduction electrons occurs through an exchange process where an electron jumps off the molecule to the electrodes bath. At the same time, another one must replace it on a time scale h/ϵ_0, where ϵ_0 is the energy level of the molecule. An antiferromagnetic Heisenberg exchange interaction, J, describe such a cotunneling process in an interaction Hamiltonian:

$$H_{\text{int}} = \sum_{\lambda} J_\lambda \mathbf{s}_{\text{bath}} \times \mathbf{S}_\lambda \tag{7.2}$$

between the λ spins in the molecule $\mathbf{S}_\lambda$ and the sum of spin operators of the conduction electrons $\mathbf{s}_{\text{bath}}$. We can represent the di-radical molecular transistors by two molecular orbitals, $|1\rangle$ and $|2\rangle$, coupled to source and drain leads through tunnel barriers (see figure 7.1 b). Each magnetic impurity has a screening channel with a Kondo temperature, $T_{K\lambda} \propto \Gamma_\lambda = \Gamma_{\lambda S} + \Gamma_{\lambda D}$. When the radical is in its $N = 1$ state, or if the experimental temperature is in the range $T_{K2} \ll T \leq T_{K1}$, only one screening channel is effective as depicted in the bottom figure 7.1 b. However, the binding energy is not simply proportional to this coupling strength. The Kondo temperature dependence on the barrier size is described in the relation developed by Haldane [146]:

$$k_B T_K = \frac{\sqrt{\Gamma U}}{2} e^{-\pi\epsilon_0(-\epsilon_0+U)/\Gamma U}, \tag{7.3}$$

where the Kondo temperature is expressed as a function of, U, the on-site repulsion, ϵ_0 the energy level of the molecule through which transport occurs and Γ, the sum of the tunnelling barriers widths. The exponential dependence of T_K on Γ highlight the susceptibility to the exact molecule-metal geometry. In EMBJs, the tunnel barriers are fixed. However, the capacitive coupling of the molecule to the gate allows for tuning the alignment of the molecular molecular orbitals with the chemical potentials of the electrodes.

At sufficiently large bias voltages, an accessible level is present in the range between the chemical potentials of the two electrodes, leading to resonant tunnelling through the molecule, producing a peak in the $\mathrm{d}I/\mathrm{d}V$. Thus, the gate bias shifts the source-drain voltage at which resonant transport occurs. Measurements of $\mathrm{d}I/\mathrm{d}V$ as a function of different gate voltages are compiled in a "stability diagram" as displayed in the left plot of figure 7.3. Typically, in molecular devices, a single molecule transistor is characterised by a hour glass like structure where the current is blockaded on both sides where the molecule maintains a consistent charge state. When the gate voltage is tuned to align a molecular orbital with the Fermi energy in the junction, resonant tunnelling occurs at zero bias and the molecule transition between distinct charge state. This point is referred to as the "Charge degeneracy point" (CDP) of a Coulomb diamond. The dependence on the location of the chemical potential ϵ_0 is employable to fit the gate dependence of a $S = 1/2$ Kondo resonance.

In the left plot of figure 7.3, we show a stability diagram from a 2-OS molecular junction in an EMBJ device. Edge of two Coulomb diamonds (highlighted by black dashed lines) indicates a change in the molecular charge state between the left and the right side of the diamond. The blockaded region on the right of the CDP displays a small spin-flip signal with large Kondo correlation compatible with a doubly occupied singlet ground state. On the left side of the diamond, the odd charge state displays a zero-bias resonance with tunable height and full-width half maximum using the gate voltage. The Kondo resonances are fit to a Lorentzian, and using equation 7.1; the corresponding Kondo energy and Kondo temperatures are displayed on the right plot of figure 7.3 as a function of gate voltage. The exponential dependence of the Kondo temperature on the gate bias expected from the Haldane relation 7.3 is displayed as the dashed black line in the right figure 7.3. A good correspondence is found.

7.2.3. MAGNETIC FIELD DEPENDENCE

A $S = 1/2$ Kondo resonance is expected to split by $2g\mu_b B$ in the presence of an external magnetic field due to the Zeeman effect. The doublet ground state degeneracy of a single

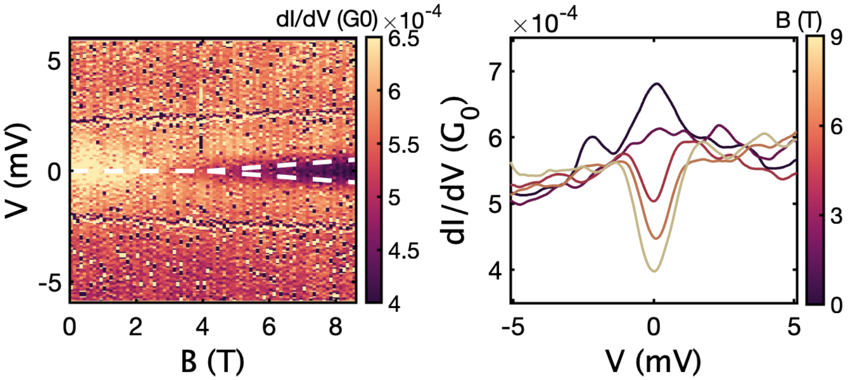

Figure 7.4: (left) $\mathrm{d}I/\mathrm{d}V$ as a function of bias voltage and external magnetic field up to 9 T. The white dashed lines corresponds to a splitting of $2g\mu_bB$ with $g = 2$ above a critical magnetic field of 4.1 T. (right) $\mathrm{d}I/\mathrm{d}V$ vertical linecuts from left figure for different magnetic fields applied along normal direction of the device.

magnetic impurity is thus lifted with a magnetic field. An exchange interaction between the two states arises, and a dip appears around zero bias in the $\mathrm{d}I/\mathrm{d}V$ spectra due to the associated inelastic spin-flip processes. This results in splitting from a single Kondo peak to two distinct peaks taking place above a threshold magnetic field B_C. The relation between B_C and T_K has been studied using the numerical renormalisation group (NRG) yielding a critical field $B_\mathrm{C} = \frac{0.5k_\mathrm{B}T_\mathrm{K}}{g\mu_\mathrm{B}}$ for a $S = 1/2$ screening with $g = 2$ [147]. Some measurements in MCBJ highlighted Kondo temperatures corresponding to several tens of K, too large to be split with an 8 T magnetic field.

The magnetic field dependence of the $\mathrm{d}I/\mathrm{d}V$ spectra in an EMBJ Sme-2OS molecular junction in the odd charge state of a Coulomb diamond is displayed in figure 7.4. The dashed lines on the left panel represent a splitting of $|2g\mu_\mathrm{b}\mathrm{B}|$ corresponding well to the opening of the conductance dip at zero-bias with $g = 2$. The FWHM of the resonance at 0 T extracted from the fit to a Lorentzian is 2.8 meV at 1.7 K, corresponding to a Kondo temperature of 11 K. The opening of the dip matches well with the value expected from $\frac{0.5k_\mathrm{B}T_\mathrm{K}}{g\mu_\mathrm{B}} \approx 4.1$ T. We note the constraint that the thermal excitation must be smaller than the critical magnetic field $T < \frac{g\mu_\mathrm{B}B_\mathrm{C}}{k_\mathrm{B}}$ (see SI section 7.4.3).

7.2.4. TEMPERATURE DEPENDENCE

The results presented can be explained by a single $S = 1/2$ impurity coupled to a single Kondo screening channel. The total spin effectively screened can be larger than 1/2, and Kondo resonances in the even charge state of molecular devices have been experimentally observed [148]. The two molecular orbitals, each occupied by a radical electron, can have different couplings to the electrodes yielding two distinct energy scales, T_K1 and T_K1. In this picture, as the Kondo energy scale depends exponentially on the coupling strengths, a large number of molecular junction geometries lead to two different Kondo temperatures $T_\mathrm{K1} \gg T_\mathrm{K2}$. If the temperature of the experiment is above the lowest Kondo temperature, $T_\mathrm{K2} \ll T < T_\mathrm{K1}$, a single screening process is apparent and resonances are

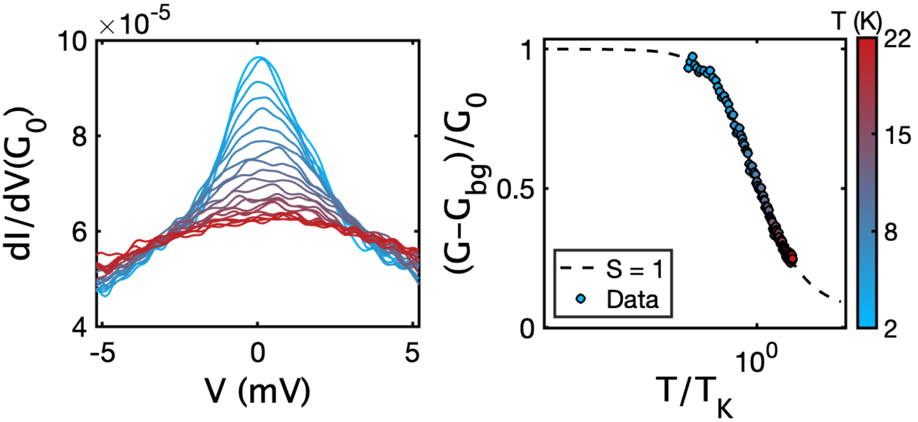

Figure 7.5: (left) $\mathrm{d}I/\mathrm{d}V$ as a function of bias voltage for different temperatures in Sme-2OS molecular junction in EMBJ. (right) Normalised zero-bias conductance as a function of T/T_K extracted from left figure. Dashed lines corresponds to the best fit to equation 7.4 with parameters $T_\mathrm{K} = 9$ K, $G_\mathrm{b} = 0.54$ and $s = 0.7$ corresponding to a $S = 1$ Kondo temperature evolution.

in the underscreened regime. The logarithmic dependence of the zero-bias conductance as a function of temperature is contingent upon the total screened spin, as highlighted in the formula described by Goldhaber-Gordon *et al.* [149]:

$$G(T, V=0) = \frac{G(T=0)}{\left(1+(2^{1/s}-1)(T/T_\mathrm{K})^2\right)^s} + G_\mathrm{b}, \tag{7.4}$$

with s the empirical spin parameter (where $s = 0.22$ for $S = \frac{1}{2}$ and $s = 0.7$ for $S = 1$), $G(T=0)$ the peak conductance at 0 V in the $T \to 0$ K limit and G_b the background conductance at finite voltages. Equation 7.4 enables one to estimate the total spin screened in a molecular junction by recording $\mathrm{d}I/\mathrm{d}V$ for different temperatures. Larger temperatures activate vibrational modes that can result in increased noise in the junction. Thermal energy also increases the diffusion of the molecule and, with it, the probability of changing the molecule-metal geometries. Figure 7.5 displays an example of temperature dependence measurements of a Kondo resonance in the $\mathrm{d}I/\mathrm{d}V$ spectra of Sme-2OS molecular junction in EMBJ device.

The sharp resonance of figure 7.5 at an initial temperature of 1.7 K broadens and reduces to half of its conductance around a temperature of 10 K. The full-width half maximum of the Kondo resonance fit to a Lorentzian is around 2 meV at 1.7 K, corresponding to a Kondo temperature in the 10 K range. We fit the zero-bias conductance of the Kondo peaks using equation 7.4 on the right side of the figure. The result of the fits converge to higher spin values than $s = 0.22$, indicating the temperature evolution of a $S = 1$ Kondo resonance. In this junction, the molecule could not be reduced or oxidised. A fit to $s = 0.22$ (displayed in SI figure 7.10) converge to an inconsistent Kondo temperature of about 20 K with a smaller G_b. Note, that a broad range of temperatures should be measured to fit the Goldhaber-Gordon relation 7.4 with reasonable accuracy, especially on the plateau at fractions of the Kondo temperature in the strong coupling regime.

Numerical and analytical investigations focusing on the electron-phonon coupling relation with Kondo correlations confirmed that vibronic modes can alter the spin 1/2 impurity behaviour. Intramolecular electron-electron interactions and couplings to the leads are renormalised by additional interaction with a phonon mode, leading to an increased value of T_K, a weak gate voltage dependence and anomalous behaviour of Coulomb diamond edges [150]. The zero-bias peak in figure 7.5 did not split up to an applied magnetic field of 9 T (figure SI). We note that such a signature has been discussed in the context of strong electron-phonon coupling when the on-site repulsion can be renormalised to a negative value in specific cases [151].

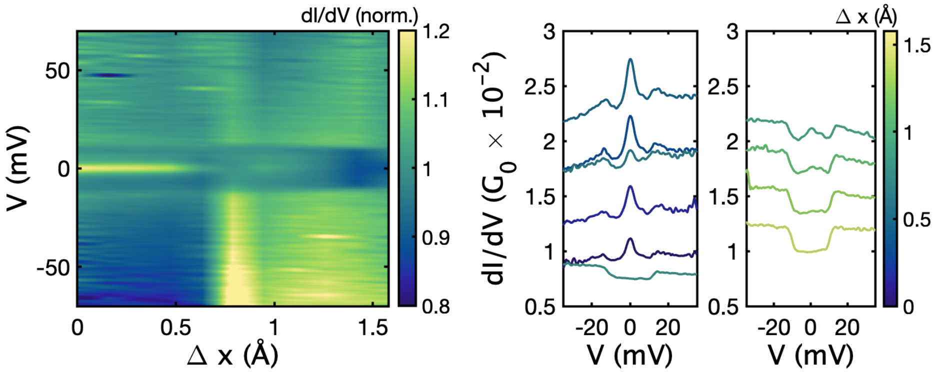

Figure 7.6: (left) dI/dV as a function of bias voltage and electrodes spacing in a 2OS molecular junction in MCBJ. (right) dI/dV linecuts from left figure for increasing electrodes spacing. Some signals display different behaviour with the same background conductance highlighting the importance of the exact molecule-metal conformation defining the fingerprint observed in the dI/dV. The sharp Kondo resonance accompanied by two satellites peaks initially turns in a flat inelastic spin-flip excitation with a change of background conductance highlighting the mechanically induced charge state transition from $N = 1$ to $N = 2$.

7.2.5. MECHANICAL MANIPULATION OF KONDO REGIME

When the number of screening channels $n < 2S$, the impurity is partially screened by conduction electrons forming an underscreened Kondo resonance. Mechanical manipulation can influence this screening regime by tuning either the number of screening channels or the total spin of the molecule. An example of mechanical manipulation with a transition from a completely screened to an underscreened Kondo resonance in a 2-OS MCBJ molecular junction is shown in figure 7.6. At small electrode distances, the dI/dV spectra display a zero bias resonance accompanied by two satellite peaks around ±10 mV. In the first four spectra, increasing the electrode distance increases the Kondo correlations and the background conductance. Between the 5th and the 6th spectras, around $\Delta x \approx 0.7$ Å, the background slope changes sign and Kondo correlations disappear, leaving a spin-flip signal with an exchange coupling close to 10 mV. This change of background asymmetry in the differential conductance spectra is also observed between the left and right sides of di-radical junction displaying Coulomb diamonds: we observe a positive conductance background slope as a function of bias voltage in the odd states and a negative slope in the even states (see SI figure 7.14). The four spectra following this background change show a decrease in the Kondo correlations at the bottom of the dip and an overall decrease in the conductance simultaneously. These characteristic fingerprints indicate a transition to an underscreened Kondo state with a change of the ground state from $S = 1/2$ to $S = 1$ and a single screening channel. The underscreened Kondo resonance at the bottom of a ferromagnetic spin-flip signal splits with a magnetic field of $2g\mu_B B$ above a smaller threshold magnetic field than for $S = 1/2$ screening [76]. This result shows that the electrodes-molecule geometry not only influences the tunnel couplings (through Γ in the Haldane relation 7.3) but also the relative position of the level, ϵ_0, up to oxidising or reducing the di-radical beyond the CDP.

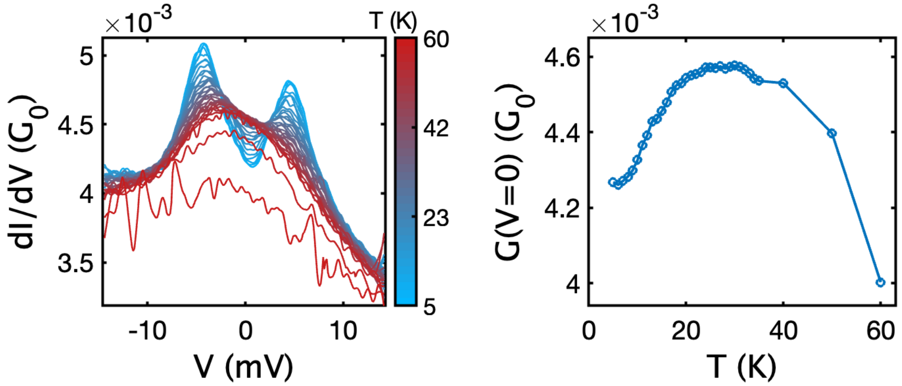

Figure 7.7: (left) Double peak centered around zero-bias in the dI/dV spectra of a 2OS EMBJ molecular junction for increasing temperatures from 5 to 60 K. (right) Differential conductance at zero-bias as a function of temperature extracted from the left plot. The dip around zero-bias is closing first, increasing the zero-bias conductance up to the first Kondo temperature T_{K1} around 10-20 K. The height of the resulting resonance decreases as well at temperatures above $T_{K2} \approx 50$ K.

7.2.6. TWO-STAGE KONDO

When the experimental temperature is below both Kondo energy scales (T_{K1} and T_{K2}), a second screening channel opens for the impurity to be fully screened. This situation referred to as the two-stage Kondo effect, leads to a non-monotonic behaviour of the zero-bias conductance as a function of temperature [152]. In the case of a singlet ground state, $S = 0$, the Kondo resonance is expected to be in the overscreening regime if there is one or more screening channels ($n > 2S$). In case the exchange coupling between the two impurities is larger than the level broadening, screening is absent around zero-bias at the bottom of the dip in the dI/dV spectra, and the current is blocked (see SI figure 7.14 device E). The Kondo correlations recover at finite bias when the difference of chemical potential between the source and drain exceeds the energy to the triplet transition in the form of step's conductance overshoots in the IETS spectra. On the left side of figure 7.11, the conductance at zero bias increases with increasing temperatures while the height of the two symmetric peaks around zero bias reduces until a single peak is visible in the differential conductance spectra. Increasing the temperature further yields a decrease in the zero-bias conductance, and the resonance continues to broaden. The corresponding zero-bias conductance displayed as a function of temperature (right side of figure 7.11) is in agreement with the evolution expected for a two-stage Kondo effect [152]. In a magnetic field, when the singlet and lowest triplet state are close in energy, the split resonance is expected to restore to a single peak above a magnetic field $B > \frac{J_{\mathrm{ex}}}{g\mu_{\mathrm{B}}}$ for an antiferromagnetic exchange coupling or to only split further in case of ferromagnetic coupling (as observed in [153]).

When the ground and excited states are degenerate (exchange interaction is close to 0), the tunnelling amplitude between the two radicals sites is renormalised by Coulomb interactions. The two spins can act either as two independent $S = 1/2$ impurities (as a biradical at small tunnelling amplitudes) or be in a crossover regime between the triplet and the locked singlet resulting in the singlet-triplet Kondo effect [154] (at intermediate tunnelling amplitudes). This situation leads to a non-monotonic $G(T)$ with a pronounced peak around $k_{\mathrm{B}}T = J_{\mathrm{ex}}$ which is broadening with increased inter-dot tunnelling. In this case, when the singlet-triplet transition energy, J_{ex}, is smaller than the level broadening from the degenerate state participating to Kondo assisted transport, Γ, we can expect contributions to the conductance around zero-bias. The resonance appears as a split peak centred around zero-bias as in the right charge state of the Coulomb diamond in figure 7.3. The distance between the two peaks corresponds to the exchange coupling between the ground and excited states and the bottom of the dip at zero-bias has a higher conductance than the background at larger bias voltages. This behaviour is described in the calculations from Ref.[155], which predict a non-monotonic evolution with temperature of the zero-bias conductance when the inter-dot tunnelling amplitude is in the range of $t \sim \sqrt{U' T_{\mathrm{K}}}$ with U' the on-site extended Coulomb repulsion and $J_{\mathrm{ex}} \sim T_{\mathrm{K}}$.

7.3. CONCLUSION

In conclusion, we reported on Kondo resonances originating from the unpaired spins of the all-organic PAH di-radicals, 2-OS and Sme-2OS, in low-temperature, two- and three-terminal device configurations, and highlight the influence of mechanical manipulation, electrostatic gating, magnetic field splitting and temperature broadening on the conductance spectra. We determined the Kondo temperatures with three complementary methods (bias width, magnetic field splitting and temperature dependence) and pointed out their limitations. The di-radical can be reduced to a single radical either by gate voltage or mechanically, yielding a $S = 1/2$ Kondo screening effect in agreement with the expected behaviour in this regime. The large Kondo temperatures of PAH polyradicals allow observation of both the completely screened $S = 1/2$, the underscreened $S = 1$ and the singlet-triplet Kondo regimes in a temperature range above a Kelvin. Some devices diverge from the expected behavior, such as the one with a narrow resonance unaffected by an external magnetic field with indications for a $S > 1$ spin state. We also showed with an example of the behaviour compatible with the two-stage Kondo effect as described in the literature and emphasiszed the similarities with the singlet-triplet Kondo effect when the binding energy is larger than the exchange coupling between the two magnetic impurities.

7.4. APPENDIX

We measured di-radical molecular junction formed with the 2-OS and Sme-2OS di-radical in 7 different mechanically controlled break junction (MCBJ) devices and 74 electromigration break junction (EMBJ) devices. The features observed are compiled in figure 7.8 for both MCBJ, EMBJ and all devices. The MCBJ devices are broken and fused back together yielding a different molecule metal-geometry each time the junction is broken. A detailed description of the MCBJ measuring technique can be found in [156, 157].

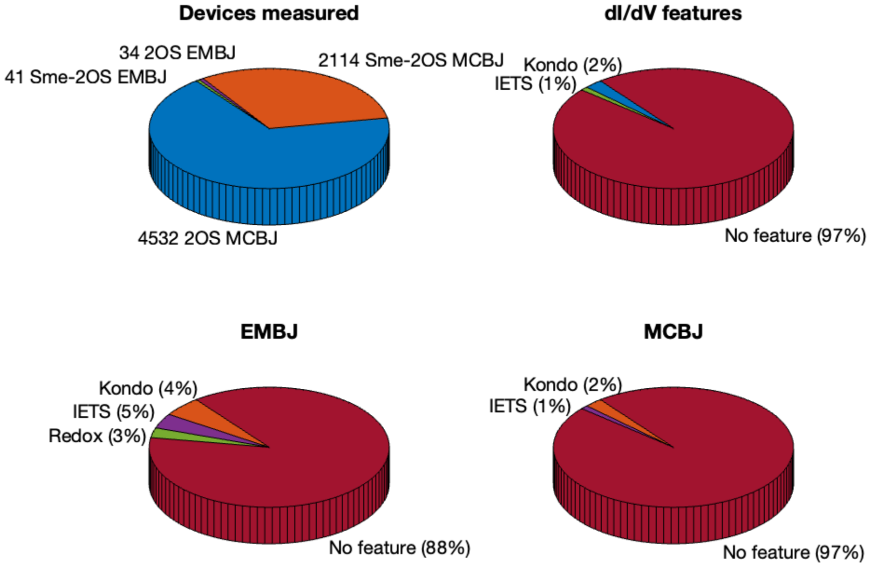

Figure 7.8: Statistics of the measured features in the dI/dV spectra of 2OS and Sme-2OS molecular junctions (top-right), in EMBJ (bottom-left) and MCBJ (bottom-right)

7.4.1. FIT OF THE KONDO RESONANCE

We used a Lorentzian function to estimate the Kondo temperatures from the full-width half maximum extracted of the fits:

$$y(x) = \mathrm{A} \times \frac{1}{1 + \left(\frac{x - \mathrm{x}_0}{\Gamma/2}\right)^2} + \mathrm{B}x + \mathrm{C}, \tag{7.5}$$

with A a scaling parameter, B the slope of the conductance, C a background conductance offset, x_0 the center of the resonance and Γ the full width at half maximum.

7.4.2. FITS TO THE HALDANE RELATION

In figure 7.10, we fit the zero-bias conductance of the resonances displayed in 7.5 as a function of temperature to the Goldhaber-Gordon relation (eq. 7.4 from main text) and constrain the spin parameter $s = 0.22$ corresponding to a spin-1/2 screening. The best fit

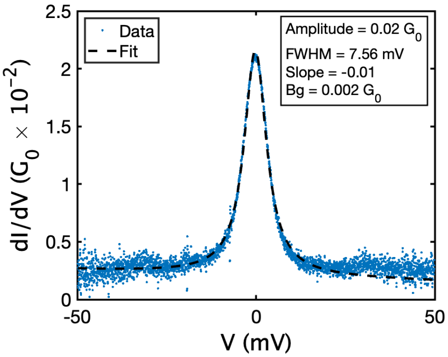

Figure 7.9: dI/dV as a function of bias of a Kondo resonance from figure 7.2. The black dashed line correspond to the best fit found to formula 7.5.

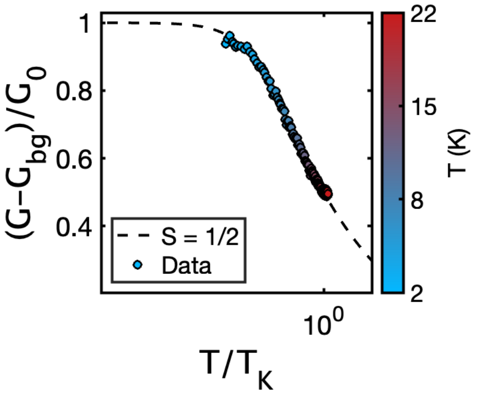

Figure 7.10: Best fit to the Haldane relation of the Kondo resonance amplitudes in function of the temperature for a $S = 1/2$ screening. Solution converge to a background of 0.24 and a Kondo temperature of 19 K.

converge to a Kondo temperature of 19 K, almost twice as expected with $s = 0.7$, with a background conductance of 2.3×10^{-5} G_0, half of the $S = 1$ fit background (5.2×10^{-5} G_0) which is corresponding well with the background observed experimentally in the dI/dV spectra.

In a similar way, we fit the double peak in the differential conductance spectra to the sum of two Lorentzian with different height and width as displayed in figure 7.11 and apply this procedure for the range of temperatures displayed on the right plot. The subtraction of the two fitted Lorentzian yield the black dashed line. The two heights extracted from Lorentzian fit are compared to the Goldhaber-Gordon relation and find that solution converges better to $S = 1/2$ for the outer resonance (red curve in 7.11) with a Kondo temperature of 55 K (which is the temperature at which the overall resonance broaden and zero-bias conductance decrease) and to $S = 1$ for the inner resonance (orange curve in 7.11) with a Kondo temperature of 13 K (corresponding well to the temperature where

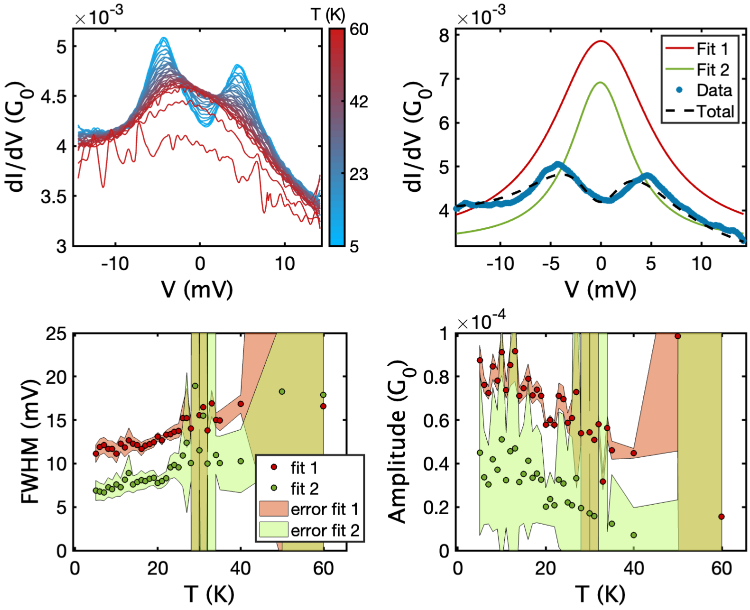

Figure 7.11: (left) Double peak in the dI/dV spectra of a 2OS molecular junction in EMBJ centered around zero-bias. We fit the signal using substraction of two lorentzian displayed as red and orangecurves yielding the black dashed line superposed to the blue data points. (right) dI/dV spectra as a function of temperature from 5 K to 60 K. The smaller resonance is closing first, increasing the zero-bias conductance up to the first Kondo temperature T_{K1}. The FWHM of the larger resonance is then decreasing as well as the zero-bias conductance at temperatures above T_{K2}.

the zero-bias dip vanishes leaving a single peak in the spectra) and show the results in figure 7.12.

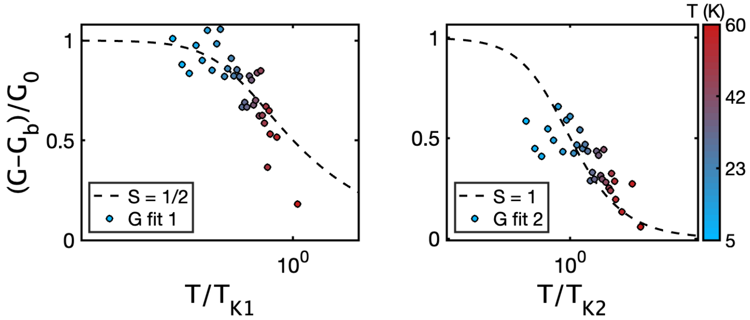

Figure 7.12: Best fit to the Goldhaber-Gordon relation of the Kondo resonances height extracted from fits of the sum of two Lorentzian (as displayed in figure 7.11) a function of the temperature. The first fit to T_{K1} is converging to a Kondo temperature of 55 K and a $S = 1/2$ temperature evolution while the second fit converge to a lower $T_{K2} \sim 13$ K with a spin 1 evolution.

7.4.3. MAGNETIC FIELD DEPENDENCE

The splitting of Kondo resonances in the dI/dV spectra as a function of external magnetic field is displayed for different 2-OS and Sme-2OS molecular junctions in figures 7.13. For the splitting to be observed the measurement temperature must be under the critical magnetic field energy $g\mu_b B_C/k_B$. The bottom-left signal is extracted from the ferromagnetic spin-flip signal in 2-OS MCBJ of[76], in this case the ground state is $S = 1$, therefor we expect a small critical magnetic field under the value observed of about 3 T corresponding to a temperature broadening of 4 to 5 K consistent with our measurements. Some zero-bias peaks are splitting while others are not, we doesn't expect the resonances to split if we meet the condition $B_C > \frac{k_B T}{g\mu_B}$ corresponding to a temperature $T < 0.5T_K$ in $S = 1/2$ single screening channel case.

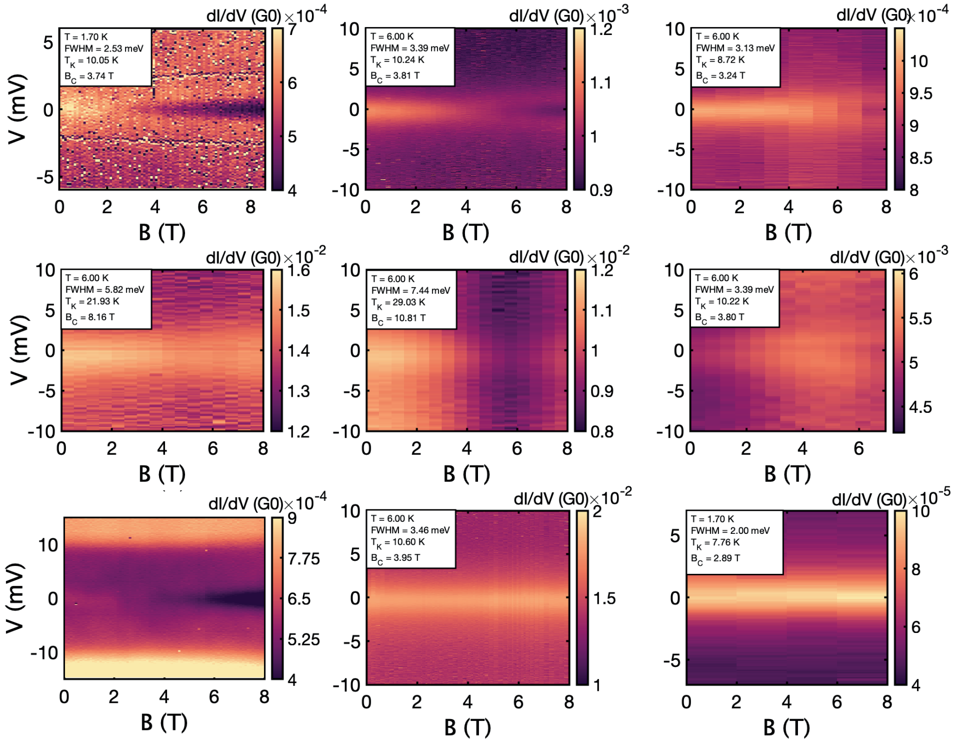

Figure 7.13: dI/dV as a function of bias voltage and magnetic field up to 8 T of 2OS and Sme molecular junction in MCBJ and EMBJ.

7.4.4. BACKGROUND MAGNETORESISTANCE

The magnetoresitance of the molecular junction highlight interesting features: in some cases where a Kondo resonance is observed in the differential conductance spectra, the background conductance is changing of more than 20 % at a magnetic field 8 T. We observe both an increase of the background conductance in some junction and a decrease in other examples. These observations are interesting to put in contrast with other experiments [144] where a larger magnetoresistance was observed for molecular junction that doesn't display Kondo resonances in their dI/dV spectras.

7.4.5. ASYMMETRY ODD/EVEN

We observe a change of background asymmetry in the dI/dV spectras when crossing the charge degeneracy point in the electromigrated break junctions as displayed in figure 7.14. Interestingly, we observe a change from a positive slope in the even charge states to a negative slope in the odd charge states in two different molecular junctions (left and center panels). During mechanical manipulation in the MCBJ (right panel), we observed a change from a Kondo resonance to a flat dip compatible with inelastic spin-flip excitation. This change could originate from a tunable exchange coupling between the radicals centers: when the exchange coupling is very small to null, the di-radical becomes a bi-radical and the configuration of the molecular junction is similar to two $S = 1/2$ molecules probed in parallel. Moving the electrodes changes the conformation of the molecule and the exchange coupling get to a negative value yielding a $S = 1$ system. However, considering the change of background asymmetry, this sequence is better explained by am effect similar to electrostatic gating of the molecule from the electrodes which results in its -real- reduction.

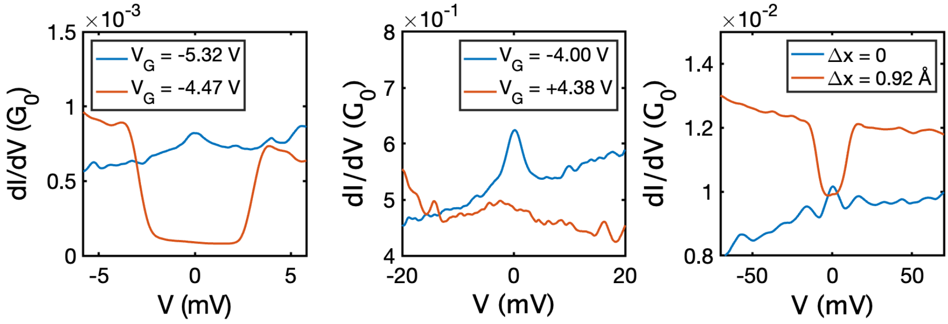

Figure 7.14: Comparison of the dI/dV as a function of bias voltage for: (a) Sme-2OS and (b) 2-OS in EMBJ for gate voltages in the (red) even and (blue) odd occupations of the di-radical junction and (c) 2-OS in MCBJ for different electrodes spacing.

8

MECHANICAL MANIPULATION OF AN ALL-ORGANIC DI-RADICAL IN SCANNING TUNNELING MICROSCOPE SINGLE-MOLECULE JUNCTIONS

L'image du jeu est sans doute la moins mauvaise pour évoquer les choses sociales.

De la règle aux stratégies : entretien avec Pierre Bourdieu, 1985

In this study, we investigate an all-organic di-radical molecule, employing the scanning tunnelling microscopy (STM) technique[1] *and compare the results with the ones on the same compound obatined in solid-state mechanically controlled break-junction (MCBJ) devices. Analysis of the two setups highlights the interplay between the geometry of the molecular junction and its electrostatic environment, producing specific magnetic fingerprints in the electronic transport spectra. The signals observed with both approaches are remarkably similar and can be altered by mechanical manipulation: by moving the tip in the scanning tunnelling microscope (STM) or by moving both electrodes in the mechanically controlled break junction (MCBJ). Comparing the results, we underscore the limits of each system and the spin signatures associated with the molecular junction conformation.*

---

[1] The STM measurements had been performed in the group of J.I. Pascual in San Sebastián (Spain) in close collarboration with Alessio Vegliante.

8.1. INTRODUCTION

Recent studies highlight all-organic polycyclic aromatic hydrocarbons (PAHs) polyradicals bearing promising properties, such as enhanced conductance [158–160], long coherence time [161–163] or large Seebeck coefficient [130, 133, 164]. The semi-filled orbitals enable unpaired magnetic impurities to persist in open-shell compounds up to room temperature by taking advantage of the large charge delocalization in the π-orbitals over the aromatic compounds and the steric hindrance of the molecule to avoid the reaction to the closed-shell form with hydrogen and oxygen. Advances in atomically precise bottom-up synthesis present new strategies to synthesize such compounds in sufficient purity to study their magnetic properties at the single-molecule level.

Although a few studies focus on PAH's properties at the single-molecule level [165], the link between the specific molecular conformation and the electronic properties of a molecular junction still needs to be explored. Integrating polyradicals in solid-state devices for fundamental studies remains challenging due to the limited control on the possible configurations of the molecule between metallic electrodes [82, 88, 92]. Some configurations may lead to the quench of one -or more- open-shell spin-center(s), altering or suppressing the magnetic properties of the molecule. In this chapter, we study an all-organic di-radical molecule, the Sme-2OS (schematically represented in figure 8.1). We assemble single-molecule junctions in a scanning tunnelling microscope (STM represented in figure 8.1 b) and compare the scanning tunnelling spectroscopy (STS) signal with results obtained with the same molecule measured in a mechanically controlled break junction (MCBJ represented in figure 8.1 a).

Despite differences in molecular deposition (see next section), a striking resemblance is seen in the $\mathrm{d}I/\mathrm{d}V$ signals observed using both setups as displayed in figure 8.2: Kondo resonances in the same range of energy (a,b), a split peak centered around zero bias (c,d), and spin-flip signals with a flat bottom and varying bias overshoot sizes (e,f,g,h). The STM spectra are obtained by contacting the molecule at different sites or by approaching the tip at different positions over the molecule. As indicated by the magnetic fingerprints in the differential conductance spectra, we will show in this chapter that the di-radical can be oxidized to a single radical depending on the exact molecular junction conformation, with spectra changing from a spin-flip dip to a Kondo resonance. Therefore, mechanical manipulation can lead to redox reactions analogously to electrostatic gating, as observed for molecular junctions formed in three-terminal solid-state devices (see chapter 5). A spin-flip signal with a small zero-bias contribution, a magnetic fingerprint associated with the ferromagnetic -triplet- ground state, is solely observed in the MCBJ experiments (see figure 8.2 i). The resemblance of the results in both setups indicates that similar molecular conformations are formed in both set-ups, despite the difference in contacting geometry, emphasizing the single-molecule character of junctions formed with the MCBJ technique; the ferromagnetic configuration is, however, exclusive to the MCBJ measurement method. The comparison allows a better understanding of the different conditions offered by the two measurement setups, their similarities and differences, using the same compound as a probe to their environment, and gathering a more exhaustive picture of its electronic properties.

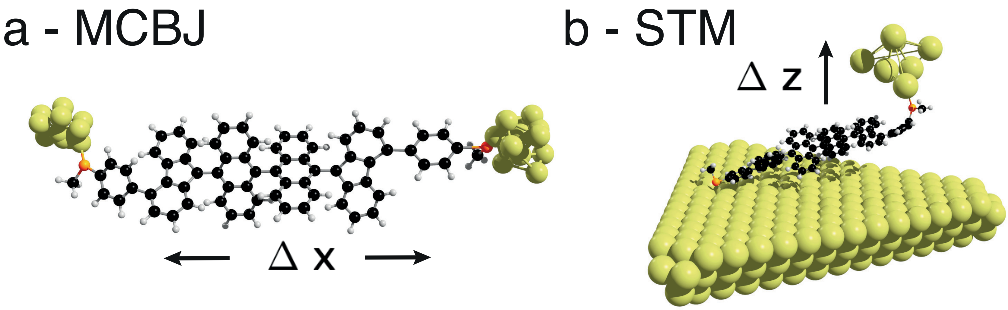

Figure 8.1: (a) Schematic representation of the Sme-2OS all-organic di-radical in a mechanically controlled break junction (MCBJ) and (b) in a scanning tunnelling microscope (STM). The di-radical is composed of two fluorene moieties holding a radical center, linked by two anthracenes with an angular rotational degree of freedom, with two benzene rings linking each anthracene to a sulfur-methyl group (orange). In the MCBJ setup the electrode spacing is controlled in the x direction by bending the substrate; in a STM setup the tip position is controlled relative to the substrate, and the electrode distance is controlled by lifting the tip in the z direction, normal to the plan of the substrate.

8.2. METHODS

Several techniques have been explored to form single-molecule devices by isolating a molecule between two metallic electrodes. It is convenient to model this setup as a double barrier tunnelling structure with the tunnel couplings defined by the molecule-metal interfaces [119]. Such a layout can be obtained with a STM, depicted in figure 8.1 b. In this setup, an atomically sharp metallic tip is controlled in the x, y and z directions with sub-nanometer resolution and the tunnelling current between the tip and a conducting substrate is measured, allowing to spatially map the local density of state (DOS) of the molecule lying on a flat metallic surface. In a STM experiment, the molecular species are typically deposited on the substrate by thermal sublimation to minimize surface contamination. Then, the metallic tip is placed above a molecule to obtain the double barrier junction configuration; the exact position of the tip with respect to the molecule determines the injection points from the tip into the molecule. The spatial resolution allows the analysis of current-bias characteristics at specific molecule positions so that $\mathrm{d}I/\mathrm{d}V$ features can be linked to a particular unit in the molecular structure. This technique is especially suited for flat molecules as the terminating atom of the STM tip can pick up a carbon-monoxide group to obtain bond-resolved topography of PAH species [166].

The core of the Sme-2OS molecule is similar to the 2-OS measured in previous chapters; the molecule structure is schematically represented in 8.1. It comprises of two fluorene moieties holding the radicals centers, linked by two anthracene groups with an angle in the carbon backbone axis. The core is stabilized and protected by benzene rings attached to the fluorenyl and a sulfur-methyl end group. The synthesis of Sme-2Os is detailed elsewhere [145].

In a MCBJ, the molecule is deposited on the junction by dropcasting a molecular solution of 1 mM concentration dissolved in dichloromethane (DCM), allowing the deposit of the di-radical without alteration during the procedure. Once the solvent has been evaporated, the sample space is pumped to 10^{-6} mbar and cooled to liquid helium temperature (~ 4 K). The junction is then broken in small steps (~ 5 picometers), and its current-bias characteristics are recorded by sweeping the potential difference between the source and drain electrodes while recording the output current until a molecular fingerprint is observed in the spectra.

STM deposition avoids the use of solvents for molecular deposition due to stringent cleanliness requirements within the system. Experiments are performed in an ultrahigh vacuum in the 10^{-11} mbar range to allow exact control of the metallic tip position with a sample space decoupled from room vibrations by several stages and cooled to liquid helium temperatures (similar to MCBJ, $T \approx 5$ K). Sample fabrication is as follow: a gold substrate is heated to several hundred °C to sublimate any unwanted organic compound on the metal and to form an atomically flat Au(111) surface. At the same time, thermal sublimation eliminates a portion of molecular hydrogen, a source of contamination that can react with molecules.

The Sme-2OS di-radical was initially deposited by thermal sublimation from a molecular powder in an ultrahigh vacuum at a temperature of 400 K. This method yields highly pure samples but poor control over the density of molecules deposited as it also depends on the exact molecules' properties at sublimation temperatures. This procedure, applied to the Sme-2OS di-radical, yielded various recomposed fragments from the original compound on the gold substrate (see appendix figure 8.6).

To prevent the molecule fragmentation we employed flash evaporation, wherein a few grains of the compounds in powder form are deposited on a doped silicon wafer covered with silicon oxide. Subsequently, sublimation was achieved by applying a current through the doped silicon rapidly increasing its temperature. In order to protect the molecule core during deposition, we used the Sme-2CS precursor molecule of the Sme-2OS di-radical with two OH groups linked to the fluorene moieties. The structures obtained by topography are challenging to link unambiguously to each chemical group composing the molecule as displayed in figure 8.3 a: the conformation highlights two central lobes in the topography, identified as the two anthracenes groups, each attached to a fluorenyl unit with a benzene ring and sulfur-methyl group at the ends of the structure.

Once a precursor molecule is found isolated on a clean part of the substrate, the STM tip is brought close to the presumed fluorenyl unit, where the OH is attached, and the voltage between the tip and the substrate is slowly increased while recording the current (see inset in figure 8.3 b). A jump in the current is observed above 2 V, signalling the rupture of the covalent liaison between the oxygen atom and the molecular backbone. Bringing the tip over the molecule after this procedure yields a zero-bias peak in the $\mathrm{d}I/\mathrm{d}V$ spectrum (see figure 8.3 c), with a larger signal to noise ratio close to the fluorenyl with removed hydroxyls. Bringing the tip close enough to a sulfur atom with a voltage applied yields another current jump, signalling the molecule's attachment to the tip. Support for this scenario is the presence of a small component close to the molecule (see appendix figure 8.7) after the manipulation that could correspond to the detached methyl group after the formation of a bond between the sulfur atom from the molecule and a gold atom at the apex of the tip.

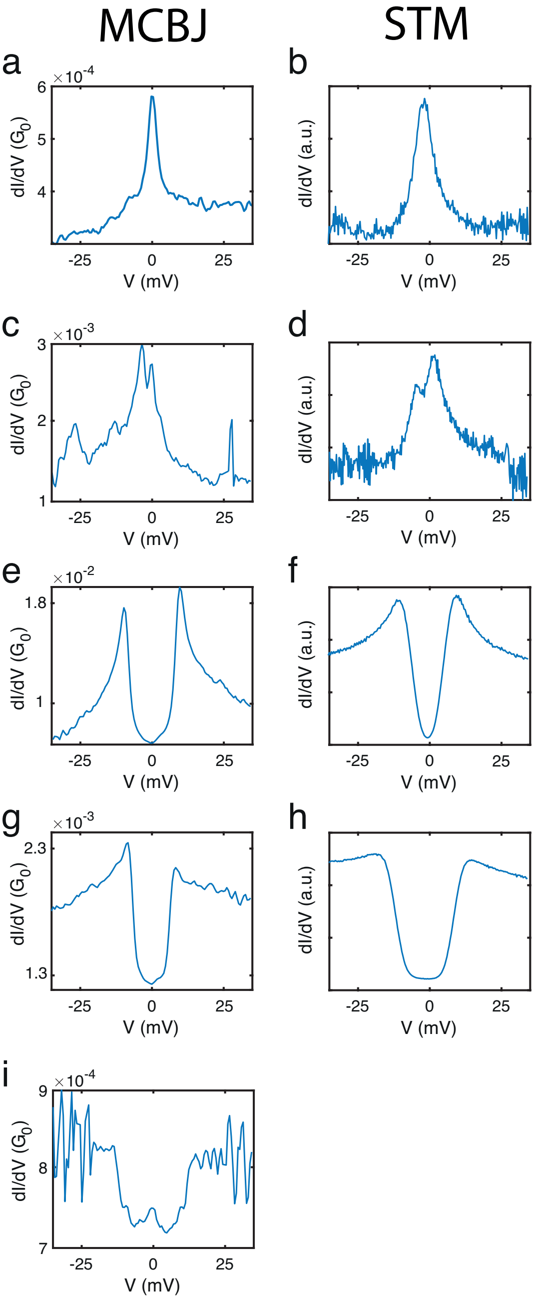

Figure 8.2: Differential conductance (dI/dV) spectra of Sme-2OS di-radical molecular junctions formed with (left panels) the MCBJ technique and (right panels) in an STM. (a and b) Zero-bias resonance ascribed to an $S = 1/2$ Kondo effect; (c and d) double peak centred around zero bias with a small exchange coupling and a conductance at zero bias above the spectra background; (e and f) inelastic spin-flip signals with large bias overshoots and a rounded bottom around zero bias; (g and h) inelastic spin-flip signals with smaller bias overshoots and a flat bottom; (i) small zero-bias peak at the bottom of a spin-flip signal indicating a ferromagnetic triplet ground state. The last signal is exclusively observed in MCBJ, both in molecular junctions formed with the Sme-2OS and 2OS di-radicals molecules.

8.3. RESULTS

8.3.1. SINGLE RADICAL

The result of differential conductance measurements as a function of the STM tip height is displayed in figure 8.4 (in a similar way as for MCBJ in figure 7.2). The full-width half-maximum (FWHM) of the zero-bias peak is linked to the Kondo temperature [57], depending on the tunnel barrier height and the alignment with the Fermi energy (see chapter 1). In the case of an asymmetric coupling, the largest metal-molecule coupling mainly defines the Kondo energy, as the Kondo temperature depends on the sum of the tunnel couplings. Figure 8.4 shows $\mathrm{d}I/\mathrm{d}V$ spectra while moving the tip away from the substrate. Amid the first spectras, just after the tip is attached to the molecule, increasing the tip height increases the Kondo temperature, indicating an increased total tunnel coupling or reduced energy difference between the spin-polarized levels responsible for Kondo correlations and the chemical potential of the electrodes (see chapter 5). After 0.5 Ångstrom of vertical displacement, the width reduces (see figure 8.4 b), and the resonance is fading in the noise. In the meantime, the conductance continuously decreases: the opposite situation is happening in the MCBJ (see figure 7.2), where the FWHM is monotonous, but the conductance at zero-bias jumps most likely due to a reorganization in the electrode's gold crystallographic structure. The associated tensile stress release is not happening in STM, where the Au(111) substrate is highly stable; at the same time, van der Waals interactions are presumably stronger in this configuration than in the MCBJ, locking the molecule on the surface while minimizing its energy by adapting its conformation up to the snapping point. At that point, the current drops to the noise level, and scanning the surface shows the molecule in a slightly shifted position and angle on the substrate (see appendix figure 8.7). Other similarities are observed in the two measurement geometries such as current jumps during IV measurements as displayed in appendix figure 8.8.

8.3.2. DI-RADICAL

We repeat the voltage-pulse procedure on the OH attached to the second fluorene group and take new STS spectra. They now reveal spin-flip steps with an exchange coupling of about 10 mV (see figure 8.3 c). The STS signal above the fluorenyl is similar to the $\mathrm{d}I/\mathrm{d}V$ spectra displayed in figure 4.1 b, with a rounded dip at the bottom and large bias overshoots. This situation corresponds to an asymmetric coupling of the molecule: strongly coupled to the substrate electrode and less strongly coupled to the tip electrode. After taking several long-range spectra, with the tip far away, the molecule moved, and its topography changed slightly; in the STS signal, a double peak centred around zero-bias appears with a zero-bias conductance above the background (see figure 8.2 d). The exchange coupling and the peak height can be slightly varied by changing the position of the tip over the molecule. However, for these non-contact measurements the exchange coupling and Kondo correlations appear to be mainly defined by the molecule-substrate interactions and can only be slightly varied by the tip coupling.

In the MCBJ measurements, the di-radical molecular junction displayed similar inelastic spin-flip signals (inelastic electron tunnelling spectroscopy, IETS) in their $\mathrm{d}I/\mathrm{d}V$ spectra with an exchange coupling of about 14 meV, close to the values observed in

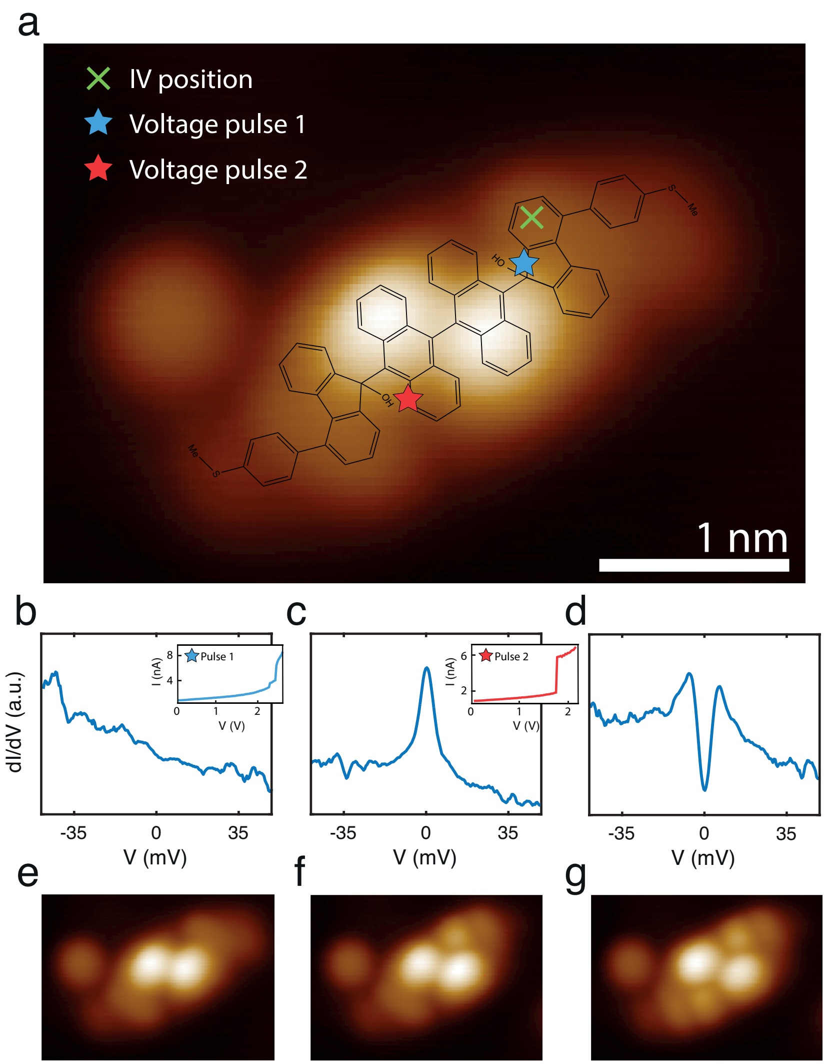

Figure 8.3: On-surface reaction from the closed shell Sme-2CS to the open-shell Sme-2OS di-radical. (a) Topography of a Sme-2CS molecule and (b,c and d) dI/dV spectra taken at the green cross position at each step of the reaction: (b) initial STS signal on a Sme-2CS molecule displaying no features, (c) spectrum after applying a voltage sweep (see inset) above one of the expected OH group position (blue star) showing a zero-bias peak compatible with $S = 1/2$ Kondo and (d) spectrum after repeating the voltage sweep above the second OH group presenting inelastic spin-flip steps with an exchange coupling of about 7 mV. Corresponding topography images (e,f,g) taken at each reaction step with a faint lobe appearing at the position where the OH group has been removed.

bulk [93] Signatures of a ferromagnetic -triplet- ground state have been observed under the application of a magnetic field [76], but significant bias overshoots and absence of resonance at the bottom of the dip also indicated an anti-ferromagnetic, singlet ground state in other junctions. Mechanical manipulation could turn the IETS signal into a zero-bias resonance ascribed to an $S = 1/2$ Kondo physics as displayed in the left pannels of figure 8.5, indicating the change in the total number of unpaired electrons on the molecule from $N = 2$ to $N = 1$. This oxidation may be induced by the proximity of metallic electrodes with the spin-bearing impurities, expelling one of the electrons into the contacts.

A similar transition of the spectra has been observed in the STM measurements as displayed in figure 8.5 b,d. This sequence has been obtained by picking up the molecule from the sulfur atom and lifting it with the tip in the z-direction in small steps (of about $\sim$ 50 pm) while recording the current-bias characteristics at each step. In figure 8.5 a,b the normalized $\mathrm{d}I/\mathrm{d}V$ from the mechanical series are displayed in a color-coded map, revealing a similar transition in both setups from an IETS signal, with an exchange coupling of about 3 meV, into a Kondo resonance. This transition happens in a couple of steps/spectra; it is not straightforward to deduce whether the exchange coupling of the spin-flip signal is reduced before the transition happens or if the background and conductance at the bottom of the dip smear out the side steps.

The main difference between the two mechanical series is better seen in figure 8.5 c and d, where the $\mathrm{d}I/\mathrm{d}V$ spectra are displayed in units of $G_0 = \frac{2e^2}{h}$. In the MCBJ (figure 8.5 c), the different fingerprints are observed at the same conductance, and both the Kondo and the spin-flip signals display a background conductance of about $\sim 10^{-3}$ G_0. In the STM (figure 8.5 d), the signal is dominated by an exponential decay of the conductance with increasing height of the tip. This indicates that direct tunnelling between the tip and the substrate represents an increased fraction of the current measured in the case of STM; this can be due to a larger surface of the two electrodes, as only the tip is atomically sharp in STM, while both electrodes are pointy in the case of an MCBJ experiment.

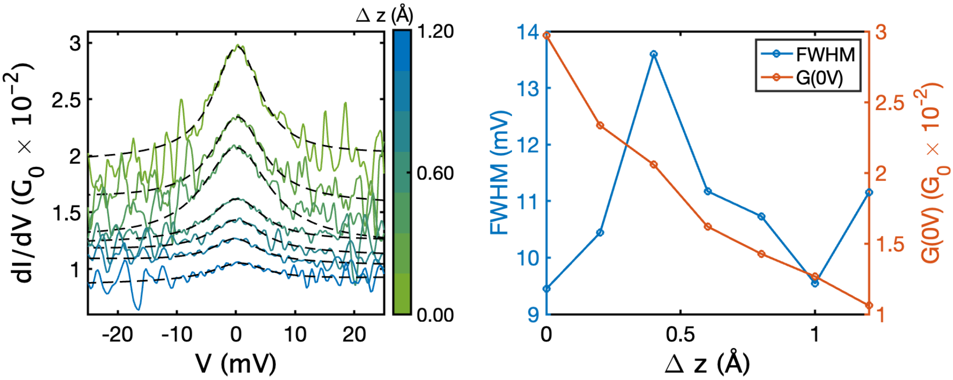

Figure 8.4: (Left) Differential conductance ($\mathrm{d}I/\mathrm{d}V$) as a function of the bias voltage of a Sme-2OS molecular junction in STM at low temperature for increasing tip height (Δz). (Right) Full-width half maximum (FWHM; blue curve) as a function of tip height showing a non-monotonic behavior as a function of Δz, resulting from the Kondo temperature changing with the conformation of the molecule between the substrate and the tip. Differential conductance at zero-bias (red curve) as a function of tip height displaying the high stability of the junction in this geometry and increased direct tunnelling between the tip and the substrate relative to scattering through the quantum transport channel.

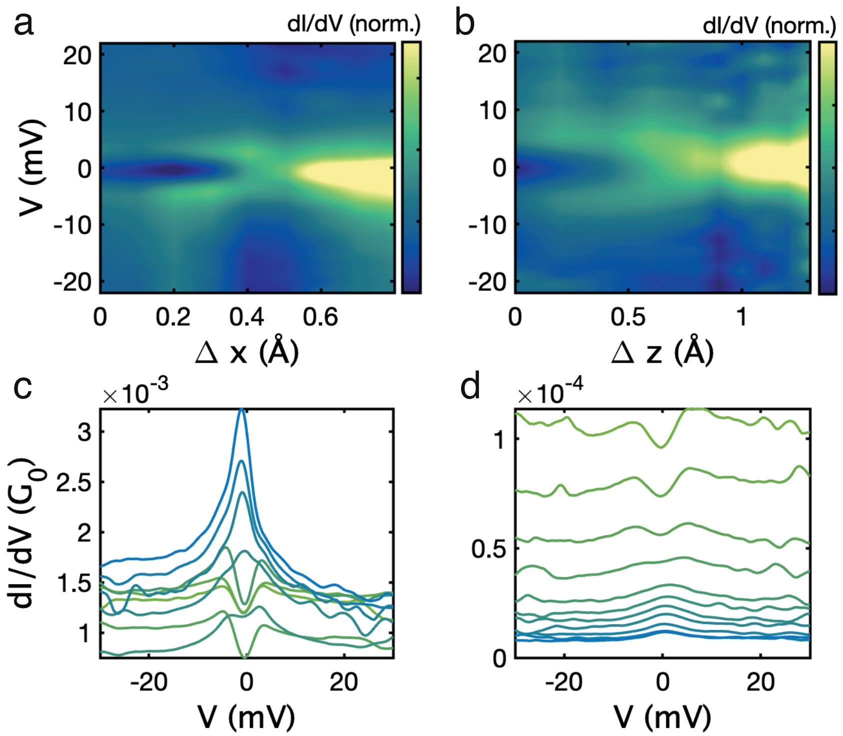

Figure 8.5: Mechanical manipulation of a Sme-2OS molecule (a and c) in MCBJ and (b and d) in STM. The differential conductance, dI/dV, as a function of electrode displacement in MCBJ, Δx, and tip displacement in STM, Δz, and bias voltage applied to the junction are displayed: (c and d) normalized in a color-coded dI/dV map and (e and f) in superposed dI/dV signals in with raw conductance measured in G_0 units. The two mechanical transitions display many similarities: an initial spin-flip signal with an exchange coupling of a few meV turns into a zero-bias resonance after increasing the molecular junction size of a few hundred picometers. The main difference between MCBJ and STM is the overall signal decaying exponentially in STM. In contrast, both the IETS signal and Kondo resonance fingerprints are observed at the same conductance but at different electrode positions in MCBJ.

Thereby, both the molecule conformation and the electrode shapes may change in the MCBJ setup; concurrently, the substrate in STM junctions is highly stable, resulting in fewer changes of the couplings to the molecules during mechanical manipulation.

Contacting the di-radical closer to the radical holding unit in the STM, we observe the opposite transition, from a zero-bias Kondo resonance into an IETS signal with increasing tip height as displayed in appendix figure 8.9. Again, a similar evolution with increasing electrode spacing has been observed with the MCBJ. In the case of the single radical, with a single OH group removed, a zero-bias resonance is measured in the STS spectra independent of the tip-molecule contact position. Based on these observations, it is less likely that the di-radical is oxidized by the tip contacting the molecule, but rather that the interaction between the two radical centers is strongly suppressed, leaving the molecule in a bi-radical state. In this case, the observed spectra correspond to two superposed S=1/2 Kondo resonances measured in a parallel circuit. It is not possible to qualitatively differentiate two superposed S=1/2 Kondo resonances from an oxidized di-radical signal. However, the exchange coupling variation observed among the molecular junction configurations and those exclusively measured in the MCBJ devices support the latter scenario, showing that the exchange coupling can be altered to positive and negative values. It is therefore possible that this exchange coupling take a value close to zero, leaving the di-radical in a bi-radical state.

8.4. CONCLUSION

In this chapter, we investigated molecular junctions based on an all-organic di-radical molecule, the Sme-2OS, using the STM technique and compared the results to those obtained with the MCBJ technique. We produced the open-shell molecule starting from a closed-shell precursor and underlined the similar magnetic fingerprints observed in the differential conductance spectra with purified di-radical measurements in MCBJ. Beyond similar spectra, we also observe similar $\mathrm{d}I/\mathrm{d}V$ sequences along the mechanical manipulation of the open-shell molecule. These results highlight the single-molecule character of molecular junctions formed with the MCBJ technique. By selecting the contacting site between the STM tip and the molecule, we changed the evolution of the mechanical manipulation sequence, headlining the importance of the junction geometry on the di-radical electronic and magnetic properties. The mechanical manipulation exhibited oxidation of the open-shell molecule, demonstrating analogous effects to electrostatic gating.

Comparing the results with measurements of the same molecule in MCBJ, we aimed to reduce the gap between single-molecule studies and integration into functional solid-state devices. The results highlight the improved reproducibility in the STM setup thanks to its ability to manipulate a single molecule in real space and the enhanced stability of the geometry using an Au(111) substrate as an electrode. On the other hand, MCBJ allows the exploration of a more extensive phase space of molecular transport behavior due to the extended variability in the electrode geometry produced during the single-molecule junction formation. The results represent a step toward controlled manipulation of all-organic molecular junctions to tune their properties for potential application. Tailoring the exchange coupling in a di-radical molecule paves the way toward the practical usage of magnetic molecules in spintronic, quantum sensor and quantum computing devices. At the same time, it allows to explore fundamental effects such as Kondo physics and their interplay with other quantum effects like inelastic spin-flip phenomena taking place at the scale of a single molecule.

8.5. APPENDIX

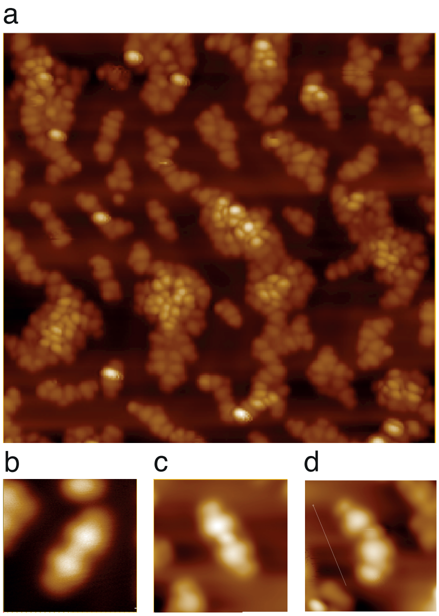

Figure 8.6: (a) STM topography image of molecule chains obtained after deposition of the Sme-2OS di-radical by thermal sublimation. (b, c and d) Some isolated structures reminding of a single molecule shape, however, no magnetic fingerprint is observed in the STS spectra taken over these units. Panel (d) shows the topography of (c) after lateral manipulation.

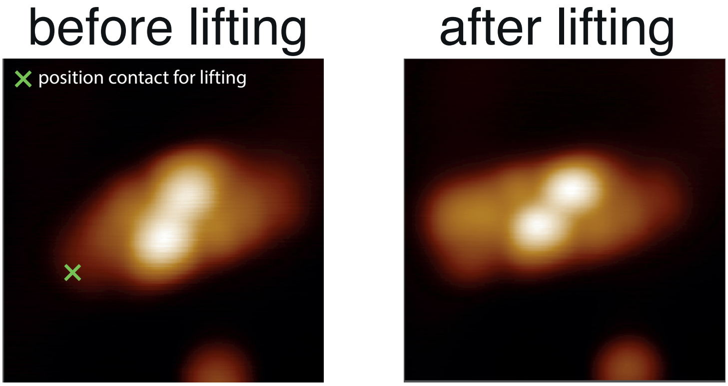

Figure 8.7: STM topography image of a Sme-2OS di-radical molecule (left pannel) before and (right pannel) after the lifting procedure. The tip contacting position is highlighted by the green cross. After lifting manipulation, the topography of the molecule has changed. The spin-flip signal is still visible in the STS spectra taken above the molecule after the lifting procedure.

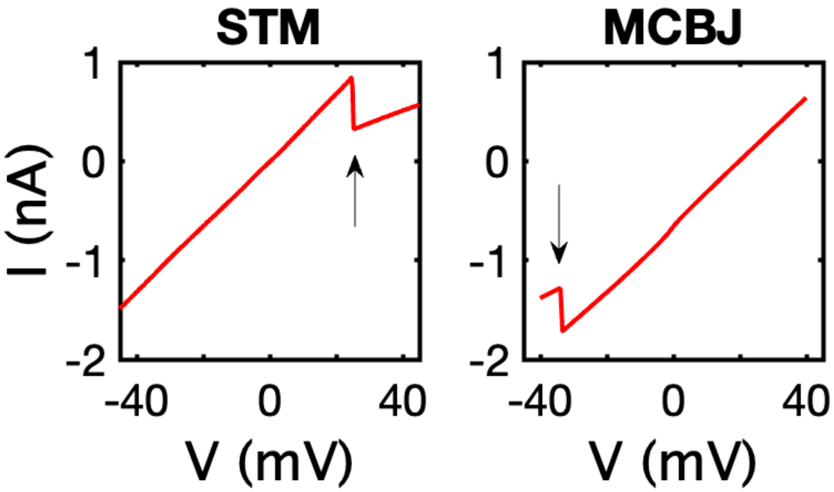

Figure 8.8: Current jump during a bias sweep to record a dI/dV spectrum in a Sme-2OS molecular junction formed in (left panel) the STM setup and with (right pannel) the MCBJ technique.

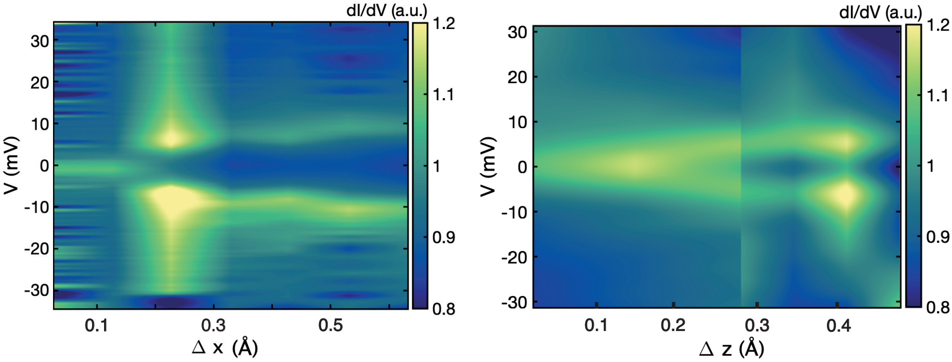

Figure 8.9: Mechanical manipulation of a Sme-2OS molecule (left) in MCBJ and (right) in STM. The differential conductance, dI/dV, as a function of electrode displacement in MCBJ, Δx, tip displacement in STM, Δz. Bias voltage applied to the junction is displayed in a color-coded normalised dI/dV map. The two mechanical sequences display an initial zero-bias resonance turning into an inelastic spin-flip signal with an exchange coupling of a few meV.

9

CONCLUSION AND OUTLOOK

- Sometimes I wonder why we don't put all this ingenuity into serving a noble cause.
- Because it's less fun.
- Oh yeah right.

Orelsan and Gringe, FloBer, Navo and Kyan Khojandi - **Bloqués** - 43: *Projet Chaos*

Optimism is a strategy for making a better future. Because unless you believe that the future can be better, you are unlikely to step up and take responsibility for making it so.

Noam Chomsky

In this chapter we conclude this dissertation by summing up the conclusions from the previous chapters. We also provide a quick outlook on the prospects for the use of all-organic radical molecules in fundamental studies of quantum transport and single-molecule electronics.

9.1. OVERVIEW

In this thesis, we studied charge transport through single-molecule all-organic di-radical molecular junctions. We highlighted a collection of physical phenomena using the same compound backbone throughout the entire study. We investigated the properties of this di-radical embedded in molecular junctions in various conditions. We observed the molecule's signature at room temperature (see chapter 3) and validated the mechanically controllable break junction method as a quick check to detect an organic radical in charge transport experiments. We studied the influence of sulfur-stabilizing groups on molecular junctions formation and transport properties, and measured the closed-shell precursors as a reference.

Investigations at low temperatures in mechanically controlled break junction (chapter 4) allowed us to explore the magnetic fingerprints of the di-radical in diverse conformations and gather an overall picture of the electronic structure of the molecule in different geometries. The spin state of the molecule in the junction has been measured both with indications for $S = 1/2$ and $S = 1$ in the differential conductance spectra of the devices by the observation of a zero-bias Kondo resonance and inelastic spin-flip excitation steps. The exchange coupling between the two electrons has been measured with a ferromagnetic ground state by spin-flip spectroscopy with external magnetic field investigations. Mechanical manipulation has shown transitions from $S = 1/2$ to $S = 1$, highlighting a similar effect as electrostatic gating.

Using three-terminal electromigrated break junction (EMBJ) devices, we investigated molecular junctions formed with the same di-radical with the addition of a gate electrode. We could reversibly reduce and oxidize the charge state of the molecule (chapter 5). The similarity of the signals measured in EMBJ compared to the MCBJ molecular junctions is highlighted. The exchange coupling renormalization due to the proximity of the charge degeneracy point have been observed, and magnetic field measurements highlighted an anti-ferromagnetic coupling in this device.

In the molecular junctions that could be charged but didn't display a signal in the cotunneling (COT) regimes, we investigated the sequential electron tunneling (SET) regime using an external magnetic field and highlighted spin-related excitations (chapter 6). Measuring the shift of the charge degeneracy point with respect to the magnetic field and to the temperature, we attempted to determine the ground state of the molecular junctions using the spin-entropy evolution.

Gathering the previous results, we summarized the different Kondo effects observed in this di-radical in the chapter 7. We checked the $S = 1/2$ evolution of the zero-bias resonances with mechanical manipulation, electrostatic gating, external magnetic field and temperature. Using these methods, we highlight cases beyond the single channel Kondo effect and discuss the intermediate regimes observed and their corresponding fingerprints in the conductance spectras.

Finally, we compared the results obtained with the di-radical in solid-state devices with the ones obtained in a scanning tunnelling microscope setup (chapter 8). Beyond the similarities of the differential conductance spectra, we highlighted similar $\mathrm{d}I/\mathrm{d}V$ sequences during mechanical manipulation of the molecular junction. It is interesting to note that in the two measurement systems, the di-radical was obtained using different paths. In solid-state devices, the open-shell di-radical was directly deposited from solution on top of the device. In STM, the open-shell compound was obtained by successive bias voltage pulses to remove the hydroxyl groups of the precursor. The results confirm the single-molecule character of the molecular junctions measured in solid-state devices and the large influence of the environment on the magnetic properties of all-organic radical molecules.

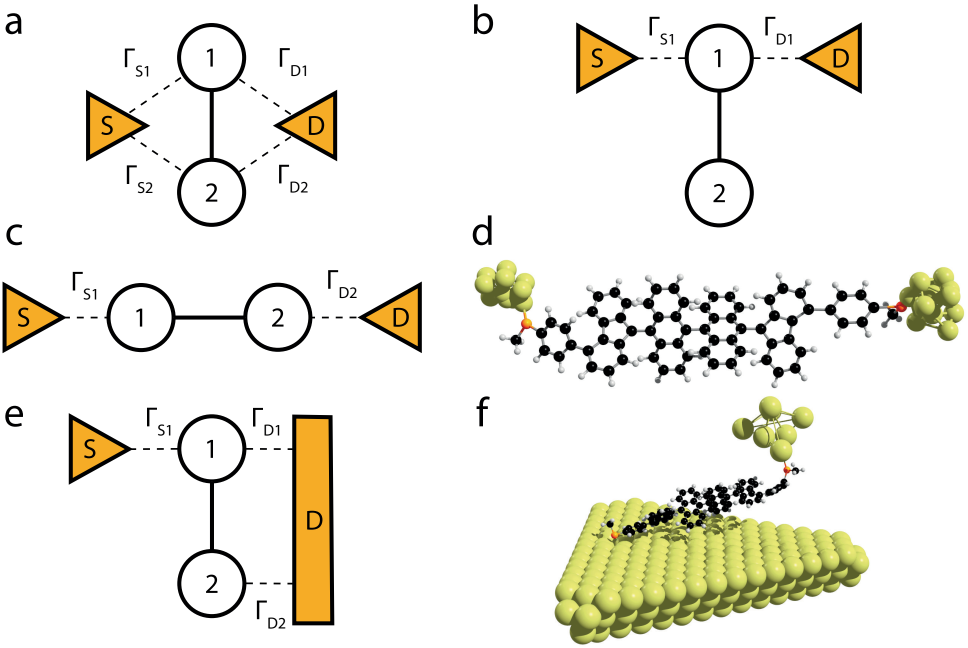

Figure 9.1: (a) Schematic representation of a di-radical molecular junction: two quantum dots (1 and 2) are coupled to each others with an exchange coupling (black solid line) and linked to the circuit through four different tunnel couplings to the source (S) and drain (D) electrodes ($\Gamma_{S1},\Gamma_{D1},\Gamma_{S2},\Gamma_{D2}$). (b) If one of the quantum dot has a stronger coupling to the electrodes than the other the layout is similar to that of a side coupled dot ($\Gamma_{S1},\Gamma_{D1} \gg \Gamma_{S2},\Gamma_{D2}$). (c) If each dot is strongly coupled to a different electrode the layout is that of two serial coupled dots ($\Gamma_{S1},\Gamma_{D2} \gg \Gamma_{S2},\Gamma_{D1}$) similar to a conformation expected in a mechanically controlled break junction (d). (e) If both dots are strongly coupled to the same electrode and only one of them is strongly coupled to the other electrode, the layout is similar to the one displayed in (f), which corresponds to the lifting Scanning tunneling microscope setup ($\Gamma_{D1},\Gamma_{D2} \approx \Gamma_{S1} \gg \Gamma_{S2}$, see chapter 8).

9.2. ALL-ORGANIC POLYCYCLIC AROMATIC HYDROCARBONS POLY-RADICALS

This work highlighted the 2-OS all-organic di-radical as a robust magnetic molecule compatible with the various measurement methods used. The steric hindrance within the molecule protecting the radical centers is a promising road to integrate radicals in solid-state devices while preserving their magnetism. The van der Waals interactions between the 2D carbon lattice of the fluorene and the metallic surface of the electrodes constitute a sturdy interface with a close proximity between the radical center and image charges allowing for strong correlations between the molecular orbitals and the conductions electrons in the gold electrodes.

The high Kondo temperatures observed in the solid-state devices combined with the variable exchange coupling between the spin centers allow to explore a wide phase space of two interacting electrons. Magnetic fingerprints in the cotunneling regime of the $\mathrm{d}I/\mathrm{d}V$ spectra can be used to determine the ground state of the molecule, but other methods can be explored to gather information in the absence of clear cotunneling signals, such as charge degeneracy point shifts with respect to temperature and magnetic field. The possibility to manipulate the molecular junction parameters in a large phase space allow researchers to study exotic regimes such as the singlet-triplet Kondo effect. This makes the all-organic radicals a tool of interest to study physical phenomenon at this scale, and particularly many-body and exotic effects such as the ferromagnetic Kondo effect for example.

The possibility of altering the exchange coupling between the two spin-bearing fluorene moieties by changing the torsional angle between the chemical groups offers the possibility of tuning the system in these different regimes. In particular, considering the series-coupled conformation (see figure 9.1 c,d), a di-radical molecular junction with two Kondo screened channels (9.2 c,d) would be an ideal system to study spin chains. In such a layout, there are four polarised sites in series ($|\mathrm{Source}\rangle$, $|1\rangle$, $|2\rangle$, $|\mathrm{Drain}\rangle$). By adjusting the exchange coupling, we can tune the system to an $S = 1/2$ anti-ferromagnetic spin chain ($|\uparrow\rangle, |\downarrow\rangle, |\uparrow\rangle, |\downarrow\rangle$) or to an $S = 1$ chain ($|\uparrow\rangle, |\downarrow\rangle, |\downarrow\rangle, |\uparrow\rangle$).

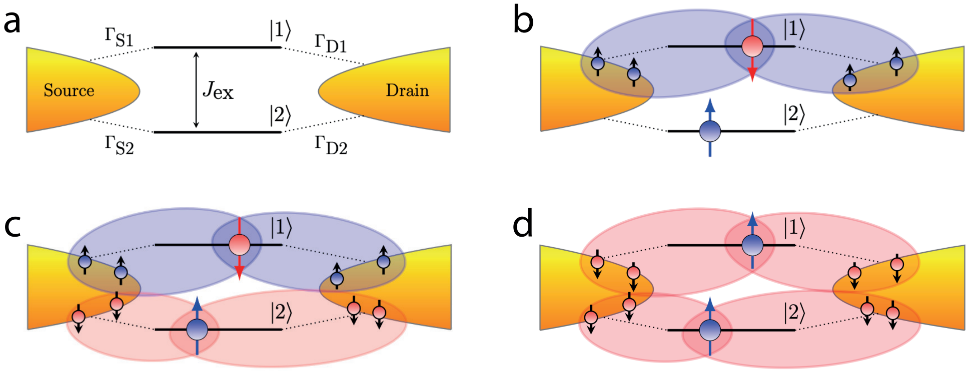

Figure 9.2: (a) Schematic representation of a di-radical molecular junction. (b) Below the Kondo temperature $T_{K1} \propto \Gamma_{S1} + \Gamma_{D1}$, an anti-ferromagnetic exchange coupling arises between the localized electron on the molecular orbital and the conduction electrons in the electrodes generate a polarized Kondo cloud (blue). (c and d) When the temperature is below the Kondo temperatures of both spin-polarized levels, each electron generate its own Kondo cloud. Depending on the exchange coupling between the two molecular orbitals, J_{ex}, the conduction electrons from each Kondo cloud can be polarized in (c) opposite directions ($J_{ex} < 0$) or in (d) the same direction ($J_{ex} > 0$).

9.3. SINGLE-MOLECULE ELECTRONICS

The exploration advantage of single-molecule electronics is counterbalanced as its pitfall: exotic configurations can occur, but the molecule conformation in the junction is stochastic. Couplings are interdependent, and the exact tunnel couplings cannot be controlled precisely. This lack of control is a problem for reproducibility: it is improbable that the same configuration is be obtained twice in the same MCBJ experiment. However, this complication can be avoided by using complementary methods to investigate the same compound and compare the results, such as MCBJ and STM in this thesis.

In the same way, the advantage offered by STM and MCBJ to adjust the couplings is counterbalanced by the lack of control of the charge state. Several experiments in this thesis highlighted a similar effect to electrostatic gating as mechanical manipulation; in some cases, the charge state of the molecule was even found to change by moving the electrodes. In the same way, an electromigrated break junction (EMBJ) offers the possibility to tune this electrostatic environment at the cost of keeping the electrodes fixed and the gap geometry immutable once it has been opened. The greater temperature control of these devices also allows for further characterization of the molecular junction by tuning this extra external parameter.

Molecular junction devices can only be scaled for application purposes by unlocking the ability to precisely control the molecule conformations in the junction. Mechanical manipulation of objects of this dimension cannot be precise as the tunnel coupling varies significantly on the scale of a single metallic atom. Rather than device-based solutions, chemical design can be explored to improve the stability of the contacts, the repeatability of the device characteristics and ultimately a better control of the molecular junctions. By designing metal-molecule interfaces that take advantage of atomically precise synthesis, chemists can engineer radicals with specific transport regimes in mind in order to study exotic phenomena or fulfil a specific task in a logic circuit.Even though this strategy has been implemented in the labs, the mismatch between different disciplines and the long feedback loops involved in taking advantage of such a study has not yet reached this goal. In the same way, chemical design is also a potential direction to tune the exchange coupling in poly-radical molecules robustly and efficiently.

Finally, the tools developed to study single molecule hold promise for diverse research areas. Bendable junctions, in particular, are interesting for exploratory investigations as they allow for strain control while studying the electronic transport properties of a nanostructure. This technique can be applied to study transition metal dichalcogenoids for example. The possibility to engineer electrode spacing on the order of a nanometer opens the potential to study the properties of these materials at a mesoscopic scale. Beyond the potential utility of theses techniques, the molecular electronic catalogue is an ideal tool for students to learn about the complexity of condensed matter at the scale of hundreds to thousands of interacting atoms and the phenomenas emerging from the collective interaction of singular quantum objects.

REFERENCES

[1] R. Brown, *A Brief Account of Microscopical Observations on the Particles Contained in the Pollen of Plants; and on the General Existence of Active Molecules in Organic and Inorganic Bodies*. Richard Taylor, 1828.

[2] J. Perrin, “Mouvement brownien et réalité moléculaire,” in *Annales de Chimie et de Physique*, vol. 18, 1909, pp. 1–114.

[3] L. K. Nash, “The origin of dalton’s chemical atomic theory,” *Isis*, vol. 47, no. 2, pp. 101–116, 1956.

[4] J. C. Maxwell, “V. illustrations of the dynamical theory of gases.—part i. on the motions and collisions of perfectly elastic spheres,” *The London, Edinburgh, and Dublin Philosophical Magazine and Journal of Science*, vol. 19, no. 124, pp. 19–32, 1860.

[5] L. Boltzmann, *Über die Beziehung zwischen dem zweiten Hauptsatze des mechanischen Wärmetheorie und der Wahrscheinlichkeitsrechnung, respective den Sätzen über das Wärmegleichgewicht*. Kk Hof-und Staatsdruckerei, 1877.

[6] L. Boltzmann, “Lectures on gas theory, sg brush,” *Trans. University of California Press: Berkeley, Los Angeles*, vol. 1964, 1896.

[7] J. W. Gibbs, “On the fundamental formula of statistical mechanics, with applications to astronomy and thermodynamics,” in *Proceedings of the American Association for the Advancement of Science*, 1884, pp. 57–58.

[8] J. J. Thomson, “Xl. cathode rays,” *The London, Edinburgh, and Dublin Philosophical Magazine and Journal of Science*, vol. 44, no. 269, pp. 293–316, 1897.

[9] P. Drude, “Zur elektronentheorie der metalle,” *Annalen der Physik*, vol. 306, no. 3, pp. 566–613, 1900.

[10] G. S. Ohm, *Die galvanische kette: mathematisch*. TH Riemann, 1827.

[11] H. A. Lorentz, *The theory of electrons and its applications to the phenomena of light and radiant heat*. GE Stechert & Company, 1916, vol. 29.

[12] A. Sommerfeld, “Zur Elektronentheorie der Metalle auf Grund der Fermischen Statistik,” *Zeitschrift fur Physik*, vol. 47, no. 1-2, pp. 1–32, Jan. 1928.

[13] G. Kirchhoff and R. Bunsen, “Chemische analyse durch spectralbeobachtungen,” *Annalen der Physik*, vol. 186, no. 6, pp. 161–189, 1860.

[14] M. Planck, “The theory of heat radiation,” *Entropie*, vol. 144, no. 190, p. 164, 1900.

[15] A. Einstein, “Einstein’s proposal of the photon conceptfia translation of the annalen der physik paper of 1905,” *Ann. Physik*, vol. 17, p. 132, 1905.

[16] N. Bohr, "On the constitution of atoms and molecules," in *Niels Bohr, 1913-2013: Poincaré Seminar 2013*, Springer, 2016, pp. 13–33.

[17] A. Einstein, "7 on the quantum theory of radiation," *The Old Quantum Theory: The Commonwealth and International Library: Selected Readings in Physics*, p. 167, 2016.

[18] L. de Broglie, "Research on the theory of quanta," in *Annales de Physique*, vol. 10, 1925, pp. 22–128.

[19] E. Schrödinger, "An undulatory theory of the mechanics of atoms and molecules," *Physical review*, vol. 28, no. 6, p. 1049, 1926.

[20] E. Fermi, "Sulla quantizzazione del gas perfetto monoatomico," *Rendiconti Lincei*, vol. 145, 1926.

[21] S. N. Bose, "Planck's law and the hypothesis of light quanta," *Z. Phys*, vol. 26, no. 178, pp. 1–5, 1924.

[22] Bose, "Plancks gesetz und lichtquantenhypothese," *Zeitschrift für Physik*, vol. 26, no. 1, pp. 178–181, Dec. 1924.

[23] W. Gerlach and O. Stern, "Der experimentelle nachweis der richtungsquantelung im magnetfeld," *Zeitschrift für Physik*, vol. 9, no. 1, pp. 349–352, Dec. 1922.

[24] A. Hirohata *et al.*, "Review on spintronics: Principles and device applications," *Journal of Magnetism and Magnetic Materials*, vol. 509, p. 166 711, 2020.

[25] I. Yuri, "Manin. vychislimoe i nevychislimoe," *Sov. Radio*, p. 1, 1980.

[26] R. P. Feynman, "Simulating physics with computers," *International Journal of Theoretical Physics*, vol. 21, no. 6, pp. 467–488, Jun. 1982.

[27] P. Benioff, "The computer as a physical system: A microscopic quantum mechanical hamiltonian model of computers as represented by turing machines," *Journal of Statistical Physics*, vol. 22, no. 5, pp. 563–591, May 1980.

[28] J. J. Pla *et al.*, "A single-atom electron spin qubit in silicon," *Nature*, vol. 489, no. 7417, pp. 541–545, Sep. 2012.

[29] D. J. Reilly, "Engineering the quantum-classical interface of solid-state qubits," *npj Quantum Information*, vol. 1, no. 1, p. 15 011, Oct. 2015.

[30] D. M. Hudgins, J. Charles W. Bauschlicher, and L. J. Allamandola, "Variations in the peak position of the 6.2 mum interstellar emission feature: A tracer of n in the interstellar polycyclic aromatic hydrocarbon population," *The Astrophysical Journal*, vol. 632, no. 1, p. 316, Oct. 2005.

[31] K. Kaiser *et al.*, "Visualization and identification of single meteoritic organic molecules by atomic force microscopy," *Meteoritics & Planetary Science*, vol. 57, no. 3, pp. 644–656, 2022.

[32] A. Li, "Pahs in comets: An overview," in *Deep Impact as a World Observatory Event: Synergies in Space, Time, and Wavelength*, H. Käufl and C. Sterken, Eds., Berlin, Heidelberg: Springer Berlin Heidelberg, 2009, pp. 161–175.

[33] K. A. Kipfer *et al.*, “Toward detecting polycyclic aromatic hydrocarbons on planetary objects with origin,” *The Planetary Science Journal*, vol. 3, no. 2, p. 43, Feb. 2022.

[34] D. A. García-Hernández *et al.*, “Formation of fullerenes in h-containing planetary nebulae,” *The Astrophysical Journal Letters*, vol. 724, no. 1, p. L39, Oct. 2010.

[35] D. S. Parker *et al.*, “Low temperature formation of naphthalene and its role in the synthesis of pahs (polycyclic aromatic hydrocarbons) in the interstellar medium,” *Proceedings of the National Academy of Sciences*, vol. 109, no. 1, pp. 53–58, 2012.

[36] P. Ehrenfreund, S. Rasmussen, J. Cleaves, and L. Chen, “Experimentally tracing the key steps in the origin of life: The aromatic world,” *Astrobiology*, vol. 6, no. 3, pp. 490–520, 2006, PMID: 16805704.

[37] R. Wiltschko, C. Nießner, and W. Wiltschko, “The magnetic compass of birds: The role of cryptochrome,” *Frontiers in Physiology*, vol. 12, 2021.

[38] T. Ritz, P. Thalau, J. B. Phillips, R. Wiltschko, and W. Wiltschko, “Resonance effects indicate a radical-pair mechanism for avian magnetic compass,” *Nature*, vol. 429, no. 6988, pp. 177–180, May 2004.

[39] J. Nall and J. Lathrop, “Photolithographic fabrication techniques for transistors which are an integral part of a printed circuit,” in *1957 International Electron Devices Meeting*, IEEE, 1957, pp. 117–117.

[40] R. Young, J. Ward, and F. Scire, “The topografiner: An instrument for measuring surface microtopography,” *Review of Scientific Instruments*, vol. 43, no. 7, pp. 999–1011, 1972.

[41] G. Binnig and H. Rohrer, “Scanning tunneling microscopy,” *Surface science*, vol. 126, no. 1-3, pp. 236–244, 1983.

[42] C. Joachim, J. K. Gimzewski, R. R. Schlittler, and C. Chavy, “Electronic transparence of a single C_{60} molecule,” *Phys. Rev. Lett.*, vol. 74, pp. 2102–2105, 11 Mar. 1995.

[43] L. A. Bumm *et al.*, “Are single molecular wires conducting?” *Science*, vol. 271, no. 5256, pp. 1705–1707, 1996.

[44] A. R. Champagne, A. N. Pasupathy, and D. C. Ralph, “Mechanically adjustable and electrically gated single-molecule transistors,” *Nano Letters*, vol. 5, no. 2, pp. 305–308, 2005, PMID: 15794616.

[45] A. R. Von Hippel and R. Landshoff, “Molecular Science and Molecular Engineering,” *Physics Today*, vol. 12, no. 10, pp. 48–48, Oct. 1959.

[46] A. Aviram and M. A. Ratner, “Molecular rectifiers,” *Chemical Physics Letters*, vol. 29, no. 2, pp. 277–283, 1974.

[47] A. Aviram, “Molecules for memory, logic, and amplification,” *Journal of the American Chemical Society*, vol. 110, no. 17, pp. 5687–5692, 1988.

[48] D. C. Magri, “A fluorescent and logic gate driven by electrons and protons,” *New J. Chem.*, vol. 33, pp. 457–461, 3 2009.

[49] P. A. de Silva, N. H. Q. Gunaratne, and C. P. McCoy, “A molecular photoionic and gate based on fluorescent signalling,” *Nature*, vol. 364, no. 6432, pp. 42–44, Jul. 1993.

[50] D. Parker, “Taking advantage of the ph and po2 sensitivity of a luminescent macrocyclic terbium phenanthridyl complex,” *Chem. Commun.*, pp. 245–246, 2 1998.

[51] B. Turfan and E. U. Akkaya, “Modulation of boradiazaindacene emission by cation-mediated oxidative pet,” *Organic Letters*, vol. 4, no. 17, pp. 2857–2859, 2002, PMID: 12182573.

[52] A. Prasanna de Silva and N. D. McClenaghan, “Proof-of-principle of molecular-scale arithmetic,” *Journal of the American Chemical Society*, vol. 122, no. 16, pp. 3965–3966, 2000.

[53] J. G. Simmons, “Generalized Formula for the Electric Tunnel Effect between Similar Electrodes Separated by a Thin Insulating Film,” *Journal of Applied Physics*, vol. 34, no. 6, pp. 1793–1803, Jun. 2004.

[54] S. Florens *et al.*, “Universal transport signatures in two-electron molecular quantum dots: Gate-tunable hund’s rule, underscreened kondo effect and quantum phase transitions,” *Journal of Physics: Condensed Matter*, vol. 23, no. 24, p. 243 202, May 2011.

[55] R. Gaudenzi, M. Misiorny, E. Burzurí, M. R. Wegewijs, and H. S. J. van der Zant, “Transport mirages in single-molecule devices,” *The Journal of Chemical Physics*, vol. 146, no. 9, p. 092 330, Feb. 2017.

[56] J. Kondo, “Resistance Minimum in Dilute Magnetic Alloys,” *Progress of Theoretical Physics*, vol. 32, no. 1, pp. 37–49, Jul. 1964.

[57] G. D. Scott and D. Natelson, “Kondo resonances in molecular devices,” *ACS Nano*, vol. 4, no. 7, pp. 3560–3579, 2010, PMID: 20568709.

[58] S. Naghibi *et al.*, “Redox-addressable single-molecule junctions incorporating a persistent organic radical**,” *Angewandte Chemie International Edition*, vol. 61, no. 23, e202116985, 2022.

[59] J. Liu *et al.*, “Radical-enhanced charge transport in single-molecule phenothiazine electrical junctions,” *Angewandte Chemie International Edition*, vol. 56, no. 42, pp. 13 061–13 065, 2017.

[60] J. A. De Sousa *et al.*, “Stable organic radical for enhancing metal–monolayer–semiconductor junction performance,” *ACS Applied Materials & Interfaces*, vol. 15, no. 3, pp. 4635–4642, 2023, PMID: 36642951.

[61] G.-C. Hu, Z. Zhang, Y. Li, J.-F. Ren, and C.-K. Wang, “Length dependence of rectification in organic co-oligomer spin rectifiers*,” *Chinese Physics B*, vol. 25, no. 5, p. 057 308, Apr. 2016.

[62] M. R. S. Siqueira, S. M. Corrêa, R. M. Gester, J. Del Nero, and A. M. J. C. Neto, “Single-molecular diodes based on opioid derivatives,” *Journal of Molecular Modeling*, vol. 21, no. 12, p. 317, Nov. 2015.

[63] J. Barbosa *et al.*, "Molecular design of functional polymers for organic radical batteries," *Energy Storage Materials*, vol. 60, p. 102 841, 2023.

[64] E. Schröter, C. Stolze, A. Saal, K. Schreyer, M. D. Hager, and U. S. Schubert, "All-organic redox targeting with a single redox moiety: Combining organic radical batteries and organic redox flow batteries," *ACS Applied Materials & Interfaces*, vol. 14, no. 5, pp. 6638–6648, 2022, PMID: 35084188.

[65] H. Nishide and T. Suga, "Organic radical battery," *The Electrochemical Society Interface*, vol. 14, no. 4, p. 32, Dec. 2005.

[66] P. Li, C. Jia, and X. Guo, "Molecule-based transistors: From macroscale to single molecule.," *The Chemical Record*, vol. 21, no. 6, pp. 1284–1299, 2021.

[67] Y. Li, C. Yang, and X. Guo, "Single-molecule electrical detection: A promising route toward the fundamental limits of chemistry and life science," *Accounts of Chemical Research*, vol. 53, no. 1, pp. 159–169, 2020, PMID: 31545589.

[68] L. Meng *et al.*, "Dual-gated single-molecule field-effect transistors beyond moore's law," *Nature Communications*, vol. 13, no. 1, p. 1410, Mar. 2022.

[69] Q. Zheng *et al.*, "Ultra-stable organic fluorophores for single-molecule research," *Chemical Society Reviews*, vol. 43, no. 4, pp. 1044–1056, 2014.

[70] A. Abdurahman *et al.*, "Understanding the luminescent nature of organic radicals for efficient doublet emitters and pure-red light-emitting diodes," *Nature Materials*, vol. 19, no. 11, pp. 1224–1229, Nov. 2020.

[71] X. Li, Y.-L. Wang, C. Chen, Y.-Y. Ren, and Y.-F. Han, "A platform for blue-luminescent carbon-centered radicals," *Nature Communications*, vol. 13, no. 1, p. 5367, Sep. 2022.

[72] X.-H. Cao *et al.*, "Controllable anisotropic thermoelectric properties in 2D covalent organic radical frameworks," *Applied Physics Letters*, vol. 119, no. 26, p. 263 901, Dec. 2021.

[73] E. P. Tomlinson, S. Mukherjee, and B. W. Boudouris, "Enhancing polymer thermoelectric performance using radical dopants," *Organic Electronics*, vol. 51, pp. 243–248, 2017.

[74] S. Sangtarash and H. Sadeghi, "Radical enhancement of molecular thermoelectric efficiency," *Nanoscale Advances*, vol. 2, no. 3, pp. 1031–1035, 2020.

[75] X. Zhang *et al.*, "Synthesis of extended polycyclic aromatic hydrocarbons by oxidative tandem spirocyclization and 1,2-aryl migration," *Nature Communications*, vol. 8, no. 1, p. 15 073, Apr. 2017.

[76] T. Y. Baum, S. Fernández, D. Peña, and H. S. J. van der Zant, "Magnetic fingerprints in an all-organic radical molecular break junction," *Nano Letters*, vol. 22, no. 20, pp. 8086–8092, 2022.

[77] F. van Veen, L. Ornago, H. S. van der Zant, and M. El Abbassi, "A generalized neural network approach for separation of molecular breaking traces," *Journal of Materials Chemistry C*, 2023.

[78] D. Cabosart *et al.*, “A reference-free clustering method for the analysis of molecular break-junction measurements,” *Applied Physics Letters*, vol. 114, no. 14, p. 143 102, Apr. 2019.

[79] N. Pavliček *et al.*, “Synthesis and characterization of triangulene,” *Nature Nanotechnology*, vol. 12, no. 4, pp. 308–311, Apr. 2017.

[80] Z. Chen, A. Narita, and K. Müllen, “Graphene nanoribbons: On-surface synthesis and integration into electronic devices,” *Advanced Materials*, vol. 32, no. 45, p. 2 001 893, 2020.

[81] Y.-h. Zhang *et al.*, “Temperature and magnetic field dependence of a kondo system in the weak coupling regime,” *Nature Communications*, vol. 4, no. 1, p. 2110, Jul. 2013.

[82] R. Frisenda *et al.*, “Kondo effect in a neutral and stable all organic radical single molecule break junction,” *Nano Letters*, vol. 15, no. 5, pp. 3109–3114, May 2015.

[83] L. H. Yu and D. Natelson, “The kondo effect in c60 single-molecule transistors,” *Nano Letters*, vol. 4, no. 1, pp. 79–83, 2004.

[84] J. Liu *et al.*, “First observation of a kondo resonance for a stable neutral pure organic radical, 1, 3, 5-triphenyl-6-oxoverdazyl, adsorbed on the au (111) surface,” *Journal of the American Chemical Society*, vol. 135, no. 2, pp. 651–658, 2013.

[85] S. Mullegger, M. Rashidi, M. Fattinger, and R. Koch, “Surface-supported hydrocarbon π radicals show kondo behavior,” *The Journal of Physical Chemistry C*, vol. 117, no. 11, pp. 5718–5721, 2013.

[86] R. Hayakawa *et al.*, “Large magnetoresistance in single-radical molecular junctions,” *Nano letters*, vol. 16, no. 8, pp. 4960–4967, 2016.

[87] B. Warner *et al.*, “Tunable magnetoresistance in an asymmetrically coupled single-molecule junction,” *Nature nanotechnology*, vol. 10, no. 3, pp. 259–263, 2015.

[88] R. Gaudenzi *et al.*, “Redox-induced gating of the exchange interactions in a single organic diradical,” *ACS nano*, vol. 11, no. 6, pp. 5879–5883, 2017.

[89] X. Chen *et al.*, “Probing superexchange interaction in molecular magnets by spin-flip spectroscopy and microscopy,” *Phys. Rev. Lett.*, vol. 101, p. 197 208, 19 Nov. 2008.

[90] S. Mishra *et al.*, “Collective all-carbon magnetism in triangulene dimers**,” *Angewandte Chemie International Edition*, vol. 59, no. 29, pp. 12 041–12 047, 2020.

[91] S. Mishra *et al.*, “Large magnetic exchange coupling in rhombus-shaped nanographenes with zigzag periphery,” *Nature Chemistry*, vol. 13, no. 6, pp. 581–586, 2021.

[92] R. Gaudenzi *et al.*, “Exchange coupling inversion in a high-spin organic triradical molecule,” *Nano Letters*, vol. 16, no. 3, pp. 2066–2071, Mar. 2016.

[93] Z. Zeng *et al.*, “Stable tetrabenzo-chichibabin’s hydrocarbons: Tunable ground state and unusual transition between their closed-shell and open-shell resonance forms,” *Journal of the American Chemical Society*, vol. 134, no. 35, pp. 14 513–14 525, 2012, PMID: 22889277.

[94] R. Poli, “Radical Coordination Chemistry and Its Relevance to MetalMediated Radical Polymerization,” *European Journal of Inorganic Chemistry*, vol. 2011, no. 10, p. 1513,

[95] M. Ternes, “Spin excitations and correlations in scanning tunneling spectroscopy,” *New Journal of Physics*, vol. 17, no. 6, p. 063 016, Jun. 2015.

[96] J. Park *et al.*, “Coulomb blockade and the kondo effect in single-atom transistors,” *Nature*, vol. 417, no. 6890, pp. 722–725, Jun. 2002.

[97] G. D. Scott, Z. K. Keane, J. W. Ciszek, J. M. Tour, and D. Natelson, “Universal scaling of nonequilibrium transport in the kondo regime of single molecule devices,” *Phys. Rev. B*, vol. 79, p. 165 413, 16 Apr. 2009.

[98] J. J. Parks *et al.*, “Mechanical control of spin states in spin-1 molecules and the underscreened kondo effect,” *Science*, vol. 328, no. 5984, pp. 1370–1373, 2010.

[99] T. A. Costi, “Kondo effect in a magnetic field and the magnetoresistivity of kondo alloys,” *Phys. Rev. Lett.*, vol. 85, pp. 1504–1507, 7 Aug. 2000.

[100] Y. Meir, N. S. Wingreen, and P. A. Lee, “Low-temperature transport through a quantum dot: The anderson model out of equilibrium,” *Phys. Rev. Lett.*, vol. 70, pp. 2601–2604, 17 Apr. 1993.

[101] L. Venkataraman, J. E. Klare, C. Nuckolls, M. S. Hybertsen, and M. L. Steigerwald, “Dependence of single-molecule junction conductance on molecular conformation,” *Nature*, vol. 442, no. 7105, pp. 904–907, Aug. 2006.

[102] M. Ormaza *et al.*, “Efficient spin-flip excitation of a nickelocene molecule,” *Nano Letters*, vol. 17, no. 3, pp. 1877–1882, Mar. 2017.

[103] M.-H. Jo *et al.*, “Signatures of molecular magnetism in single-molecule transport spectroscopy,” *Nano Letters*, vol. 6, no. 9, pp. 2014–2020, Sep. 2006.

[104] S. Mishra *et al.*, “Observation of fractional edge excitations in nanographene spin chains,” *Nature*, vol. 598, no. 7880, pp. 287–292, Oct. 2021.

[105] P. Jelínek, “Quantum spin chains go organic,” *Nature Chemistry*, vol. 15, no. 1, pp. 12–13, Jan. 2023.

[106] L. Guo, X. Gu, X. Zhu, and X. Sun, “Recent advances in molecular spintronics: Multifunctional spintronic devices,” *Advanced Materials*, vol. 31, no. 45, p. 1 805 355, 2019.

[107] J. Guasch *et al.*, “Two-dimensional self-assembly and electrical properties of the donor-acceptor tetrathiafulvalene-polychlorotriphenylmethyl radical on graphite substrates,” *Journal of Applied Physics*, vol. 125, no. 14, p. 142 909, Apr. 2019.

[108] J. Liu, J. Kang, and Y. Wang, “Molecular discovery of half-metallic one-dimensional metal-organic framework,” *Journal of Applied Physics*, vol. 125, no. 14, p. 142 906, Mar. 2019.

[109] M. Gobbi, M. A. Novak, and E. Del Barco, “Molecular spintronics,” *Journal of Applied Physics*, vol. 125, no. 24, p. 240 401, Jun. 2019.

[110] A. E. Tschitschibabin, “Über einige phenylierte derivate des p, p-ditolyls,” *Berichte der deutschen chemischen Gesellschaft*, vol. 40, no. 2, pp. 1810–1819, 1907.

[111] R. Hicks, *Stable radicals: fundamentals and applied aspects of odd-electron compounds*. John Wiley & Sons, 2011.

[112] J. Li *et al.*, “Uncovering the triplet ground state of triangular graphene nanoflakes engineered with atomic precision on a metal surface,” *Phys. Rev. Lett.*, vol. 124, p. 177 201, 17 Apr. 2020.

[113] N. Pavliček *et al.*, “Synthesis and characterization of triangulene,” *Nature Nanotechnology*, vol. 12, no. 4, pp. 308–311, Feb. 2017.

[114] C. Sánchez-Sánchez *et al.*, “On-surface hydrogen-induced covalent coupling of polycyclic aromatic hydrocarbons via a superhydrogenated intermediate,” *Journal of the American Chemical Society*, vol. 141, no. 8, pp. 3550–3557, 2019.

[115] S. Mishra *et al.*, *Bistability between π-diradical open-shell and closed-shell states in indeno[1,2-a]fluorene*, 2023.

[116] R. Kawaguchi, K. Hashimoto, T. Kakudate, K. Katoh, M. Yamashita, and T. Komeda, “Spatially resolving electron spin resonance of pi-radical in single-molecule magnet,” *Nano Letters*, vol. 23, no. 1, pp. 213–219, 2023, PMID: 36585948.

[117] L. Sellies, R. Spachtholz, P. Scheuerer, and J. Repp, *Atomic-scale access to long spin coherence in single molecules with scanning force microscopy*, 2023.

[118] M. Koole, J. C. Hummelen, and H. S. J. van der Zant, “Spin excitations in an all-organic double quantum dot molecule,” *Phys. Rev. B*, vol. 94, p. 165 414, 16 Oct. 2016.

[119] J. M. Thijssen and H. S. Van der Zant, “Charge transport and single-electron effects in nanoscale systems,” *physica status solidi (b)*, vol. 245, no. 8, pp. 1455–1470, 2008.

[120] H. S. J. van der Zant *et al.*, “Molecular three-terminal devices: Fabrication and measurements,” *Faraday Discuss.*, vol. 131, pp. 347–356, 0 2006.

[121] S. Guo, J. Hihath, and N. Tao, “Breakdown of atomic-sized metallic contacts measured on nanosecond scale,” *Nano Letters*, vol. 11, no. 3, pp. 927–933, 2011, PMID: 21294524.

[122] V. S. Zharinov, X. D. A. Baumans, A. V. Silhanek, E. Janssens, and J. Van de Vondel, “Controlled electromigration protocol revised,” *Review of Scientific Instruments*, vol. 89, no. 4, p. 043 904, Apr. 2018.

[123] F. Hadeed and C. Durkan, “Controlled fabrication of 1-2 nm nanogaps by electromigration in au and au/pd nanowires,” *Applied Physics Letters*, vol. 91, pp. 123 120–123 120, Sep. 2007.

[124] V. Dubois *et al.*, “Massively parallel fabrication of crack-defined gold break junctions featuring sub-3nm gaps for molecular devices,” *Nature Communications*, vol. 9, no. 1, pp. 1–10, Aug. 2018.

[125] M. Mannini *et al.*, “Magnetic memory of a single-molecule quantum magnet wired to a gold surface,” *Nature Materials*, vol. 8, no. 3, pp. 194–197, Mar. 2009.

[126] E. A. Weiss, M. J. Ahrens, L. E. Sinks, A. V. Gusev, M. A. Ratner, and M. R. Wasielewski, "Making a molecular wire: Charge and spin transport through para-phenylene oligomers," *Journal of the American Chemical Society*, vol. 126, no. 17, pp. 5577–5584, 2004, PMID: 15113229.

[127] J. O. Thomas *et al.*, "Understanding resonant charge transport through weakly coupled single-molecule junctions," *Nature Communications*, vol. 10, no. 1, p. 4628, Oct. 2019.

[128] M. Ganzhorn, S. Klyatskaya, M. Ruben, and W. Wernsdorfer, "Strong spin–phonon coupling between a single-molecule magnet and a carbon nanotube nanoelectromechanical system," *Nature Nanotechnology*, vol. 8, no. 3, pp. 165–169, Mar. 2013.

[129] N. Hartman *et al.*, "Direct entropy measurement in a mesoscopic quantum system," *Nature Physics*, vol. 14, no. 11, pp. 1083–1086, Nov. 2018.

[130] P. Gehring *et al.*, "Complete mapping of the thermoelectric properties of a single molecule," *Nature Nanotechnology*, vol. 16, no. 4, pp. 426–430, Apr. 2021.

[131] M. Gomberg, "An instance of trivalent carbon: Triphenylmethyl.," *Journal of the American Chemical Society*, vol. 22, no. 11, pp. 757–771, 1900.

[132] W. Schlenk and M. Brauns, "Zur frage der metachinoide," *Berichte der deutschen chemischen Gesellschaft*, vol. 48, no. 1, pp. 661–669, 1915.

[133] M. Noori, H. Sadeghi, and C. J. Lambert, "Stable-radicals increase the conductance and seebeck coefficient of graphene nanoconstrictions," *Nanoscale*, vol. 10, pp. 19 220–19 223, 40 2018.

[134] S. M. Cronenwett, T. H. Oosterkamp, and L. P. Kouwenhoven, "A tunable kondo effect in quantum dots," *Science*, vol. 281, no. 5376, pp. 540–544, 1998.

[135] H. Jeong, A. M. Chang, and M. R. Melloch, "The kondo effect in an artificial quantum dot molecule," *Science*, vol. 293, no. 5538, pp. 2221–2223, 2001.

[136] W. G. van der Wiel *et al.*, "Two-stage kondo effect in a quantum dot at a high magnetic field," *Phys. Rev. Lett.*, vol. 88, p. 126 803, 12 Mar. 2002.

[137] A. Spinelli, M. Gerrits, R. Toskovic, B. Bryant, M. Ternes, and A. F. Otte, "Exploring the phase diagram of the two-impurity kondo problem," *Nature Communications*, vol. 6, no. 1, p. 10 046, Nov. 2015.

[138] A. F. Otte *et al.*, "The role of magnetic anisotropy in the kondo effect," *Nature Physics*, vol. 4, no. 11, pp. 847–850, Nov. 2008.

[139] V. Madhavan, W. Chen, T. Jamneala, M. F. Crommie, and N. S. Wingreen, "Tunneling into a single magnetic atom: Spectroscopic evidence of the kondo resonance," *Science*, vol. 280, no. 5363, pp. 567–569, 1998.

[140] A. Makarovski, A. Zhukov, J. Liu, and G. Finkelstein, "Su(2) and su(4) kondo effects in carbon nanotube quantum dots," *Phys. Rev. B*, vol. 75, p. 241 407, 24 Jun. 2007.

[141] N. Friedrich *et al.*, "Addressing electron spins embedded in metallic graphene nanoribbons," *ACS Nano*, vol. 16, no. 9, pp. 14 819–14 826, 2022, PMID: 36037149.

[142] T. Wang *et al.*, "Aza-triangulene: On-surface synthesis and electronic and magnetic properties," *Journal of the American Chemical Society*, vol. 144, no. 10, pp. 4522–4529, 2022, PMID: 35254059.

[143] V. Iancu, A. Deshpande, and S.-W. Hla, "Manipulating kondo temperature via single molecule switching," *Nano Letters*, vol. 6, no. 4, pp. 820–823, 2006, PMID: 16608290.

[144] G. Mitra *et al.*, "Interplay between magnetoresistance and kondo resonance in radical single-molecule junctions," *Nano Letters*, vol. 22, no. 14, pp. 5773–5779, 2022, PMID: 35849010.

[145] A. Vegliante *et al.*, "Tuning the spin interaction in non-planar organic diradicals through mechanical manipulation," 2024.

[146] F. D. M. Haldane, "Scaling theory of the asymmetric anderson model," *Phys. Rev. Lett.*, vol. 40, pp. 416–419, 6 Feb. 1978.

[147] T. A. Costi, "Kondo effect in a magnetic field and the magnetoresistivity of kondo alloys," *Phys. Rev. Lett.*, vol. 85, pp. 1504–1507, 7 Sep. 2000.

[148] N. Roch, S. Florens, T. A. Costi, W. Wernsdorfer, and F. Balestro, "Observation of the underscreened kondo effect in a molecular transistor," *Phys. Rev. Lett.*, vol. 103, p. 197 202, 19 Nov. 2009.

[149] D. Goldhaber-Gordon, J. Göres, M. A. Kastner, H. Shtrikman, D. Mahalu, and U. Meirav, "From the kondo regime to the mixed-valence regime in a single-electron transistor," *Phys. Rev. Lett.*, vol. 81, pp. 5225–5228, 23 Dec. 1998.

[150] P. S. Cornaglia, G. Usaj, and C. A. Balseiro, "Electronic transport through magnetic molecules with soft vibrating modes," *Phys. Rev. B*, vol. 76, p. 241 403, 24 Dec. 2007.

[151] P. S. Cornaglia and D. R. Grempel, "Magnetoconductance through a vibrating molecule in the kondo regime," *Phys. Rev. B*, vol. 71, p. 245 326, 24 Jun. 2005.

[152] M. Pustilnik and L. I. Glazman, "Kondo effect in real quantum dots," *Phys. Rev. Lett.*, vol. 87, p. 216 601, 21 Nov. 2001.

[153] H. Heersche *et al.*, "Kondo effect in the presence of magnetic impurities," *Physical review letters*, vol. 96, p. 017 205, Feb. 2006.

[154] P. Zalom, J. de Bruijckere, R. Gaudenzi, H. S. J. van der Zant, T. Novotný, and R. Korytár, "Magnetically tuned kondo effect in a molecular double quantum dot: Role of the anisotropic exchange," *The Journal of Physical Chemistry C*, vol. 123, no. 18, pp. 11 917–11 925, 2019.

[155] V. N. Golovach and D. Loss, "Kondo effect and singlet-triplet splitting in coupled quantum dots in a magnetic field," *Europhysics Letters*, vol. 62, no. 1, p. 83, Apr. 2003.

[156] H. B. Akkerman, B. de Boer, M. Taniguchi, M. Tsutsui, K. Yokota, *et al.*, "Lithographic mechanical break junctions for single-molecule measurements in vacuum: Possibilities and limitations,"

[157] C. A. Martin, R. H. M. Smit, R. v. Egmond, H. S. J. van der Zant, and J. M. van Ruitenbeek, “A versatile low-temperature setup for the electrical characterization of single-molecule junctions,” *Review of Scientific Instruments*, vol. 82, no. 5, p. 053 907, May 2011.

[158] L. Li, C. Nuckolls, and L. Venkataraman, “Designing long and highly conducting molecular wires with multiple nontrivial topological states,” *The Journal of Physical Chemistry Letters*, vol. 14, no. 22, pp. 5141–5147, 2023, PMID: 37252687.

[159] R. Yasui, D. Shimizu, and K. Matsuda, “Large enhancement of the single-molecular conductance of a molecular wire through a radical substituent,” *Chemistry – A European Journal*, vol. 28, no. 27, e202104242, 2022.

[160] L. Li, S. Louie, A. M. Evans, E. Meirzadeh, C. Nuckolls, and L. Venkataraman, “Topological radical pairs produce ultrahigh conductance in long molecular wires,” *Journal of the American Chemical Society*, vol. 145, no. 4, pp. 2492–2498, 2023, PMID: 36689781.

[161] M. Mayländer, P. Thielert, T. Quintes, A. Vargas Jentzsch, and S. Richert, “Room temperature electron spin coherence in photogenerated molecular spin qubit candidates,” *Journal of the American Chemical Society*, vol. 145, no. 25, pp. 14 064–14 069, 2023, PMID: 37337625.

[162] Y.-Y. Huang, “The long-coherent-time and potentially scalable qubits composed of electric dipolar molecules based on graphene,” *arXiv preprint arXiv:2103.07263*, 2021.

[163] A. Al-Qatatsheh, S. Juodkazis, and N. Hameed, “Bridging performance gaps: Exploring new classes of materials for future spintronics technological challenges,” *Advanced Quantum Technologies*, vol. 6, no. 12, p. 2 300 204, 2023.

[164] Y. Joo *et al.*, “Thermoelectric performance of an open-shell donor–acceptor conjugated polymer doped with a radical-containing small molecule,” *Macromolecules*, vol. 51, no. 10, pp. 3886–3894, 2018.

[165] J. Hurtado-Gallego *et al.*, “Thermoelectric enhancement in single organic radical molecules,” *Nano Letters*, vol. 22, no. 3, pp. 948–953, 2022, PMID: 35073099.

[166] Q. Zhong, X. Li, H. Zhang, and L. Chi, “Noncontact atomic force microscopy: Bond imaging and beyond,” *Surface Science Reports*, vol. 75, no. 4, p. 100 509, 2020.

CURRICULUM VITÆ

Thomas Yves BAUM

14-09-1995 Born in Schiltigheim, France.

EDUCATION

2009–2013 High School
Lycée Fustel de Coulanges
Strasbourg, France.

2013–2017 Bachelor of science in Physics
Université de Strasbourg
Strasbourg, France.
Thesis: Dispersive forces arising from electromagnetic confinement
Promotor: Dr. M. Rastei

2017–2019 Master of science in Physics
Université de Strasbourg
Strasbourg, France.
Thesis: Single colloidal quantum dot luminescence in an atomic force microscope
Promotor: Dr. M. Vomir & Dr. M. Rastei

2019–2023 PhD. in Applied Physics
Delft University of Technology
Delft, The Netherlands.
Thesis: Electronic transport signatures of two electrons interactions in all-organic molecular junctions
Promotor: Prof. Dr. Ir. H. S. J. van der Zant

LIST OF PUBLICATIONS

3. T. Cardona-Lamarca*, **T. Y. Baum***, R. Zaffino, D. Herrera, R. Pfattner, S. Gómez-Coca, E. Ruiz, A. González-Campo, H. S. J. van der Zant, N. Aliaga-Alcaldea, *Polycyclic Aromatic Hydrocarbon-based curcuminoids in graphene nano-junctions*, (Submitted to Chemical Science).

2. A. Vegliante, S. Fernandez, R. Ortiz, M. Vilas-Varela, **T. Y. Baum**, N. Friedrich, F. Romero-Lara, A. Aguirre, K. Vaxevani, D. Wang, C. Garcia, H. S. J. van der Zant, T. Frederiksen, D. Peña, J. I. Pascual, *Tuning the Spin Interaction in Non-planar Organic Diradicals Through Mechanical Manipulation* arXiv:2402.08641 (2024) (Submitted to ACS Nano).

1. **T. Y. Baum**, S. Fernández, D. Peña, H. S. J. van der Zant, *Magnetic Fingerprints in an All-Organic Radical Molecular Break Junction*, Nano Letters **22** 20, 8086-8092 (2022).

---

* These authors contributed equally

ACKNOWLEDGEMENTS

How fortunate is it to spend a life dedicated to learning? Days and nights filled with the pursuit of meaningful information from a vast, chaotic collection of knowledge. Even in peaceful moments, it's challenging to remember all the people who contributed to this journey.

I must first acknowledge our collaborators who synthesized the molecules studied throughout this thesis: Diego Peña, Saleta Fernández, and Manuel Vilas-Varela. I also thank those who accepted the duty of serving on the jury for the defense of this thesis: Arzhang Ardavan, Jaime Ferrer, Nacho Pascual, Sander Otte, Mario Ruben, and Sonja Conesa-Boj. Additionally, I would like to thank Jos Thijssen for being my second promotor during this thesis and Yuli Nazarov for being my mentor.

Before working with these collaborators during the last years, I was fortunate to be surrounded by supportive colleagues in Strasbourg. I would like to thank everyone who introduced me to the fascinating world of physics. The first to guide me into the academic world was Mircea Rastei. He fascinated me with his probing questions about deep physical concepts, combined with one of the friendliest personalities I've ever met. I will never thank you enough for the encouragement and everything you taught me. Soon after meeting Mircea, I met Oussama, a PhD candidate working on the optical chiral forces acting on nanoparticles. Another friendly guy that introduced me to his circle where I could hear about the most fascinating stories of (but not limited to) science on the weekly Monday journal club. The exceptional people in this place shaped my curiosity for condensed matter physics. They helped me to understand more than the surface of the long chapters studied at university: Thibaut, Étienne, Ziad, David, Arthur and many others. Soon after, I started my first student project with Mircea and began visiting IPCMS weekly for the next four years. The burning discussion about physics, computers, and technology with Alberto are fond memories that often come to mind when I wrestle with Debian permissions. My thoughts also go to Mircea, Bertrand, Laurent, Jean Louis and all the member of DMO. I do not forget my former colleagues Manouel, Nicolas, Loïc and many others among the wonderful people from DMO and IPCMS.

During my years at university, I was fortunate to find the finest associates to tackle the hefty amount of math required, aided by concentrated hits of caffeine during the crazy nights just before exams. The firsts I met during my undergraduate studies were Jean and Theo, followed by Leo and Pier Andrea. After experiencing challenges with the intense study of short hydroxylated carbon chains (a common issue for many students), I had to collaborate with new peers during my master's program: Thomas and Dylan. If there's one thing I learned from them, it's to stay close to people who challenge you, not only for the inspiration from the quality of their work but also for the relevance of their questions. With them, I learned how to develop a solid critical spirit, and I couldn't have asked for better companions to share this journey.

I met Herre after sending him a simple email. Having accepted another PhD in Paris a few days before, I went to the mont Blanc and had the good idea to lose my phone on this journey. Upon returning to civilization, I found Herre's response in my mailbox, inviting me to visit his lab, and I went directly to the Netherlands. I discovered there the crazy idea of catching single molecules into electronic circuits and became instantly found of the operation. thank you for this journey over the past years. Your direction taught me more than I could have expected, and your contagious passion for science kept me deeply engaged in the pursuit of understanding.

When I arrived in Delft I was welcomed and guided by a young and enthusiastic team. The first lab member who held out his hand to me was a master's student at that time, Tristan. Thank you for being such a great colleague over these years. I wish you the best for your thesis and the next chapters of your career. I also thank the lab members who taught me the first steps, from the clean room to the fridge: Maria, Chunwei, Lucas, Pascal and Martin. Over the course of these four years, several exceptional people left, arrived or passed by the lab. The postdocs Talieh and Josep, whom I wish the best, but also some rest, in their American adventures. Samuel which is the perfect colleague to share an office with: not only will he be around and can open your door with a smile from Monday to Sunday, he also gives some excellent advice to write thesis. I hope your research will lead you where you deserve to be. There are also the fantastic PhD candidates with whom we shared so many moments: devoted work, hopeless tentatives, delusional results, but most of all, we felt the joy of learning together. To all of you, I can only believe that your work, dedication and kindness will get you to the bright future you deserve: Jacqueline, Jasper, that already started their new life, and Damian, which is about to begin his. Sebastiaan, Sergii, Maurits, to whom I also wish the best for your redaction and to enjoy some rest after this four years marathon. There's also the new PhD students, Linde, Yongqing and Cosimo, for which I do not worry as they're in the good hands of Captain S.J. May your PhD teach you the things you didn't know you wanted to know. The masters students that went by the lab have been a colorful and unexpected patchwork of diverse people, and turned out to be as surprising as fun to work with. Alessandro, always ready to move sky and earth (including barbecues over long distances); Jorien, always with a smile, even with the computer crashing; Daan, always asking if he can get you something at Spar; Arnaud, always filling the fridge, rain or snow; Loic, always telling another **cking great story; Danyil, always ready to help, even with weird robot problems; and Giannis, always politely asking before draining an unused battery to the ground. Your contagious motivation created a wonderful place to work, and I wish you all the best. There are two other PhD's whose futures I do not worry about: Alvaro, with his Latin kindness and boundless energy directed towards organizing social events for the department and dancing on the Friday night; and Riccardo, the mental gymnast and MacGyver-to-be of the lab. Thank you for the fantastic time we had together and thank you for being the paranymph of this defense. I wish you success, and to always keep this joy of learning. I also thank Rebecca, who helped me and many other students with the obscure art of nanofabrication. Your smile was always a pleasure to encounter, both in and out of the cleanroom. Finally, I extend my thanks to all those whom I barely met but whose presence was felt: Riccardo(s), Michael, Joeri, Max, Rocco, and many others.

I also extend thanks to all the people who helped us run these experiments over the

years. I must thank the entire cleanroom team at the Kavli Nano Lab for allowing us to work in the best conditions and always being there to help solve problems: Marc, Eugene, Charles, Anja, Bas, Lodi, Roald, Marinus, Paulien, Hozanna, and Arnold. Also to the QN Special thanks to Tino and Ronald for their cheerful assistance with unexpected failures in all situations. I also highlight the help from the wonderful people of DEMO, who assisted us efficiently and were a pleasure to converse with: Jack, Wouter, Yannick, and many others.

I would like to highlight my thanks to Nacho Pascual and all his group. Thank you for the invitation to discover the wonderful world of STM; my stay in San Sebastián was one of the most beautiful moments of my thesis, and meeting you reminded me of why what we do is so cool! I wish all the best to these wonderful people: Stefano, Léonard, Dongfei, Danilo, Katerina and Niklas; thank you for welcoming me with such kindness and for all these discussions that taught me so much. Among all these wonderful people, I especially want to highlight my thanks to Alessio and Fran. The hours spent together in the lab and out for kañas are warm memory I've kept in my heart over the Dutch winter. May your future reflect the brilliant and kind people you are.

I met many other PhD students, postdocs and scientists during conferences and summer school. I realized how much you can connect about subjects beyond science: cooking, cinema, philosophy, music, painting, and knowledge in all possible forms. Rafael, I wish you the best with the redaction of your thesis and your bright future in science. Also, I wish the best for Christian; I expect you found what you've been looking for and hope to see you around a random corner someday. I also take the occasion to thank Alexandre that always have a nice word when we cross in the corridor, I hope you will continue to enjoy Delft. Patrick, may your smile never leaves you et j'éspère te croiser bientôt sur Panam mon pote. Another unexpected apparition occurred when Rossella spawned in front of a probe station. I will keep this unexpectedly fruitful fishing manoeuvre inscribed in my mind. Thank you for surviving the terrible graphene junction and bringing that amount of joy to your work.

There are also those you wouldn't believe you would miss so much. My brother, Antoine, that I wish I could be closer; my cousin, Julien who was always watching for me; Marina whom I wish the best life with her soon-to-be husband, Xavier, Laura and all her energy, Mahe and his taste for adventure, Romain, and his golden tongue, Leo, and his characteristic phlegm so unusual for his age, Chloé, that I wish to find her promised way, Stella and her charismatic and reinsuring aura that seems impossible for such a young Lady, Chiara and her resilient spirit that remind me that I sometimes become too soft about my beliefs. My uncle, Francois, and his artistic soul that I always connect with in instants. Pinou, my god-father, is the best proof that a person can be as sweet inside as he looks solid outside. To Mimmo, who saved my life a couple of times over the years, including those of my PhD and some recent events: your kindness, righteousness and openness are among the most beautiful I have seen; thank you for all the discussions, all the words that you had to me. My aunt, Consi, and her inextinguishable combativeness have been a model over the last few years. Our discussions that always started randomly, never bound by time, have been a lighthouse when I was lost in the storm of everyday life. My grandmother Danielle, whom I will keep as a model of elegance and savoir-vivre, and Chiara, my Nona; living with you taught me things I'm still discovering nowadays.

And there are also the ones that are so close that they feel like family each time I cross their path: Pascale, Gilles and Solene.

I also want to thank those that I wish could be here to share these moments. My Aunt Christina proved me that joy is the best way to respond to the maddest events in life. Sometimes, when I vacuum clean my apartment, I see you dancing on the table with a unique selection of the finest hits of the last 40 years (now 50 - aïe!) playing on the speakers. I hope this memory will never leave my heart. The ones who taught me that the most enjoyable lessons are those that make remarkable stories: my great-grandfather André and my grandfather Yves. You taught me to always strive to understand without judging, and your wonderful curiosity is a trait I proudly inherited.

It's when you're far from what's really important that you miss it, and it's one of the lessons I learned during these four years. I am lucky to have such a fantastic family. I couldn't thank them enough for believing in me and continuously offering encouragement. I want to thank my dad, that always helped me to push myself to the maximum. You always acted that way for me, even when I didn't realize it, and I want to thank you for that. Of course, I must thank the two women of my life: my sister and my mother. They are handling me in the shadow; they have been my best friend, confident, and reason to push myself every morning for a long time now. The present booklet would need to be more spacious to express my gratitude for having you.

Finally, there are the ones building your character that you want to keep as close as possible, as long as it is allowed. Marion, even though we haven't seen each other as often as I wished during these years, each time was like we've never left each other. I hope we will be able to increase our meeting frequency and keep our instantaneous connection. Antoine, we have known each other for more than two decades, and our relationship continued growing in curiosity, respect and constancy. May our friendship continue on this path. PA, in these years, it seems we have developed our own language. We went through several crazy subjects and situations together, and I have always been able to rely on you. I hope we will keep this forever. Marjorie, or Paton, you have been a refreshing ointment to some profound wounds. It's funny how the furthest people can have such a significant influence. Thank you for being who you are. And finally, there is one I used extensively to feed my mind, which never went into a conversation with the slightest preconceived idea: Anthony. Through philosophy, music, History, literature, science (and endless nights playing video games), we exchanged invaluable amount of ideas and feelings. Our crazy projects proved how loyal we have always remained to each others. Having such a friend who shares a part of your blood is a gift I am grateful for every time we talk. I hope you find what you're looking for and the strength to get it.

It's interesting how individuals are mainly defined by their environment. Many body effects are difficult to understand with certainty, but I'm sure that it is thanks to you that I am standing where I am today.